DESIGN OF MESOPOROUS SMALL-PORE ZEOLITES FOR DIRECT CONVERSION OF METHANE TO METHANOL

A THESIS SUBMITTED TO
THE GRADUATE SCHOOL OF NATURAL AND APPLIED SCIENCES
OF
MIDDLE EAST TECHNICAL UNIVERSITY

BY

ÖZGÜN MEMİOĞLU

IN PARTIAL FULFILLMENT OF THE REQUIREMENTS
FOR
THE DEGREE OF MASTER OF SCIENCE
IN
CHEMICAL ENGINEERING

JULY 2020

Approval of the thesis:

DESIGN OF MESOPOROUS SMALL-PORE ZEOLITES FOR DIRECT CONVERSION OF METHANE TO METHANOL

submitted by **ÖZGÜN MEMİOĞLU** in partial fulfillment of the requirements for the degree of **Master of Science** i**n Chemical Engineering, Middle East Technical University** by,

Prof. Dr. Halil Kalıpçılar
Dean, Graduate School of **Natural and Applied Sciences** _____

Prof. Dr. Pınar Çalık
Head of the Department, **Chemical Engineering** _____

Assist. Prof. Dr. Bahar İpek Torun
Supervisor, **Chemical Engineering, METU** _____

Examining Committee Members:

Prof. Dr. Deniz Üner
Chemical Engineering, METU _____

Assist. Prof. Dr. Bahar İpek Torun
Chemical Engineering, METU _____

Prof. Dr. Naime Aslı Sezgi
Chemical Engineering, METU _____

Assoc. Prof. Dr. Dilek Varışlı
Chemical Engineering, Gazi University _____

Assist. Prof. Dr. Gökhan Çelik
Chemical Engineering, METU _____

Date: 29.07.2020

I hereby declare that all information in this document has been obtained and presented in accordance with academic rules and ethical conduct. I also declare that, as required by these rules and conduct, I have fully cited and referenced all material and results that are not original to this work.

Name, Last name : Özgün Memioğlu

Signature :

ABSTRACT

DESIGN OF MESOPOROUS SMALL-PORE ZEOLITES FOR DIRECT CONVERSION OF METHANE TO METHANOL

Memioğlu, Özgün
Master of Science, Chemical Engineering
Supervisor : Assist. Prof Dr. Bahar İpek Torun

July 2020, 118 pages

Methane is the main component of natural gas, a useful feedstock and an abundant material. Therefore, valorization of the methane can be considered as an important field of research. Selective conversion of methane to valuable materials such as methanol is a highly desired, yet challenging process due to the high activation energy (439 kJ mol^{-1}) of C–H bonds in methane and weak acidity of methane. Zeolites that are exchanged with copper and iron could activate methane at low temperatures and allow selective formation of partial oxidation products using a non-catalytic 3-step process. To provide a commercial methanol production; however, selective methanol production in a continuous process should be achieved at meaningful methanol formation rates.

Continuous methanol production systems using Cu-zeolites remain largely unexplored, and practical applications necessitate fundamental understanding for catalyst and process improvement. In this study, to perform the methane to methanol reaction at high yield and methanol selectivity and at mild temperatures, we have developed different type of zeolites such as Mordenite, SSZ-13, SSZ-39 and Omega with different concentration of active Cu-centers. We also introduced mesoporosity

to increase methanol selectivity. Catalytic experiments were conducted with altered feed gas compositions and optimization of the partial pressure of the reactants was performed.

At 573 K, microporous SSZ-39 and Mordenite showed the best methanol production rates (90.6 μmol g^{-1} h^{-1} and 54.7 μmol g^{-1} h^{-1}**)** and plausible selectivities of 44% and 54% respectively. Mesopore addition resulted in increased methanol selectivity only for SSZ-39 with shortened crystal sizes.

Increasing N_2O partial pressure (to 15 kPa) have caused increased methanol production rates and selectivity values up to 52% and 130 μmol g^{-1} h^{-1} for SSZ-39. In the same way, incerasing methane partial pressure (to 40.4 kPa) resulted in incresed methanol production rates up to 90.6 μmol g^{-1} h^{-1} for SSZ-39 and 54.7 μmol g^{-1} h^{-1} for Mordenite. In addition, increasing partial pressure of water has showed increased methanol selectivity values with similar methanol production rates on SSZ-39 (311 μmol g^{-1} h^{-1}) and Mordenite (116 μmol g^{-1} h^{-1}).

Keywords: Methane to Methanol, Catalysis, Cu-SSZ-39, Mesoporous Zeolites,

ÖZ

METANDAN DİREKT METANOL ELDESİNDE MEZO-GÖZENEK İLAVELİ KÜÇÜK-GÖZENEKLİ ZEOLİT TASARIMI

Memioğlu, Özgün
Yüksek Lisans, Kimya Mühendisliği
Tez Yöneticisi: Assist. Prof. Dr. Bahar İpek

Temmuz 2020, 118 sayfa

Metan, doğal gazın ana bileşeni, faydalı bir hammadde ve bol miktarda çıkarılabilen bir malzemedir. Bu nedenle, metanın değerlenmesi önemli bir araştırma alanı olarak kabul edilebilir. Metanın metanol gibi değerli malzemelere seçici dönüşümü, metandaki C–H bağlarının yüksek aktivasyon enerjisi (439 kJ mol^{-1}) ve metanın zayıf asitliği nedeniyle oldukça istenen ancak zorlayıcı bir süreçtir. Bakır ve demir içeren zeolitler, metanı düşük sıcaklıklarda aktive edebilir ve katalitik olmayan 3-aşamalı bir işlem kullanarak kısmi oksidasyon ürünlerinin seçici oluşumuna izin verirler. Seçici metanol üretimini miktarda ticari olarak sağlamak için, anlamlı metanol oluşum hızları gösteren sürekli bir proses gerçekleştirilmelidir.

Cu-zeolit kullanan sürekli metanol üretim sistemleri büyük ölçüde araştırılmamıştır ve pratik uygulamalar katalizör ve proses iyileştirme için temel bilgi birikimi gerektirir. Bu çalışmada, metan-metanol reaksiyonunu yüksek verim, ve seçicilikte orta sıcaklıklarda gerçekleştirmek için, farklı aktif Cu-merkezleri konsantrasyonuna sahip Mordenite, SSZ-13, SSZ-39 ve Omega gibi farklı tipte zeolitler geliştirilmiştir. Ayrıca metanol seçiciliğini artırmak amacıyla mezoporozite eklenmiştir. Değişen

besleme gazı bileşimleri ile katalitik deneyler yapılmış ve reaktanların kısmi basıncında optimizasyon yapılmıştır.

573 K sıcaklıkta mikro gözenekli SSZ-39 ve Mordenite, sırasıyla en iyi metanol üretim hızlarını (90.6 μmol g^{-1} h^{-1}ve 54.7 μmol g^{-1} h^{-1}) ve uygun seçicilikleri (% 44 ve % 54) göstermiştir. Mezogözenek ilavesi sadece SSZ-39 örneğinde kısalan kristal boyutları sayesinde artan metanol seçiciliğine sebep olmuştur.

Artan N_2O kısmi basıncı, mikro gözenekli SSZ-39 için 130 umol g^{-1} h^{-1}'e kadar artan miktarda metanol üretim değerleri ve % 52 oranında sseçicilik sağlamıştır. Aynı şekilde, 40.5 kPa metan kısmi basıncı SSZ-39 için 90.6 μmol g^{-1} h^{-1} ve Mordenite için 54.7 μmol g^{-1} h^{-1}'e kadar artan metanol üretim hızlarıyla sonuçlanmıştır. Ek olarak, artan kısmi su basıncı, yüksek metnol seçiciliği ve SSZ-39 (311 μmol g^{-1} h^{-1}) ve Mordenit (116 μmol g^{-1} h^{-l}) üzerinde dikkate değer metanol üretim oranları göstermiştir.

Anahtar Kelimeler: Metandan Metanolün sentezi, Kataliz, Cu-SSZ-39, Mezogözenekli zeolit

To my lovely family

ACKNOWLEDGMENTS

First and foremost I would like to express my sincerest gratitude to my supervisor, Assist. Prof. Dr. Bahar İpek Torun, who always supported me throughout my thesis with her patience and knowledge and giving me the opportunity to be part of her research group. I am grateful to her supervision, advice, and guidance from the very early stage of this research.

Furthermore, I would like to thank to the rest of my thesis committee; Prof. Dr. Deniz Üner, Prof. Dr. Naime Aslı Sezgi, Assoc. Prof. Dr. Dilek Varışlı and Assist. Prof. Dr. Gökhan Çelik for their valuable comments.

I would also like to thank the Zeolite Synthesis and Application Research Laboratory members for their endless support and friendship through the research, İsmihan Altıparmak and Büşra Karakaya for their supports and helps during my research. Also I am thankful for our undergraduate members Melis Özdemir and Doğa Tektaş for their support. My special thanks to my dear best friends Elçin Çağlan, Aytaç Tan and Oğuzhan Satı for all their advice, faithful support and encouragement during my all study.

I especially thank to my beloved, Enes Aydın, for his endless support, affection and great patience in this study. His advices made me more confident to achieve my goals. It has always been a relief to know you all are beside me when times are rough. Last but not least, I would like to express my appreciation to my father, Haluk Memioğlu, my mother Bahriye Memioğlu, my sister Öyküm Karakoyunlu, my aunt Ufuk Memioğlu, my dear grandmother Mine Memioğlu and also my babies Ata and Ilgın for their unconditional love, care and support. I would not have made it this far without them.

This project is funded through the Scientific and Research Council of Turkey (TUBITAK) Career Development Program project with Grant No: 118M656. BAP-YLT-304-2018-2712 is also acknowledged for financial support.

TABLE OF CONTENTS

LIST OF TABLES

TABLES

LIST OF FIGURES

FIGURES

LIST OF ABBREVIATIONS

ABBREVIATIONS

MTM	Methane to Methanol
MeOH	Methanol
XRD	X-Ray Diffraction
SEM	Scanning Electron Microscopy
EDX	Energy Dispersive X-Ray Spectroscopy
ICP-OES	Inductively Coupled Plasma-Optical Emission Spectroscopy
BJH	Barret-Joyner-Halenda Adsorption Model
SDA	Structure Directing Agent
CTABr	Cetyltrimethylammonium bromide
DFT	Density Functional Theory

LIST OF SYMBOLS

SYMBOLS

T	temperature, K
P	pressure, kPa
RF	response factor, ppm area^{-1}
λ	wavelength, Å
S	selectivity, %
X	conversion, %
r	rate, μmol g^{-1} h^{-1}
TOF	turnover frequency, h^{-1}

CHAPTER 1

INTRODUCTION

Zeolites are inorganic crystalline aluminosilicates, whose structure comprises of a three dimensional arrangement of TO_4 tetrahedra, where T usually denotes tetrahedrally coordinated Si^{4+} and Al^{3+} atoms. Tetrahedral atoms gather together through the sharing of oxygen atoms to form subunits, which repeat to create an infinite lattice [1], see Figure 1.1. Different ways of tetrahedra connection cause a diversity of zeolite framework types based on various compositions. Chemically, zeolites are represented by the general formula of $M^{n+}_{y/n}[(SiO_{4/2})_x(AlO_{4/2})^-_y].zH_2O$ where n symbolize valence state of the metal cation M, x and y demonstrate the number of Si and Al atoms in the unit cell, respectively, and z represents the quantity of water molecules in a single unit cell [2]. As of June 2020, the variety of existing crystalline molecular sieve topologies is recorded in 241 frameworks [3] and many more zeolites and zeo-types having a variety of Si/Al ratios or additional tetrahedral atoms such as P have discovered. They are used in a wide range of pH values for industrial applications such as detergents and water treatment, removal of radionuclides from nuclear waste effluents, and in adsorption/separation processes and in catalysis.

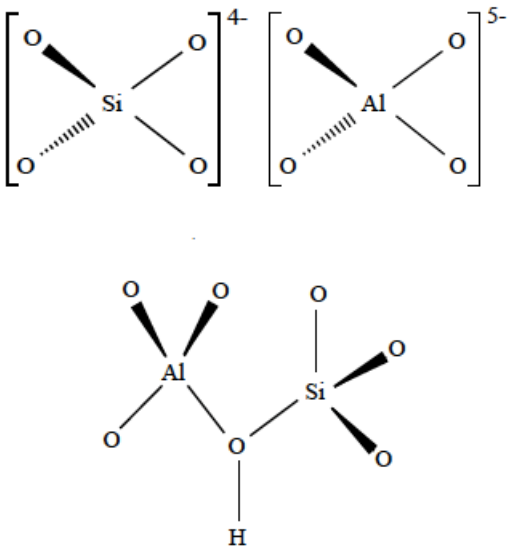

Figure 1.1. Tetrahedral arrangement of SiO_4 and AlO_4 molecules

The Si/Al ratio in a zeolite is crucial in determining the thermal stability, extraframework cation capacity and therefore the adsorption and catalytic properties. The Si/Al ratio can vary from 1 to infinity in zeolites. When the Si/Al ratio of the zeolite increases, aluminum content decreases causing an increase in the acid strength of the zeolite and increase in the thermal stability, which is proportional to the silicon content. Cation exchange capacity; on the other hand, decreases because of the declining number of the negative charges; i.e., Al content in the framework [4].

Zeolites are formed in nature in association with a chemical reaction between volcanic glass and saline water and can also be synthesized in the laboratory. First natural zeolite stilbite (STI) was discovered in 1756 by the Swedish mineralogist Cronsted [2] but the structure properties of natural zeolites and their usefulness in adsorption and separation processes and ion-exchange were recognized not until 19th century. After 1862, when the first laboratory synthesis of zeolite by St. Claire Deville was performed [5], series of different synthetic zeolites were hydrothermally synthesized through mimicking of the geothermal formation of natural zeolites.

1.1 Synthesis of Zeolites

Zeolites are typically synthesized in a gel under hydrothermal conditions with inorganic cations (Na^+, K^+, Li^+) or organic amines/ammonium cations (tetramethylammonium; TMA, tetraethylammonium; TEA, tetrapropylammonium; TPA) as the structure directing agents (SDAs), which directs the crystallization towards a specific zeolite structure. The final solution usually contains tetrahedral atom (Al, Si, etc.) sources, the SDA, and the mineralizer (OH^-). The mixture is then heated in a Teflon-lined stainless-steel autoclave under autogenous pressure at temperature 373-523 K for a period of time. Numerous synthetic factors influence the formation of zeolites, such as the source materials, aging, solvent, SDA, gel composition, pH value, and crystallization temperature and time [6]. In this study, different structure directing agents will be used in order to obtain desirable zeolites. For the synthesis of omega, tetramethylammonium hydroxide, for SSZ-13 trimethyladamantylammonium hydroxide, finally for the synthesis of SSZ-39 tetramethyl piperidinium hydroxide was utilized.

1.2 Structure of Zeolites

All zeolite frameworks can be built by linking primary building units (PBU), TO_4, a tetrahedron, in a periodic pattern. More complex building units can be formed by linking several PBUs, which are called secondary building units (SBU) such as 4-membered, 6-membered rings (4MR, 6MR) of tetrahedral. Composite building units (CBUs) such as double-six membered rings (d6MRs) are formed by assembling different types of SBUs (Figure 1.2). Different zeolite structures are formed depending on how these building units are linked together. These units play a significant structure directing role in the crystallization. [7].

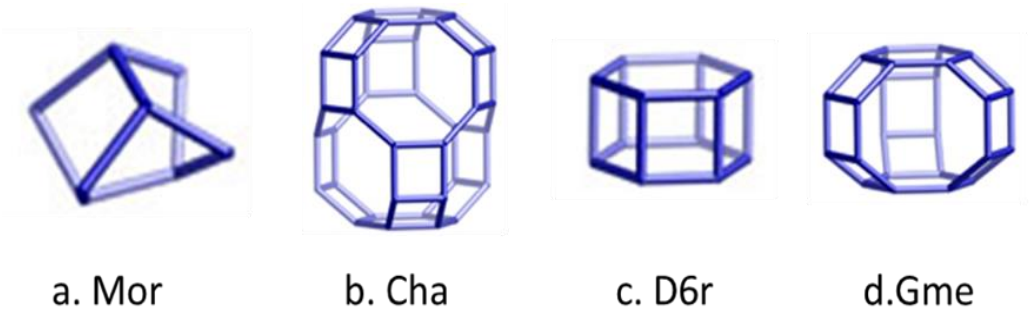

Figure 1.2. Composite building units for a. Mordenite b. SSZ-13 c. SSZ-39 d. Omega [3]

Small pore zeolites with 6MR and 8MR have pore sizes of 0.25–0.45 nm, medium pore zeolites with 10MR contain 0.45–0.60 nm pore sizes and large pore zeolites with 12MR show 0.6–0.8 nm pore sizes, respectively. The micropores of zeolites can consist of channels or cages, which may be interconnected to form a multidimensional porous system. Variability of pore size and shape of the zeolite provides shape-selective catalysis, and hence controls the product distribution of a reaction [2].

Pore systems and structures of zeolites used in this thesis are summarized in Table 1.1.

Table 1.1. Pore systems and Structures of Mordenite, SSZ-13, SSZ-39 and Omega

Zeolite	IZA Framework Code	Ring Sizes	Pore Opening (Å)	Framework Density (T 1000 $Å^{-1}$)
Mordenite	MOR	12,8,5,4	7.0	17
SSZ-13	CHA	8,6,4	3.8	15.1
SSZ-39	AEI	8,6,4	3.8	15.1
Omega	MAZ	12,8,6,5,4	3.1, 7.4	17.7

1.3 Applications of Zeolites

Zeolites are used in catalysis, ion-exchange, adsorption, gas separation and many other fields in technology. Recently, there is an increased research activity in zeolites towards the development of zeolites such as utilizing aluminophosphates and other nonconventional compositions, creation of mesopores, finding new frameworks, etc. Zeolites are very commonly used as catalysts in petrochemical industry with the help of two properties; acid sites as active sites in the crystals and size and geometry of the zeolite pores, which determines the selectivity. These properties provide high activity and selectivity in a diverse range of catalytic reactions [8]. Zeolite Y and SSZ-13 were commercialized in fluid catalytic cracking and octane enhancement. In addition, zeolites are non-toxic, have very high surface area, which enhance the ability of forming higher amount of active sites for reactions, having uniform pores and different size of channels and cavities ranging from 5–15 Å, which allows being a shape selective catalyst. Utilization of the zeolite as a catalyst have the highest market value for synthetic zeolites (13%). The use of zeolite as an ion-exchanger has the largest volume in detergents for water softening (72 %), as an adsorbent in purification and separation processes (15%) [5].

1.4 Zeolite Structures in This Study

1.4.1 MOR Structure

Mordenite pertains to MOR type zeolite. MOR type has an orthorhombic structure featuring *Cmcm* space group with unit cell dimensions of a= 18.2560 Å, b= 20.5340 Å and c= 7.5420 Å and a framework density of 17.0 T atoms per 1000 $Å^3$[3]. Its framework built from chains of four membered rings and five membered rings, where 5MR is dominant. It also contains twelve-membered main channels (7.0×6.5 Å) and small 8MR channels (5.7×2.6 Å) interconnected to side pockets that are accessible through eight-membered rings (3.4×4.8 Å) seen in Figure 1.3. Its channel

system considered as a one dimensional structure [9]. In addition, it has a 476.2 m^2 g^{-1} surface area and 0.30 cm^3 g^{-1} pore volume with a micropore volume around 0.18 cm^3 g^{-1} [10]. Natural mordenite is highly siliceous and exists with a nearly constant Si/Al ratio of 5, while synthetic mordenite has been made with Si/Al ratios from about 4 to 12. Mesoporosity can be introduced for mordenite which promote to its application in petrochemical conversion processes. It has a wide range of application in not only hydrocracking, isomerization and alkylation but also in adsorption of some pollutants like heavy metals [11,12].

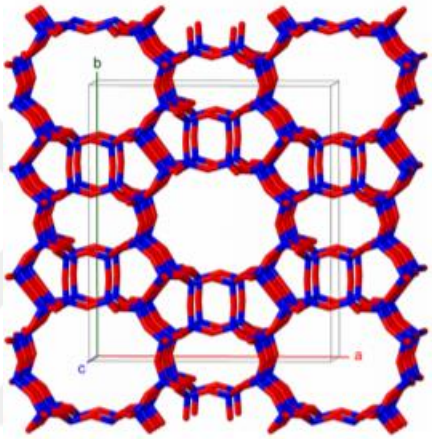

Figure 1.3. Framework structure of Mordenite (MOR) [13]

1.4.2 CHA Structure

SSZ-13 belongs to CHA type zeolite family, which is characterized by a triangular structure (Rhombohedral) having a R-3m space group and unit cell dimensions of a=13.6750 Å, b=13.6750 Å and c=14.7670 Å. It has a framework density of 15.1 T atoms per 1000 Å3[3]. It is identified by layers of double six membered rings (6-MR) that are linked by units of four membered rings. CHA has a three dimensional pore system with ellipsoidal-shaped large cages, whose openings are eight membered rings with size of (3.8x3.8 Å) as shown in Figure 1.4 [13]. SSZ-13 has a BET surface area of about 710 m^2 g^{-1} and micropore volume of 0.25–0.30 cm^3 g^{-1}. SSZ-13 has attracted great attention since its important physiochemical properties

and outstanding potential as a catalyst for various applications due to its small pore and relatively large cavities in its structure. Specially, it has potential applications as catalysts for NH_3-SCR reaction and catalytic methane to methanol reaction [14–18].

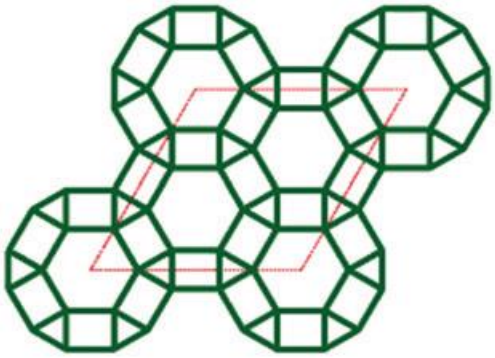

Figure 1.4. Framework structure of SSZ-13 (CHA) [13]

1.4.3 AEI Structure

SSZ-39 belongs to AEI type of zeolite characterized by an orthorhombic structure featuring *Cmcm* space group with a unit cell dimensions of a=13.6770 Å b= 12.6070 Å and c=18.4970 Å and a framework density of 15.1 T atoms per 1000 $Å^3$[3]. Framework composed of entirely double six-membered-ring (6-MR) units which are interconnected in three dimensional eight membered ring channel system, forming *aei* cage. It has an equal pores with diameter of (3.8 x 3.8 Å) seen in Figure 1.5 [14]. Both CHA and AEI types have the same channel size but the cavities of the AEI are pear shape cage. AEI type zeolites have 499 $m^2\ g^{-1}$ surface area and 0.27 $cm^3\ g^{-1}$ total pore volume which 0.20 $cm^3\ g^{-1}$ of it is micropore [15]. First synthesis of SSZ-39 was performed in 1997 by Zones et al. [16] and since then it has many catalytic applications such as selective catalytic reduction of NO_x, methanol to olefins, methane to methanol and ethane conversion reactions [17–21].

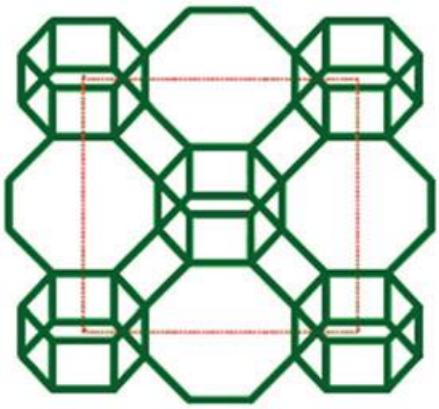

Figure 1.5. Framework structure of SSZ-39 (AEI) [13]

1.4.4 MAZ Structure

Omega has topological code of MAZ type zeolite. Framework of omega has a hexagonal symmetry belonging to a space group of *P63/mm* with unit cell dimensions of a=18.1020 Å, b=18.1020 Å and c= 7.6180 Å and framework density of 17.7 T 1000 $Å^{-1}$ [3]. Omega has columns of gmelinite-type cages sharing their 6-rings of tetrahedral to form 12 membered ring main channel-large pore (7.4 x7.4 Å). A secondary channel restrained by 8-membered rings- small pore having free diameter of (3.4 x3.4 Å) parallel to the 12MR pore system shown in Figure 1.6. MAZ type zeolites generally have BET surface area and total pore volume of 422 m^2 g^{-1} and 0.14 cm^3 g^{-1} respectively [22]. Omega is known for strong Brønsted acidity and large micropores which can be applied as a catalyst in methane to methanol conversion, hydroisomerization and adsorption [23–25].

.

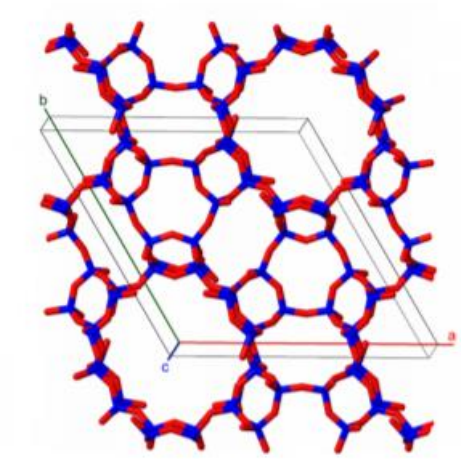

Figure 1.6. Framework structure of Omega (MAZ) [13]

1.5 Cu-Zeolites

Cu-exchanged zeolites, in which the proton or cation next to the aluminum atom is replaced with copper(II) ions to form an active site have attracted much attention for their catalytic activity in selective oxidation of methane and other hydrocarbons [31–33]. In 1986 Iwamoto et al. found that copper exchanged ZSM-5 was a great catalyst for deNO_x reactions. This discovery gave impetus to use Cu exchanged zeolites and they showed superior activity in selective catalytic reduction (SCR) of NO_x in the low temperatures. Cu-zeolites also have shown activity in selective oxidation of methane with various oxidants such as O_2 [18,33–40], N_2O [18,41], NO [42], He [43], H_2O_2 [44] and H_2O [45] in order to produce methanol. Notably, a wide range of zeolite topologies have been experimentally tested for this process. In these studies, methane generally activated utilizing a 3-step cyclic process. Lots of endeavours have been performed to improve methanol selectivity by altering the zeolite type, reaction temperature, oxidant type and other operation conditions such as partial pressure of reactants.

1.6 Conversion of Methane to Methanol

Methane functionalization was very difficult due to being significantly stabilized molecule. Obstacle of methane activation comes from very high strength of the C–H bond of methane, its electronic structure and high ionization potential. (12.61 eV) [26].

Different solutions have been presented to tackle the methane activation towards methanol under mild conditions. The mostly used strategies were, oxidation with a reactive oxygen species. Reactive metal−oxo species towards methane oxygenates can be formed in zeolites using oxidants such as oxygen, nitrous oxide, hydrogen peroxide, etc. Choice of oxidants have been important because Fe-zeolites cannot be activated using oxygen, but in the presence of other oxidants such as N_2O or H_2O_2, methane reactive sites can be formed. For N_2O, while α -oxygen atom transfer, N_2O lead for an unstable and reactive copper-oxo active sites. One favorable conversion of methane is into methanol. Methanol can be converted broad range of different products and it can be easily transported. Currently methanol processes pass over syngas that is obtained by methane steam reforming process, requiring large scale plants because of the energy-intensive operation at high pressures and temperatures. The main difficulty of direct methane oxidation into methanol is reaching high selectivity of methanol. Methane oxygenates are more reactive because of the fact that the dissociation energy of the products (~397 kJ mol^{-1} for methanol) are much smaller than that of methane (~439 kJ mol^{-1}), which cause over-oxidation products that are CO or CO_2. Because of this reason, the best yield for desirable intermediate products such as methanol is suggested to be %5 by Labinger [27].

1.6.1 3-Step Process

Remarkable methanol selectivity values higher than 95 % can be performed using 3-step process, which is based on stoichiometry. The methanol production amount depends on the number and the nature of the active sites. This cyclic three-stage

process involves: i) activation of the catalyst by O_2, N_2O or other oxidants treatment at high temperature > 723 K, ii) reaction with methane at lower temperatures (at ~473 K) iii) methanol extraction using different solvents or wet gas stream to obtain methanol. These three steps were encouraged at different temperatures and require several hours for one turnover.

In the first step, catalyst should be activated at high temperatures between 573 K and 873 K with oxidizing agents. This oxidation results in formation of active Cu_xO_y species. The identity and the location of these species are substantial for the methane activation at mild temperatures. Activation of the catalyst at high temperature cause not only the formation of the active sites but also complete dehydration of the catalyst. Smeets et al. reported that there is a need for an activation temperature of at least 553 K and not higher than 973 K [28] For the activation temperature of 473 K and 1023 K, methanol production amounts are found as 8.1 and 0.8 μmol CH_3OH g_{cat}^{-1}, respectively, which indicates that high activation temperature causes significant decrease in methanol yield [28].

The second step is the reaction step at lower temperatures between 423 K and 473 K, where the active Cu-oxo species reacts with the methane in order to form an intermediate as a product, which is strongly chemisorbed on the active sites (mostly encountered species being a methoxy). Reaction temperature might show changes according to the zeolite type. Reaction performed on Cu-mordenite and Cu-ZSM-5 with a reaction temperature of 423 K showed comparable results to reaction results obtained at 473 K on Cu-BEA and Cu-ferrierite [28].

The third step is desorption of the intermediate as methanol using extraction in polar solvents at room temperature or with a wet gas stream at high temperatures. Strong adsorption of the methoxy-type product requires a proton for removal of the product. Beznis et al. investigated the different solvents for the extraction step at room temperature. They proposed to use polar and protic solvents which could be ethanol or acetonitrile/water resulted higher amounts of methanol when compared to hexane and acetonitrile [29]. More recent procedures commonly uses the steam for extracting methanol for the convenience of the process [30]. According to recent

studies, adsorption energy between various copper-oxo active site species and methanol in most used zeolite structures, it is difficult to simultaneously desorb methanol formed in zeolite pores, but it is viable to desorb them via water.

This cyclic process could be repeated over and over in order to achieve high methanol production amounts. Activation temperature of 573–723 K was much higher than reaction temperature ~423–473 K and methanol extraction at room temperature or using steam. It should be considered that many factors such as the structure and composition of the zeolite, the structure of the copper active species and the reaction conditions selectively produce methanol by direct partial oxidation of methane. Depending on the structure of the zeolite, different active copper types can be created, on which methane is stabilized. Zeolites such as Cu-ZSM-5, Cu-MOR, Cu-Beta, Cu-Zeolite Y, Cu-Ferrerite, Cu-SSZ-13, Cu-SSZ-16, Cu-SSZ-39, Cu-ECR1, Cu-PST-11, Cu-UZM-4, Cu-omega have shown a high selectivity in methanol production using cyclic processes as shown in Table 1.2.

According to Table 1.2, initial studies using Cu-ZSM-5 showed a methanol production of about 8.2 μmol g_{cat}^{-1} with a selectivity towards methanol of over 98% (with negligible CO and CO_2 formation). When the reaction temperature is considered, Smeets et al. showed that methanol production achieved at 423 K on Cu-mordenite and Cu-ZSM5. However, Cu-BEA and Cu-FER could show a comparable production results at 473 K. Presence of different copper-oxo active species on different zeolite structures can explain this situation. In the same work, when the temperature increased to 473 K on Cu-mordenite, the methanol production was almost tripled (6 μmol g_{cat}^{-1} to 16 μmol g_{cat}^{-1} for Cu-mordenite). This indicates that different active sites that can be activated at low temperatures and high temperatures are present in Cu-mordenite [31].

Wulfers et al. discovered that several small pore zeolites and zeo-types such as SSZ-13, SSZ-39 and SAPO-34 could produce methanol with higher amounts than ZSM-5 and Mordenite, which have medium and large pores. They followed high

temperature water vapour extraction protocol resulted in more methanol production amount up to 39 μmol g_{cat}^{-1}, which was greater than previous reports at the time [32]. DFT calculations supported superior methanol formation activity on small porous zeolites (SSZ-13 and SSZ-39) with lower activation energies for C–H bond dissociation with $[Cu_2(\mu\text{-}O)]^{2+}$active site compared with medium and large pore zeolites, ZSM-5 and Mordenite, respectively [33].

Using 3-step process for direct methane to methanol conversion, long heating and cooling durations limit the applicability of the process. Because of that, isothermal multistep process was performed by Sheppard et al. using Cu-ZSM-5 as catalyst, NO as oxidant and desorption using steam [42]. NO oxidant activation, methane reaction, and methanol extraction were performed under the same temperature at 423 K, and a small methanol production amount of 0.63 μmol g_{cat}^{-1} was reported [42]. In addition, again an isothermal multiple step process was suggested by Tomkins et al. on Cu-mordenite using O_2 as an oxidant at 473 K and varying methane pressures [34]. Considering the effect of methane pressure, activation of catalyst at 1 bar of oxygen and 1.6 and 36 bar of methane resulted in 45.3 μmol g_{cat}^{-1}, 84.1 μmol g_{cat}^{-1} and 103.3 μmol g_{cat}^{-1} respectively [34]. Significant amount of methanol can be extracted when the catalyst was contacted with methane at high pressures. Increasing reaction time between methane and catalyst also showed increasing amounts of methanol production. Grundner et al. predict methane reaction time of at least 30 minutes to detect acceptable methanol formation on Cu-mordenite [34].

In the early studies, methanol was extracted offline, which explained as the reacted catalyst was mixed with a solvent outside from the reactor. Yet, offline extraction makes this process inefficient. Therefore, an online extraction method where steam is fed directly into the reactor has also been studied and increased the efficiency of methanol. The improved methanol formation activity is observed when the steps in the 3-step process is optimized in terms of temperature and duration. For example, Pappas et al. showed an increased methanol formation (to 170 μmol g_{cat}^{-1}) on Cu-Mordenite when the O_2 activation at 773 K and CH_4 reaction (at 473 K) times were prolonged to 6 h, achieving a methanol/Cu ratio of 0.45 [35]. Similarly, a methanol

formation amount of 125 μmol g_{cat}^{-1} and methanol/Cu ratio of 0.202 was achieved on Cu-SSZ-13 by elongating the O_2 activation time to 8 h [36].

Park et al. prepared 12 different zeolite structure types (i.e., MOR, EON, MAZ, MEI, BPH, FAU, LTL, MFI, HEU, FER, SZR, and CHA), and compared their methanol productivity based on the copper content, reaction temperature zeolite structure, and zeolite precursor type. According to the study, 86 μmol g_{cat}^{-1} methanol formation amount, has been achieved on Cu-Omega. When compared to other 8 MR zeolites under the same reaction conditions, the amount was a noteworthy methanol formation [37].

An interesting study proposed usage of H_2O as the oxidant to form the active sites instead of O_2. Sushkevich et al. have reported that Cu–MOR zeolites oxidized using H_2O at 673 K has showed an improved catalytic activity. 0.204 mol CH_3OH mol Cu^{-1}. They showed that methanol can be produced using H_2O as an oxidant [38], which was later debated due to the thermodynamic limitations of H_2O splitting to form the active sites at the aforementioned temperature.

Table 1.2. Experimental results for 3-step process

Material	IZA Code	Si/Al	Cu/Al	Oxidant	O_2 Activation		Reaction		Extraction	Methanol Produced (μmol CH_3OH g_{cat}^{-1})	Methanol/Cu (mol mol^{-1})	Ref
					Temperature (K)	Duration (h)	Temperature (K)	Duration (min)				
ZSM-5	MFI	12	0.31	O_2	723	24	473	15	H_2O: ACN solution	8.2	0.020	[31]
Mordenite	MOR	8.8	0.43	O_2	723	24	473	15	H_2O: ACN solution	11.34	0.016	[31]
Zeolite Y	FAU	2.7	0.29	O_2	723	24	473	15	H_2O: ACN solution	<1	0.005	[31]
Mordenite	MOR	8.8 8.8	0.50 0.50	O_2 O_2	723 723	24 24	423 473	15 15	H_2O: ACN solution H_2O: ACN solution	6 16	0.007 0.020	[28]
Ferrierite	FER	6.2	0.42	O_2	723	24	473 423	15 15	H_2O: ACN solution	12 1.6	0.012	[28]
Beta	BEA	9.8	0.50	O_2	723	24	473 423	15	H_2O: ACN solution	4.2 1.6	0.005 0.002	[28]
ZSM-5	MFI	12	0.58	O_2	773	24	473	15	H_2O:ACN solution	8.2	0.011	[28]
ZSM-5	MFI	12	0.54	N_2O	723	24	398	20	H_2O @ 293 K	14	0.021	[39]
ZSM-5	MFI	17.5	0.4	Air	823	-	423	25	Ethanol	1.69	0.005	[29]

Table 1.2. Experimental results for 3-step process (Continued)

Material	IZA Code	Si/Al	Cu/Al	Oxidant	O_2 Activation		Reaction		Extraction	Methanol Produced (μmol CH_3OH g_{cat}^{-1})	Methanol/Cu (mol mol^{-1})	Ref
					Temperature (K)	Duration (h)	Temperature (K)	Duration (min)				
Mordenite	MOR	11	0.38	O_2	723	4	473	20	He/ H_2O flow @ 473 K	13	0.025	[40]
ZSM-5	MFI	12 12	0.28 0.28	NO NO_2	423 573	2 2	423 423	60 60	Ar/ H_2O flow @ 423 K	0.629 0.690	0.002 0.002	[41]
Mordenite	MOR	11	0.4	O_2	723	1	473	240	He/ H_2O flow @ 408K	135	0.243	[42]
SSZ-13	CHA	12	0.35	O_2	723	10	473	20	N_2/H_2O flow @ 473 K	31	0.060	[32]
SSZ-16	AFX	6.5	0.34	O_2	723	10	473	20	N_2/H_2O flow @ 473 K	39	0.050	[32]
SSZ-39	AEI	10	0.26	O_2	723	10	473	20	N_2/H_2O flow @ 473 K	16	0.090	[32]
Mordenite	MOR	5	0.34	O_2	723	10	473	20	N_2/H_2O flow @ 473 K	31	0.040	[32]
ZSM-5	MFI	11.5	0.34	O_2	723	10	473	20	N_2/H_2O flow @ 473 K	16	0.030	[32]
SAPO-34	CHA	6	0.6	O_2	723	10	473	20	N_2/H_2O flow @ 473 K	15	0.010	[32]
Mordenite	MOR	8.5 8.5	0.38 0.30	O_2 O_2	723 723	40 40	473 473	30 30	H_2O/ He flow @ 473 K H_2O/ He flow @ 473 K	17.8 14.3	0.031 0.047	[43]

Table 1.2. Experimental results for 3-step process (Continued)

Material	IZA Code	Si/Al	Cu/Al	Oxidant	O_2 Activation		Reaction		Extraction	Methanol Produced (μmol CH_3OH g_{cat}^{-1})	Methanol/Cu (mol mol^{-1})	Ref
					Temperature (K)	Duration (h)	Temperature (K)	Duration (min)				
Mordenite	MOR	6 6	0.32 0.32	O_2 O_2	723 473	4 13	473 473	30 30	H_2O @ 298 K H_2O @ 473K	14.4 0.3	0.139 0.076	[34]
ZSM-5	MFI	15	0.43	O_2	473	13	473-32bar	30	H_2O @ 298 K	17.7	0.040	[34]
Zeolite Y	FAU	3	0.31	O_2	473	13	473-32bar	30	H_2O @ 298 K	10.5	0.009	[34]
ZSM-5	MFI	14	0.67	O_2	723	1	473	480	H_2O/ He flow @ 408 K	89	0.120	[44]
Mordenite	MOR	10 10 10	0.27 0.27 0.27	O_2 O_2 O_2	723 823 923	8 8 8	473 473 473	60 60 60	H_2O @ 298 K	37.3 55.3 65.2	0.091 0.135 0.160	[45]
Mordenite	MOR	13	-	H_2O	673	2	473	30	H_2O/ He flow @ 473 K	-	0.202	[38]
SSZ-13	CHA	12	0.49	O_2	773	2	473	360	H_2O flow @408 K	107	0.172	[36]
Mordenite	MOR	20	0.4 0.4	O2 O2	723 873	2	423	60	H_2O/ N_2 flow @ 408 K	67 69	0.211 0.218	[46]
Mordenite	MOR	5	0.28	O_2	723	4	473	30	H_2O @ 298 K	31.2	0.040	[37]
ECR-1	EON	3.5	0.33	O_2	723	4	473	30	H_2O @ 298 K	19.7	0.016	[37]

Table 1.2. Experimental results for 3-step process (Continued)

Material	IZA Code	Si/Al	Cu/Al	Oxidant	O_2 Activation		Reaction		Extraction	Methanol Produced (μmol CH_3OH g_{cat}^{-1})	Methanol/Cu (mol mol^{-1})	Ref
					Temperature (K)	Duration (h)	Temperature (K)	Duration (min)				
Omega	**MAZ**	**3.2**	**0.29**	**O_2**	**723**	**4**	**473**	**30**	**H_2O @ 298 K**	**86.1**	**0.075**	[37]
PST-11	MEI	3.4	0.47	O_2	723	4	473	30	H_2O @ 298 K	21.7	0.012	[37]
UZM-4	BPH	3	0.61	O_2	723	4	473	30	H_2O @ 298 K	8	0.003	[37]
ZSM-5	MFI	14	0.65	O_2	723	4	473	30	H_2O @ 298 K	9	0.013	[37]
Ferrierite	FER	8.9	0.38	O_2	723	4	473	30	H_2O @ 298 K	6.7	0.010	[37]
SSZ-13	CHA	20 20 20	0.44 0.22 0.18	O_2 O_2 O_2	723 723 723	2 2 2	473	20	H_2O/ N_2 flow @ 473 K	8.2 6.3 4.9	0.024 0.036 0.034	[47]
Mordenite	**MOR**	**7**	**0.18**	**O_2**	**773**	**6**	**473**	**360**	**H_2O steam**	**170**	**0.450**	[35]
Mordenite	MOR	7 7	0.18 0.24	He He	723 723	0.33 0.33	473 473	120 120	H_2O steam	-	0.21 0.11	[35]
Mordenite	MOR	15	3.5 2.69	O_2 O_2	723 723	2 2	473 473	30 30	H_2O @ 298 K H_2O @ 298 K	60 39	0.016 0.014	[48]

Table 1.2. Experimental results for 3-step process (Continued)

Material	**IZA Code**	**Si/Al**	**Cu/Al**	**Oxidant**	**O_2 Activation**		**Reaction**		**Extraction**	**Methanol Produced (μmol CH_3OH g_{cat}^{-1})**	**Methanol/Cu (mol mol^{-1})**	**Ref**
					Temperature (K)	Duration (h)	Temperature (K)	Duration (min)				
Mordenite	MOR	6.5	7 5.7	O_2 O_2	723 723	2 2	473 473	30 30	H_2O @ 298 K H_2O @ 298 K	42 102	0.002 0.008	[48]
Mazzite	MAZ	3.2	3.62	O_2	723	2	473	30	H_2O @ 298 K	86.1	0.006	[48]
Chabazite	CHA	15.8	6.43	O_2	723	2	473	30	H_2O @ 298 K	32.5	0.005	[48]
Ferrierite	MFI	23	12.13	O_2	723	2	473	30	H_2O @ 298 K	12	0.001	[48]
Chabazite	**CHA**	**12**	**0.5**	**O_2**	**773**	**8**	**473**	**360**	**H_2O @ 298 K**	**125**	**0.202**	[36]

1.6.2 Catalytic Methane to Methanol

3-step process is known to give very high methanol selectivity; however, prolonged cycle-times and changes in temperature and pressure of the process inhibits implementation in industry. Instead, catalytic production of methanol under continuous flow of methane, oxidant and water vapour is highly needed.

In the catalytic process the reactions given below are considered to be realized (Eq 2.1–2.4).

$$N_2O + 2Cu^{+2}\text{-Zeolite} \longrightarrow N_2 + Cu_xO_y \quad \text{Eq 2.1}$$

$$CH_4 + Cu_xO_y\text{-Zeolite} \longrightarrow CH_3OH \quad \text{Eq 2.2}$$

$$2CH_3OH \longrightarrow H_2O + CH_3OCH_3 \quad \text{Eq 2.3}$$

$$CH_3OH \longrightarrow HCOH \longrightarrow HCOOH \longrightarrow CO_2 + H_2O \quad \text{Eq 2.4}$$

First continuous MTM reaction using molecular oxygen as an oxidant have been studied by Narsimhan et al. Catalytic performance of different zeolites and zeo-type materials such as MFI, FER, MOR, BEA, CHA, FAU and MCM-41 were tested and results are given in Table 1.3. Ipek et al. have performed continuous reaction using N_2O as an oxidant using copper exchanged SSZ-13, increased selectivity towards methanol improved by increasing methane and water partial pressures [49].

The challenge in the catalytic process is to avoid excessive oxidation of the resulting methanol, typically limiting the reaction conversion to 0.001% – 0.1% for selectivity of >10% methanol. Higher conversions (>10%) lead to a significant increase in the formation of undesirable over-oxidation products, which are CO and CO_2. Cu/Fe-ZSM-5 catalyst also has been tested using H_2O_2 as an oxidant and has shown high selectivity and conversion values (92% and 0.5%) under on-flow conditions [50]. Recently, Dinh et al. found that with high water and methane partial pressures high selectivity can be achieved. Also, it is reported that methanol production activity per

copper could be maximized when zeolites having high Al content and low Cu loadings are used. Catalytic results were summarized in Table 1.3.

Table 1.3. Cu-zeolites used in catalytic process

Material	IZA Code	Si/Al	Cu/Al	Oxidant	Reaction Temperature	Gas Composition	Methanol Produced (µmol CH_3OH h^{-1} g_{cat}^{-1})	Methanol Selectivity (%)	TOF CH_3OH (h^{-1})	Ref
H-Cu-ZSM-5	MFI	13.2	0.37	O_2	483	88.9 kPa CH_4, 0.025 kPa O_2, 3.2 kPa H_2O.	1.79		0.0052	[51]
Na-Cu-ZSM-5	MFI	13.6	0.31	O_2	483	88.9 kPa CH_4, 0.025 kPa O_2, 3.2 kPa H_2O.	0.88	70.6	0.0022	[51]
Beta	BEA	13.3	0.30	O_2	483	88.9 kPa CH4, 0.025 kPa O_2, 3.2 kPa H2O.	0.80		0.0024	[51]
Mordenite	MOR	10	0.14	O_2	483	88.9 kPa CH_4, 0.025 kPa O_2, 3.2 kPa H_2O.	0.84		0.0046	[51]
Ferrite	FER	10	0.12	O_2	483	88.9 kPa CH_4, 0.025 kPa O_2, 3.2 kPa H_2O.	0.44		0.0027	[51]
Zeolite Y	FAU	5.1	0.45	O_2	483	88.9 kPa CH_4, 0.025 kPa O_2, 3.2 kPa H_2O.	0.30		0.0003	[51]
SSZ-13	CHA	13.8	0.50	O_2	483	88.9 kPa CH_4, 0.025 kPa O_2, 3.2 kPa H_2O.	0.84		0.0079	[51]
MCM-41	MCM-41	12	0.74	O_2	483	88.9 kPa CH_4, 0.025 kPa O_2, 3.2 kPa H_2O.	0.36		0.0060	[51]
SSZ-13	CHA	12	0.40	N_2O	543	30.4 kPa CH_4, 30.4 kPa N_2O, 3.2 kPa H_2O, 37.3 kPa He	28	15.8	0.35*	[49]

Table 1.3. Cu-zeolites used in catalytic process (Continued)

Material	IZA Code	Si/Al	Cu/Al	Oxidant	Reaction Temperature	Gas Composition	Methanol Produced (µmol CH_3OH h^{-1} g_{cat}^{-1})	Methanol Selectivity (%)	TOF CH_3OH (h^{-1})	Ref
SSZ-13	CHA	12	040	N_2O	573	30.4 kPa CH_4, 30.4 kPa N_2O, 3.2 kPa H_2O, 37.3 kPa He	55	2.3	4.80*	[49]
SSZ-13	CHA	12	0.18	N_2O	543	30.4 kPa CH_4, 30.4 kPa N_2O, 3.2 kPa H_2O, 37.3 kPa He	33	39.7	0.36*	[49]
H-Cu-Mordenite	CHA	5	0.08	O_2	543	30.4 kPa CH_4, 30.4 kPa N_2O, 3.2 kPa H_2O, 37.3 kPa He	10	24	0.26*	[49]
Na-Cu-Mordenite	CHA	5	0.33	O_2	543	30.4 kPa CH_4, 30.4 kPa N_2O, 3.2 kPa H_2O, 37.3 kPa He	2	1.1	0.24*	[49]
H-Cu-ZSM-5	CHA	10	0.38	O_2	543	30.4 kPa CH_4, 30.4 kPa N_2O, 3.2 kPa H_2O, 37.3 kPa He	6	0.3	3.80*	[49]
SSZ-13	CHA	23	0.22	O_2	543	18 kPa CH_4, 0.09 kPa O_2, 3.14 kPa H_2O, 79.8 kPa He	6	~1	-	[52]
SSZ-13	CHA	8.8	0.19	O_2	543	18 kPa CH_4, 0.09 kPa O_2, 3.14 kPa H_2O, 79.8 kPa He	3	~1	-	[52]
SSZ-13	CHA	76	0.23	O_2	543	18 kPa CH_4, 0.09 kPa O_2, 3.14 kPa H_2O, 79.8 kPa He	3.6	~1	-	[52]

*TOF (h^{-1}) for methane

1.7 Active Sites for Methane to Methanol Reaction

Various possible active sites stem from differences in zeolite topologies, zeolite Si/Al and Cu/Al ratios, using different kind of oxidants or activation at different temperatures as seen in Table 1. One challenge in Cu-exchanged zeolites is that, oxidation usually creates various kinds of copper species and it makes the active site identification quite difficult. Groohaert et al. reported the first activity for selective oxidation of methane to methanol on O_2 activated Cu-zeolites in 2005. Activation of methane has been displayed on zeolites with the UV–visible absorption band of 22,700 cm^{-1}. O_2 treatment has increased the intensity of this band and methane reaction caused a decrease in the intensity. This active site on Cu-ZSM-5 has been assigned as a bis(μ–oxo)dicopper(III) species [31]. After that, Smeets et al investigated the stability of the bis(μ–oxo)dicopper(III) species and found that MFI and MOR structures can stabilize this core with a methanol yield varied from <1 to 8.2 μmol per gram zeolite. In addition, the high correlation between the intensity of UV–visible band and the extracted methanol yield demonstrated once again that bis(μ–oxo)dicopper(III) core is the active site in the MTM reaction [28]. In 2009, Woertnik et al. reported that the active species showing the UV–visible absorption band at 22,700 cm^{-1} in Cu-ZSM-5 showed resonance Raman vibrations at 456 cm^{-1} and 870 cm^{-1} and therefore they designated these vibrations as symmetric and asymmetric Cu–O stretching vibrations of a mono–(μ–oxo)dicopper(II) species [39]. In DFT calculations, Cu-oxo active site is clearly identified as a bent mono–(μ–oxo)dicopper(II) on ZSM-5. Also the group found that, activation of Cu-ZSM-5 with N_2O (373 K) resulted in the formation of this core at lower temperature than O_2 (448 K) and helium (723 K). Quantitative relation between the intensity of 22,700 cm^{-1} band and amount of methanol production was investigated by Beznis et al. They have found that in ZSM-5, at least two copper-oxo species were present. The first species is Cu–O clusters that are not involved in the reaction on the outer surface of the zeolite, and the second are highly dispersed Cu-oxo species within the zeolite channels responsible for the conversion of methane to methanol [29].

Grundner et al. suggested that the MOR topology can stabilize trinuclear copper-oxo clusters, which are responsible for the high activity of the MTM reaction on Cu-MOR zeolites [42]. According to the DFT calculations, Cu-SSZ-13 with low Si/Al ratios, $[Cu(II)OH]^+$ species in 8 MR have also been recommended as active sites for the MTM reaction [53]. However due to the lack of methanol formation activity at conditions favor the concentration of Z[Cu(II)OH] species, these species have later been considered to be the precursor of active sites for MTM reaction [36].

Some recent results showed that larger sized CuO_x species are possibly formed during MTM reaction. Based on DFT calculations, Palagin et al. have studied the stabilities of different sizes of CuO_x clusters in MOR zeolites. It was found that the ground-state structures for stoichiometric tetramers or pentamers of $Cu_nO_n^{2+}$ and $Cu_nO_{n-1}^{2+}$ incorporated into 8 MR of MORs are relatively more stable than those for smaller [54]. In addition, the localization and the content of the framework aluminum in zeolites also play an immense role in the natures and stabilities of CuO_x species [54]. Newton et al. have investigated Cu exchanged zeolites with different copper active sites in MOR, MAZ, CHA and MFI zeolites based on *in situ* copper K-edge for both the high-temperature activation (723 K in flowing oxygen) and the isothermal activation (activation at 473 K in flowing oxygen followed by pressurization in methane to between 6 and 15 bar). The results confirm a two-electron mechanism for MTM reaction on Cu–zeolites based on the Cu(I)/Cu(II) redox couple rather than any other mechanism, such as a Cu(II)/Cu(III) couple or one that proceeds via a Cu(II)–O radical species [48].

Table 1.4. Proposed active site motifs for Cu-exchanged zeolites

Active Site Motif		Zeolite	Reference
Bis(μ-oxo) dicopper(III), $[Cu(\mu O)_2Cu]^{2+}$	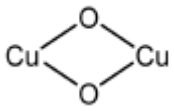	MOR, MFI	[31], [28]
Trans-μ-1,2-peroxo dicopper(II) $[Cu_2(trans\text{-}\mu\text{-}1,2\text{-}O_2)]^{2+}$	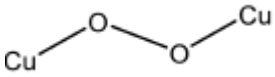	MOR, CHA	[55] [20]
Mono-(μ-oxo) dicopper(II), $[Cu_2(\mu O)]^{2+}$	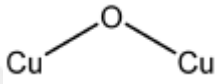	MFI, MOR,CHA	[39],[20], [56]
$[Cu_3(\mu O)_3]^2$		MOR, MFI	[42]
$[Cu–OH]^+$		CHA	[42],[57],[58]
Copper oxide clusters		MOR, MFI	[59]

1.8 Objective

The aim of this project is to increase the methanol production rate and selectivity in continuous catalytic methanol production process using Cu-exchanged zeolites. Also, optimization of the feed gas composition and reactant partial pressures is within the scope of this thesis. The effect of framework as well as introduction of mesoporosity in methanol selectivity are investigated. Using microporous Mordenite and SSZ-39 zeolites, we optimized the N_2O, CH_4 and H_2O partial pressures; furthermore, we investigated the activation energy of the reaction. Study also contains the characterization of zeolites utilized in this thesis.

CHAPTER 2

EXPERIMENTAL PROCEDURE

2.1 Catalyst Synthesis and Ion Exchange

In this thesis, three zeolites; SSZ-13 (Si/Al = 9), SSZ-39 (Si/Al = 6) and omega (Si/Al = 3) were synthesized in the laboratory. The ammonium form of Mordenite (NH_4^+-MOR, Si/Al=10) was commercially obtained from Alfa-Aesar. Following the Cu(II)-exchange process, obtained or synthesized zeolites were used for catalytic methane to methanol reaction in a continuous flow set-up.

2.1.1 Synthesis of Microporous SSZ-13

A sample of CHA zeolite (SSZ-13) was hydrothermally synthesized using similar procedure reported by Pham et al. [60] with a gel mixture having a molar composition of 1 SiO_2: 0.035 Al_2O_3: 0.5 TMAdaOH: 20 H_2O. Briefly, 26.969 g of *N*,*N*,*N*-trimethyl-1-adamantanamonium hydroxide solution (TMAdaOH, Sachem, 20 wt.%) as structure directing agent and 0.597 g aluminum ethoxide (Sigma Aldrich, 97wt.%) as Al- source were stirred for 15 minutes at room temperature to dissolve the aluminum ethoxide. After that, 10.850 g tetraethyl orthosilicate (TEOS, Merck, 98 wt.%) were added to the mixture as silicon source and stirred for 1 hour at 298 K. The resulting mixture was transferred to the 35 mL Teflon-lined autoclaves and subjected to hydrothermal treatment at 423 K for 7 days under autogenous pressure in static oven. Hydrothermally produced crystals were recovered by vacuum filtration, washed with 500 mL de-ionized water and dried at 353 K overnight. Calcination was performed in a flow furnace with 15 cm^3 min^{-1} dry air flow at 853 K for 6 h (using a heating rate of 1 K min^{-1}) following drying at 393 K for 2 h.

2.1.2 Synthesis of Mesoporous SSZ-13

Mesoporous SSZ-13 was synthesized using a gel formula of 1 SiO_2: 0.025 Al_2O_3:0.1 Na_2O 0.2 TMAdaOH: 44 H_2O: 0.12 CTABr [58]. First of all, 38.977 g *N*,*N*,*N*-trimethyl-1-adamantanamonium hydroxide (TMAdaOH, Sachem, 20 wt.%), which was employed as the structure directing agent was mixed with 0.979 g sodium hydroxide pellets (NaOH, Merck, 99 wt.%) and 114.879 g de-ionized water until a clear solution was obtained. After that, 11.079 g fumed silica (Sigma Aldrich, 99.8wt.%) as silicon source was added very slowly to the solution and stirred until a homogeneous solution was obtained. Finally, 0.855 g sodium aluminate (Sigma Aldrich, 53wt.% Al_2O_3) as alumina source was added. The gel was stirred for two hours at 298 K to obtain a homogeneous gel. The initial gel was transferred into 35 mL Teflon-lined autoclaves and kept at 433 K for one day. After one day, 1.646 g cetyltrimethylammonium bromide (Sigma Aldrich, 98 wt.%, CTABr) as mesoporogen (SiO_2:CTABr=0.12) was mixed completely with the solution. The final gel that contains CTABr was transferred back into the Teflon-lined autoclaves and hydrothermal treatment was performed at 433 K for 11 more days under static conditions. The sample was collected using vacuum filtration, washed vigorously with de-ionized water and dried at 353 K overnight. The zeolite calcined at 853 K for 10 h in a muffle furnace using a heating rate of 1 K min^{-1} following drying at 393 K for 90 min.

2.1.3 Synthesis of Microporous SSZ-39

A sample of AEI type zeolite (SSZ-39) was hydrothermally synthesized by stirring 6.690 g of tetramethyl piperidinium hydroxide (Sachem, Inc., 35.3 wt.%) as structure directing agent, 17.671 g of de-ionized water, 12.840 g of sodium silicate solution (Merck, 37 wt.%) and 1.026 g 1 M NaOH solution for 15 minutes at 298 K. After obtaining a clear solution, 4.490 g NH_4-USY (Alfa Aesar, Zeolite Y, Si/Al =12) was added very slowly to the mixture and the stirring continued for 30 minutes [20]. The

synthesis gel was then transferred to 35 mL Teflon-lined autoclaves and hydrothermally treated at 423 K for 7 days under tumbling at 45 rpm. Hydrothermally produced crystals were recovered by vacuum filtration, washed with 500 mL de-ionized water and dried at 353 K overnight. Calcination was performed in a flow furnace under 15 cm^3 min^{-1} dry air flow at 833 K for 8 h (using a heating rate of 1 K min^{-1}) following drying at 393 K for 2 h.

2.1.4 Synthesis of Mesoporous SSZ-39

Mesoporous SSZ-39 was synthesized using CTABr as mesoporogen. Firstly, 6.690 g tetramethyl piperidinium hydroxide (Sachem, Inc., 35.3 wt.%), which was used as structure directing agent, was mixed with 17.671 g de-ionized water. After that, 12.840 g sodium silicate solution (Merck, 37 wt.%) as silica source and 1.026 g 1 M NaOH solution was added and stirred for 30 minutes in order to form a homogeneous solution. Afterwards, 2.566 g NH_4-USY (Alfa Aesar, Zeolite Y, Si/Al =6), which was employed as silicon and alumina source was added very slowly to the solution and stirred for 45 minutes. The initial gel was transferred into a 35 mL Teflon-lined autoclaves and kept at 423 K under tumbling at 45 rpm for 1 day and after 1 day, 3.462 g cetyltrimethylammonium bromide (Sigma Aldrich, 98 wt.%, CTABr) as mesoporogen (SiO_2:CTABr=0.12) was mixed with the solution. Final gel containing CTABr was transferred into the Teflon-lined autoclaves again and heated at 423 K for 6 more days under rotation 45 rpm. The crystals were collected using vacuum filtration, washed vigorously with de-ionized water and dried at 353 K overnight. The zeolite calcined at 853 K for 16 h using a heating rate of 1 K min^{-1} in a muffle furnace following drying at 393 K for 90 min.

2.1.5 Synthesis of Omega

The synthesis of MAZ type zeolite (Omega) was performed using a gel mixture of 0.24 Na_2O: 0.1 Al_2O_3: 1 SiO_2: 0.024 TMAOH: 0.012 H_2O following a similar

procedure given by Gossens et al. [61]. Firstly, 2.117 g tetramethyl ammonium hydroxide (Merck, 25 wt. %) as structure directing agent, 11.476 g de-ionized water, 1.020 g NaOH (Merck, 99 wt. %) and 2.242 g sodium aluminate as Al- source were added respectively and stirred at 298 K for 15 minutes. After obtaining a clear solution, 18.144 g of colloidal silica (Ludox HS 40 wt %) was added to the solution as silicon source. Solution was aged for 3 days at room temperature under stirring. The final gel was then transferred to 35 mL Teflon-lined autoclaves and hydrothermally treated at 373 K for 15 days under autogenic pressure and static conditions. Hydrothermally produced crystals were recovered by vacuum filtration, washed with 500 mL de-ionized water and dried at 353 K overnight. Calcination was performed in a flow furnace under 15 cm^3 min^{-1} dry air flow at 823 K for 16 h (using 1 K min^{-1} heating rate) following drying at 393 K for 2 h to remove water and organic species and finally cooled down to the room temperature.

2.1.6 Ammonium Exchange Procedure

NH_4^+-SSZ-39 (or omega) was obtained by ion-exchange using 1–3 g of calcined SSZ-39 in 500 mL of 0.2 M ammonium nitrate (NH_4NO_3, Sigma Aldrich, 99 wt %,) aqueous solution (500 mL de-ionized water and 8 g NH_4NO_3). The solution was stirred for 3 hours at a temperature of 353 K for exchange. After three hours, zeolites were vacuum filtered using cellulose acetate membrane filters having a pore size of 200 nm, washed with 500 mL de-ionized water and dried at a temperature of 353 K in air for 30 minutes. This exchange procedure was repeated using the same zeolite and a new 0.2 M ammonium nitrate solution for three times. Finally, NH_4^+-exchanged zeolite was heat treated at 823 K for 5 h following drying at 423 K for 1.5 h. Resulting zeolite is denoted as H^+-SSZ-39 or H^+-Omega (Eq 2.1).

$$NH_4^+ — \text{Zeolite} \longrightarrow H^+ — \text{Zeolite} — NH_3 \qquad \text{Eq 2.1}$$

2.1.7 Dealumination Procedure

A dealumination protocol to Mordenite reported elsewhere [62] was followed to obtain mesoporous mordenite. In a typical three step run, the first step is acid treatment. 1 g of proton form of the zeolite was stirred in 20 mL 2 M aqueous HNO_3 solution at 373 K for 2 hours. The slurry was vacuum filtrated, washed thoroughly with de-ionized water and the filter cake was calcined at 823 K for 5 hours. In the second step, the sample was refluxed with 0.2 M of NaOH solution, (20 mL solution per gram of zeolite) at 343 K for half an hour. The sample was vacuum filtered and washed with de-ionized water. Finally, the resulting zeolite was refluxed with 0.2 M of HNO_3 solution at 323 K for 1.5 hour. The final product was ammonium-exchanged (three times) and then heat-treated at 823 K for 5 hours to obtain H^+-mesoporous mordenite.

2.1.8 Cu(II)-Exchange of Zeolites

Copper exchange was performed by exchanging the H^+ form of the zeolites in copper (II) acetate solution at 298 K. 1 g H^+-zeolite was exchanged with Cu(II) in 250 mL of copper (II) acetate·H_2O (Merck, >99 wt.%) solution at room temperature for 6 h to obtain Cu(II)-zeolite. The volume of the solution was kept constant at 250 mL, while the amount of required copper (II) acetate in the solution varied depending on the mass of zeolite and starting Cu/Al ratio (0.35 or 0.70) in the solution. After exchange, resulting Cu(II)-zeolites were filtered, washed with 500 mL de-ionized water and dried at a temperature of 353 K for overnight. Finally, Cu(II)-exchanged zeolites were heat-treated at 723 K for 4 h using a heating rate of 2 K min^{-1} to eliminate any acetate from the zeolites following drying at 423 K for 1 h. Resulting zeolites were denoted as Cu(II)-Zeolite.

The exact exchange details can be found in Table 2.1, which also provides an overview of the different Cu-materials under study.

Table 2.1. Cu(II)-exchange details at 298 K for 6 h

Zeolite	Si/Al	Starting Cu(II) concentration (M)	Starting Cu/Al in solution
Micro-H^+-Mordenite	10	0.002	0.35
Meso- H^+-Mordenite	16	0.001	0.35
Micro- H^+-SSZ-13	9	0.002	0.35
Meso- H^+-SSZ-13	16	0.001	0.35
Micro- H^+-SSZ-39	6.3	0.003	0.35
Meso- H^+-SSZ-39	15	0.003	0.70
H^+-Omega	3.6	0.004	0.35

2.2 Characterization Techniques

In order to understand the phases and phase purities of the synthesized zeolites, X-Ray Diffraction (XRD) analysis was performed. To calculate the surface areas, pore volumes and to investigate pore size distributions, N_2 adsorption experiments at 77 K were performed. The morphology of the zeolites were analysed using Scanning Electron Microscopy (SEM). The elemental compositions of the zeolites were examined using Inductively Coupled Plasma-Optical Emission Spectrometry (ICP-OES) methods as well as Energy Dispersed X-ray Spectroscopy (EDX). Finally, with the aim of understanding the active sites of the Cu-zeolites, Raman spectroscopy was performed.

2.2.1 X-Ray Diffraction Analysis

X-ray diffraction data were obtained after calcination of the samples. Powder XRD patterns of calcined zeolites were recorded using a Rigaku Ultima-IV X-ray diffractometer (40 kV, 30 mA) equipped with Cu Kα radiation, (λKα =1.5418 Å) in the 2θ range of 2–50° with a scanning speed of 1˚min^{-1} at Central Laboratory, METU.

2.2.2 Textural Analysis

The surface areas and pore volumes of the samples were determined using N_2 adsorption/desorption isotherms obtained at 77 K. N_2 physisorption isotherms were obtained using a surface area and pore volume analyzer Micromeritics Tristar II 3020 located in the Chemical Engineering Department, METU. The degassing process preceding the N_2 adsorption experiment was performed using Micromeritics VacPrep 061. The samples were previously degassed at 573 K for 6 h under vacuum conditions before N_2 (Oksan, 99.999 %) adsorption. The N_2 adsorption/desorption experiment was performed using P/P_0-relative pressure values of N_2 (Oksan, 99.999%) between 10^{-5} and 0.99 and the temperature were kept constant at 77 K using liquid nitrogen. The t-plot method was used to calculate the micropore volume (V_{micro}) of the prepared samples [63]. The mesopore volumes were calculated by subtracting the t-plot micropore volume from the single point pore volume obtained at P/P_0=0.98. Langmuir surface area of the samples were also obtained and presented. The pore size distributions were evaluated using Barret-Joyner-Halenda (BJH) Adsorption model [64].

2.2.3 Morphology Analysis

Morphology of the calcined samples were determined using Scanning Electron Microscopy (SEM) on a QUANTA 400F Field Emission microscope operated at 20 kV. The samples were coated by Pd-Au mixture prior to analysis.

2.2.4 Elemental Analysis

Elemental compositions of samples were determined using inductively coupled plasma-optical emission spectrometer (Perkin Elmer Optime4300DV, ICP-OES) at METU Central Laboratory. The samples were first dissolved with HF/HNO_3 solution overnight. Si, Al and Cu(II) contents of the samples were also determined utilizing

Energy Dispersive X-ray spectra (EDX) QUANTA 400F Field Emission SEM at METU Central Laboratory. EDX operated at the voltage of 20 kV by scanning at least 4 different regions.

2.2.5 Raman Spectroscopy

The dispersive Raman spectra was obtained using a Raman microscope spectrometer at Central Laboratory, Middle East Technical University (Renishaw/Invia) equipped with a 532 nm laser source and a CCD detector. Raman spectra were collected using 50–100 mW of laser power, 20 seconds of integration time over a range of 100–1300 cm^{-1}. Raman spectra were obtained at ambient conditions for the sealed samples.

N_2O activation procedure: About 0.05 grams of hydrated powder form of Cu-zeolites were placed into the NMR reactor. Zeolite was loaded between quartz wool in the NMR tube and placed in the middle of the furnace heating zone. The total flow rate of the feeding mixture was set to the 40 cm^3 min^{-1}. The feed was involved 15 % nitrous oxide and balance helium. To heat the reactor, heater with a Ordel PC771 temperature controller was used. The temperature of the system was increased to 573 K with a heating rate of 10 K min^{-1} and kept constant at this temperature for 2 hours. After that, the temperature was cooled down to the 323 K and flow of the N_2O was stopped while helium flow was being continued. The gas inlet and outlet of the NMR tube was flame sealed with helium at approximately 318 K.

2.3 Catalytic Methane to Methanol Conversion Tests

2.3.1 Reaction Set-up

Methane to methanol reaction was conducted in a quartz tubular reactor having 7 mm inner diameter and 9 mm outer diameter. The reactor was mounted on an oven

and oven temperature was controlled using a thermocouple wrapped around the quartz reactor near the center of the catalyst bed with Ordel PC771 temperature controller. Zeolite powder was pressed into pellets at a pressure of 60 bar for 4 minutes and sieved into 250–450 μm particle size. Particle size was an important parameter since it would affect both the pressure drop and mass transfer rate. Zeolites were packed between quartz wool plugs in the reactor and placed in the middle of the furnace heating zone. The catalyst bed length was kept approximately 1 cm. The flow rates of gases which are helium (Hatgaz, 99.999% purity), nitrous oxide (Hatgaz, 99%) and methane (Hatgaz, 99.995%) were controlled by separate mass flow controllers (ALICAT, MC-100SSCM-D). Water was introduced into the feed gas stream by directing gas stream to a water bubbler maintained at room temperature that resulted in 3.2 kPa H_2O pressure at 298 K. In order to increase the water partial pressure, H_2O saturator was heated to 320 K (10.1 kPa at 320 K). All the gas lines are heated at >343 K to prevent any condensation. The effluent stream was directed into a gas chromatograph (GC, Agilent7820A) with Pora-Plot Q column (CP7554, 25 m, 0.53 mm, 20 μm) and CP- Molsieve 5Å column (CP7538, 25 m, 0.53 mm, 50 μm) equipped with thermal conductivity detector and flame ionization detector, seen in Figure 2.1.

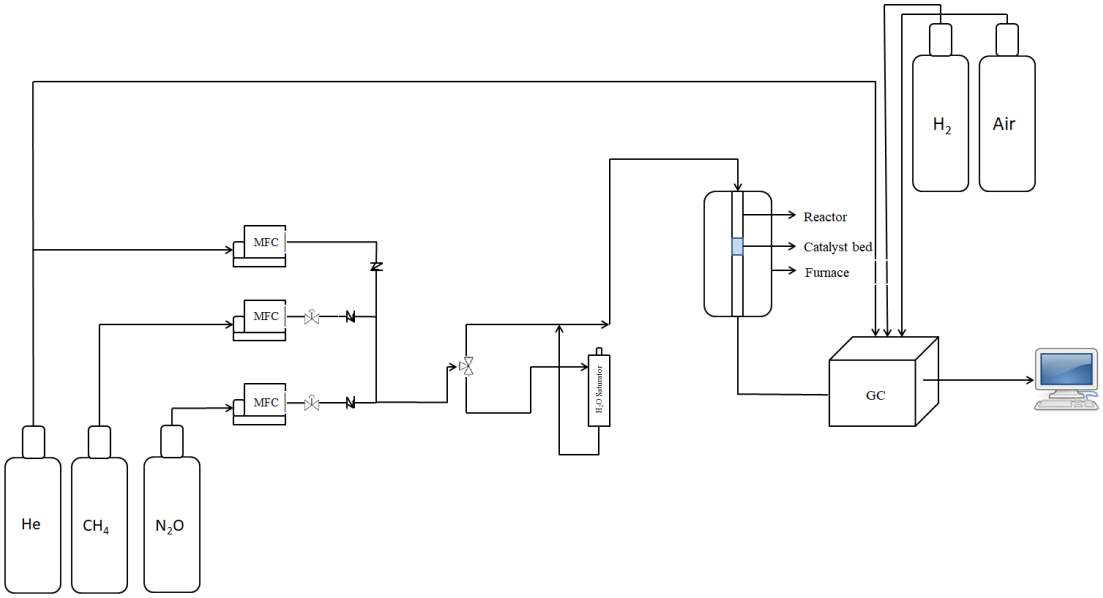

Figure 2.1. Experimental set-up of methane to methanol reaction system

Gas chromatograph (GC) was used for quantification of methanol and the other gases produced. A thermal conductivity detector and flame ionization detector were used simultaneously in order to detect the products. The GC method parameters are given in Table 2.2. The qualitative and quantitative analysis of N_2, CO, CO_2, N_2O, CH_4 and dimethyl ether (DME) were performed using single point calibration of a standard gas sample. The methanol calibration was performed by saturating inert He by methanol vapour at 298 K and at 273 K. The response factors are given in Table 2.3.

Table 2.2. Method parameters for gas chromatography method

Gas sample volume	250 µl
Split Ratio	Splitless
TCD Temperature	523 K
FID Temperature	573 K
Column Pressure	21.4 psi
Oven Temperature	323 K for 8 min, 433 K for 3 min (20 K min^{-1})

Table 2.3. Response factors obtained by calibration

Sample	Retention time/ min	TCD Response Factor / ppm area^{-1}	FID Response Factor / ppm area^{-1}
N_2	6.02	7.58	
CH_4	7.35	18.5	1.23
CH_3OH	13.29		1.03
DME	12.16		0.59
CO	2.85	74.4*	
CO_2	3.09	77.5*	

*CO and CO_2 were determined using a different method for which the split ratio was 5 and only Plot-Q column was used.

2.3.2 Reaction Procedure

Approximately 0.300 g hydrated Cu(II)-zeolites having 250–450 μm particle sizes were placed into the quartz reactor. The total flow rate of the feeding mixture was set to the 100 cm^3 min^{-1}. The feed involved different gas composition of methane, nitrous oxide, water vapour and balance helium. First of all, the sample was purged for 20 min with the feed mixture at room temperature and then a single run was taken in order to determine the initial amounts of reactants. Afterwards, reactor was heated to reaction temperature using a 5 K min^{-1} heating rate and kept at this temperature during the reaction. The methanol formation rate versus the time for which the heating starts at t=0 can be seen in Figure B.1. The time=0 in Figures 3.25, 3.26, 3.29 3.22 and 3.33 represents the time at which the reaction temperature was attained. During the reaction, reaction effluent was sent to the gas chromatograph in 21 min intervals. For all Cu(II)-zeolites, reaction temperature of 573 K with a feed composition of 40 mole % CH_4, 10% N_2O, 3% H_2O and balance He composition were selected. In addition, for Micro-Cu-SSZ-39 and Micro-Cu-Mordenite samples at the reaction temperatures of 543 K, 573 K and 598 K and compositions of 40 mole % CH_4, 10% N_2O, 3% H_2O and balance He were chosen. For understanding the

water's effect on reaction, at the reaction temperature of 573 K and 598 K, the composition of 40 mole % CH_4, 10% N_2O, 10% H_2O and balance He were used for Micro-Cu-mordenite and the composition of 40 mole % CH_4, 15% N_2O, 10% H_2O and balance He conditions at 598 K are selected on Micro-Cu-SSZ-39. Detailed experimental conditions could be seen in Table 2.4.

Table 2.4. Experimental conditions used in methane to methanol reaction

Zeolite	**Temperature / K**	**Total Volumetric Flow Rate of Feed / cm^3 min^{-1}**	**CH_4 Partial Pressure / kPa**	**N_2O Partial Pressure / kPa**	**H_2O Partial Pressure / kPa**	**He Partial Pressure / kPa**	**Duration of Reaction / hours**
Micro-Cu-Mordenite	573	100	20.2	10.1	3.2	67.9	2
			30.4			57.7	2
			40.5			47.6	2
			40.5	5.0	3.2	51.2	2
				10.1		47.6	2
				15.2		42.5	2
	598		40.5	10.1	3.2	47.6	2
					10.1	40.7	2
Meso- Cu-Mordenite	573	100	40.5	10.1	3.2	47.6	2
Micro- Cu-SSZ-13	573	100	40.5	10.1	3.2	47.6	2
Meso- Cu-SSZ-13	573	100	40.5	10.1	3.2	47.6	2
Micro- Cu-SSZ-39	573	100	20.2	10.1	3.2	67.9	2
			30.4			57.7	2
			40.5			47.6	2
			40.5	5.06	3.2	51.2	2
				10.1		47.6	2
				15.2		42.5	2
	598		40.5	10.1	2.8	47.9	2
					10.1	40.7	2
Meso-Cu-SSZ-39	573	100	40.5	10.1	3.2	47.6	2
Cu-Omega	573	100	40.5	10.1	3.2	47.6	2

CHAPTER 3

RESULTS AND DISCUSSION

3.1 Characterization Results

3.1.1 XRD Results

The crystal structures of microporous and mesoporous zeolites were determined from powder XRD patterns. Data were recorded in the 2θ range of 2–50° and are given in Figures (3.1–3.4).

X-ray diffraction patterns were recorded in order to determine the crystallinity and phase purity of synthesized zeolites. XRD showed that commercial mordenite, synthesized SSZ-13, SSZ-39 and omega zeolites had high crystallinity with characteristic peaks for MOR, CHA, AEI and MAZ frameworks, respectively. Expected XRD patterns of the zeolites were also given in the figures from literature for comparison [3]. Cu(II)-exchanged zeolites conserved their crystalline structure and Cu(II)-exchange procedure did not create any additional phases (such as CuO) for Mordetine, SSZ-13, SSZ-39 and Omega.

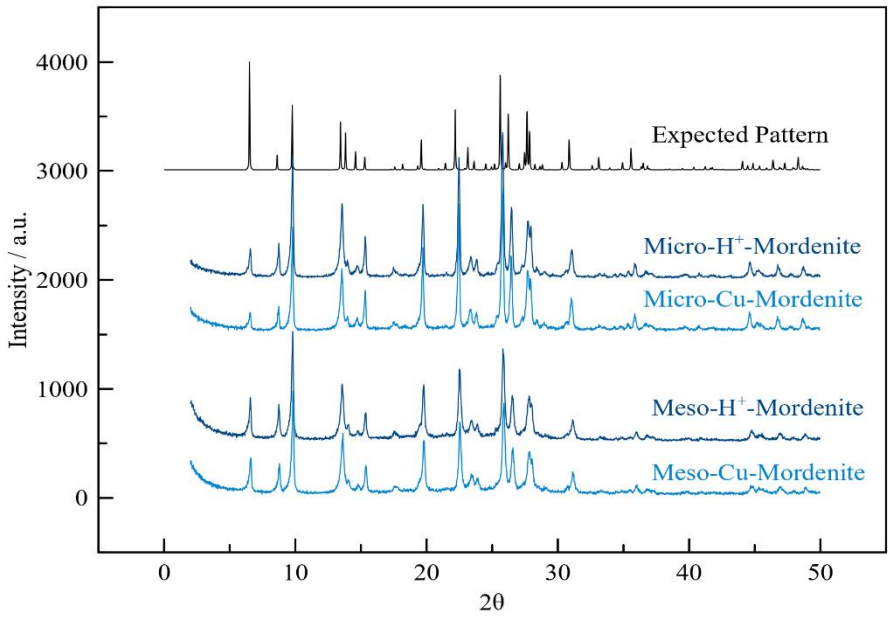

Figure 3.1. Powder XRD patterns of commercial Mordenite and mesoporous Mordenite following Cu-exchange (λ=1.5418 Å)

Mordenite showed high crystallinity with no additional phases in Figure 3.1. In addition, the dealumination process, which consists of acid and alkali treatments for mordenite, did not cause severe crystallinity loss or detectable differences such as additional phases. Mesoporous-mordenite samples have showed lower peak intensity indicating smaller particle sizes resulting from the Al-extraction methods. After ion-exchange, drying, and calcination, no differences were observed corresponding to copper or copper oxide particles. The differences in the relative peak intensity values in the expected pattern and the prepared samples result from the additional Na content in the expected pattern (Na-Mordenite [3]) .

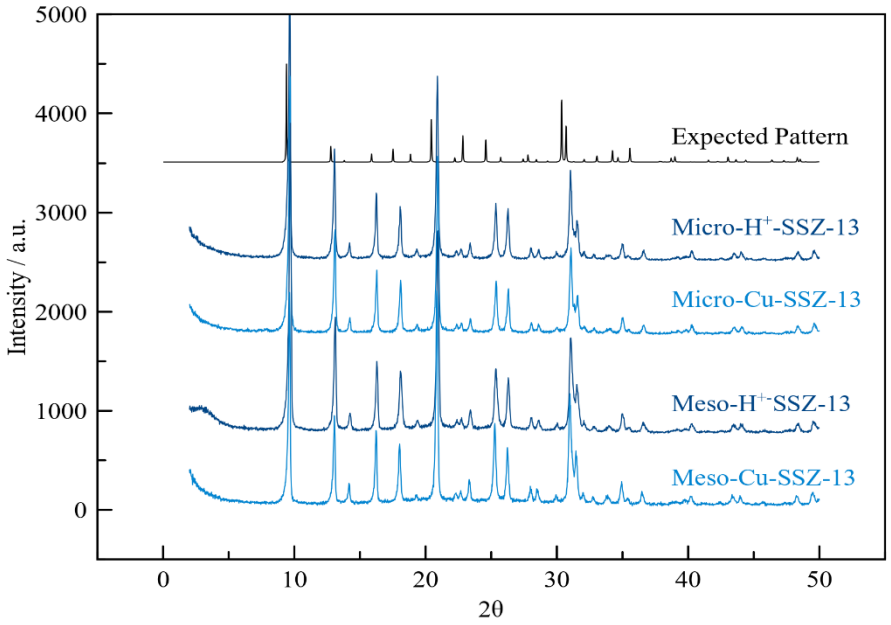

Figure 3.2. Powder XRD patterns of calcined SSZ-13 and mesoporous SSZ-13 following Cu-exchange (λ=1.5418 Å)

**Expected pattern has different unit cell length due to the difference in Si/Al ratio. (Expected pattern has Si/Al=2.15)

SSZ-13 has shown a typical XRD pattern corresponding to CHA framework (see Figure 3.2). Adding mesoporosity using CTABr did not cause any additional peaks; i.e., the mesoporous SSZ-13 was pure material like microporous SSZ-13. Microporous-SSZ-13 and mesoporous-SSZ-13 have exhibited approximately the same intensity, inferring that they have similar particle sizes as seen in Figure 3.2. Furthermore, Cu(II)-exchange caused no drastic changes such as framework collapsing for any of the SSZ-13.

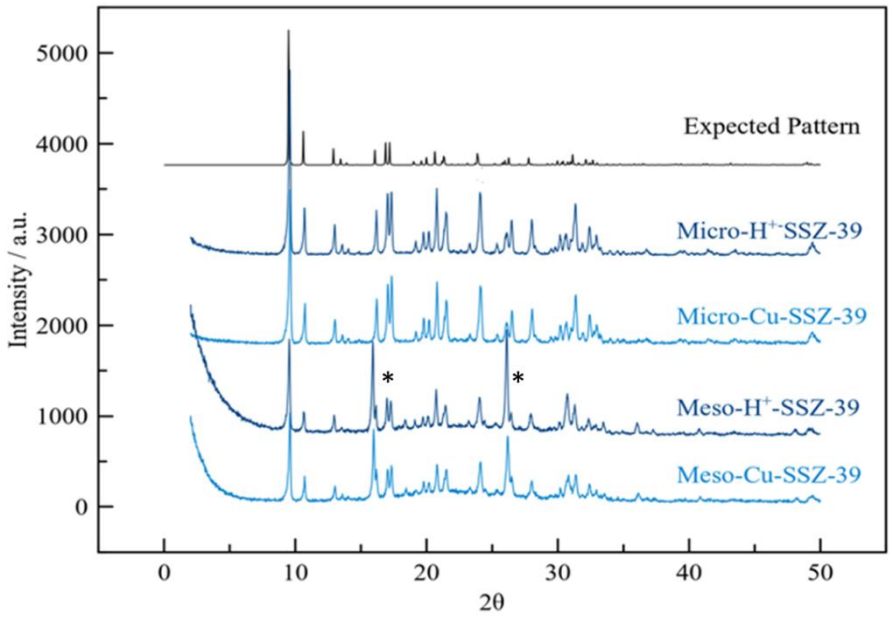

Figure 3.3. Powder XRD patterns of calcined SSZ-39 and mesoporous SSZ-39 following Cu-exchange (λ=1.5418 Å)

Microporous SSZ-39 has also shown high crystallinity with typical characteristic peaks of AEI type framework (see Figure 3.3). XRD patterns for Micro-SSZ-39 showed that no impurities or other zeolitic phases were present. In addition, Cu(II)-exchange did not cause any change in the structure of microporous SSZ-39. However, in mesoporous SSZ-39, the additional peaks at the 2θ of 15.8° and 26. 1° (marked by an asterisk) indicate presence of an extra analcime* (ANA) phase formed during the synthesis of mesoporous SSZ-39. The analcime phase remained following the Cu(II)-exchange (see Figure 3.3) [65]. Shorter peak intensities for mesoporous SSZ-39 indicate smaller particle sizes when compared to microporous SSZ-39.

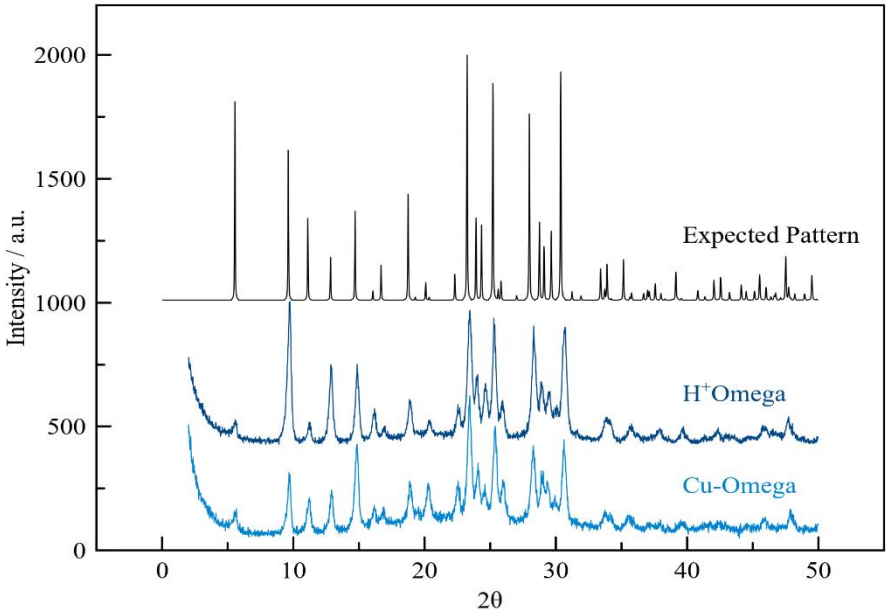

Figure 3.4. Powder XRD pattern of calcined Omega following Cu-exchange (λ=1.5418 Å)

A first overview of the results obtained by XRD showed similar peaks of MAZ type framework with a high crystallinity for Omega (see Figure 3.4). Cu(II)-exchange procedure have led to a small decrease in crystallinity. The reason could be the instability of the H^+-Omega (Si/Al = 3) in Cu(II)-acetate solution.

3.1.2 Elemental Analysis

Elemental analysis of Cu(II)-exchanged micro- and meso- zeolites were obtained using Energy-Dispersive X-ray spectroscopy (EDX) and Inductively Coupled Plasma - Optical Emission Spectrometry (ICP-OES) methods (see Table 3.1. The fact that EDX and ICP-OES results are close to each other shows that homogeneous products are synthesized. Si/Al ratio of microporous zeolites have Si/Al ratios between 3 to 10 and mesoporous zeolites have the Si/Al ratio of 3 to 20 which are compatible with the literature shown in Table 3.1. [17,66–68]

For Meso-H^+- Mordenite, dealumination process for mesopore addition caused a considerable increase in Si/Al ratio. This information confirms the efficiency of the aluminum extraction. For mesoporous SSZ-13 and SSZ-39, higher Si/Al ratios were observed due to the synthesis procedure including CTABr as the mesoporogen [65,69].

Table 3.1.Elemental analysis of H^+-micro- and meso-zeolites

Zeolite	**Si/Al[(a)]**	**Si/Al[(b)]**
Micro-H^+-Mordenite	8.9±0.7	9.7±0.1
Meso- H^+-Mordenite	20±2	16±1
Micro- H^+-SSZ-13	9.7±0.8	11±1
Meso- H^+-SSZ-13	14±2	
Micro- H^+-SSZ-39	6.3±0.4	6.6±0.1
Meso- H^+-SSZ-39	15±2	
H^+-Omega	3.6±0.1	

(a)Elemental analysis performed by EDX

(b)Elemental analysis performed by ICP-OES

Elemental analysis of micro- and mesoporous samples with Cu(II)-exchange were performed with EDX and ICP-OES. According to the elemental analysis results, zeolites containing micro and mesopores after Cu(II)-exchange showed Cu/Al values around 0.2 as targeted. Cu/Al ratios calculated using EDX was found to be in good agreement with the ratios found by ICP-OES. Si/Al and Cu/Al ratios of the Cu(II)-exchanged zeolites are given in Table 3.2.

Table 3.2. Elemental analysis of Cu(II)-exchanged micro- and mesoporous zeolites

Zeolite	Si/Al[(a)]	Cu/Al[(a)]	Si/Al (b)	Cu/Al (b)	Cu concentration / mmol Cu g^{-1}
Micro-Cu-Mordenite	8.9±0.7	0.15±0.02	9.7±0.1	0.17±0.01	0.252
Meso-Cu-Mordenite	20±2	0.27±0.03	16±1		0.214
Micro-Cu-SSZ-13	9.7±0.8	0.10±0.01	11±1	0.06±0.01	0.156
Micro-Cu-SSZ-13-2	9.7±0.8		10.2±0.3	0.31±0.01	0.446
Meso-Cu-SSZ-13	14±2	0.32±0.05			0.356
Micro-Cu-SSZ-39	6.3±0.4	0.22±0.04	6.6±0.1	0.20±0.03	0.502
Meso-Cu-SSZ-39	15±2	0.29±0.06			0.406
Cu-Omega	3.6±0.1	0.05±0.01			0.181

(a)Elemental analysis performed by EDX

(b)Elemental analysis performed by ICP-OES

3.1.3 SEM Images

In order to monitor the morphology and size of the crystals of the zeolites scanning electron microscopy was performed. Micro-Cu-Mordenite sample appeared agglomerated and consisted of an irregular shape and particle sizes vary from 150

nm to 1 μm (Figure 3.5-a). Meso-Cu-Mordenite sample also contained non-homogeneous shape and smaller crystals, which could form mesopores. Particle sizes varied from 1 nm to 200 nm. In addition, mesoporosity have seen on the crystal surfaces Figure 3.5-b).

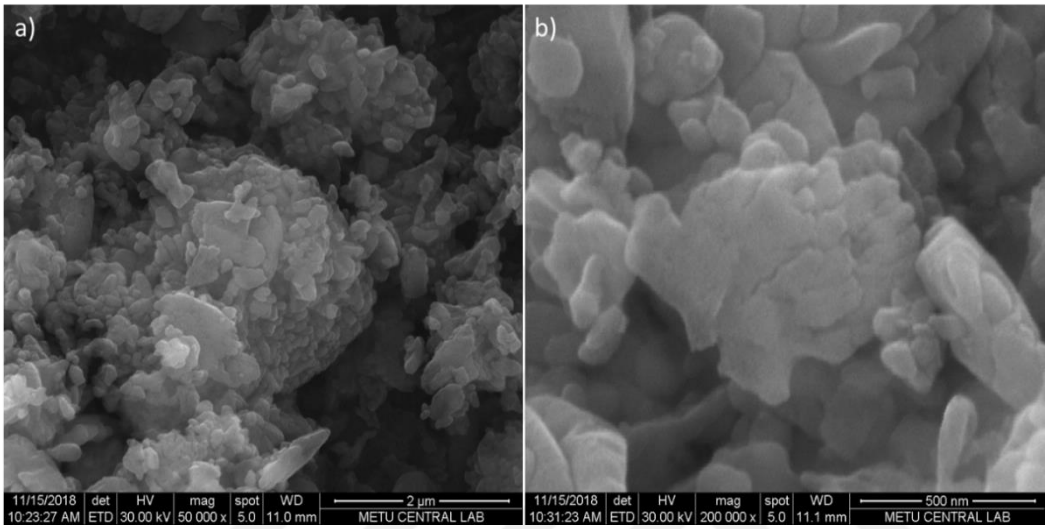

Figure 3.5 SEM images of a) Micro-Cu-Mordenite, b) Meso-Cu-Mordenite

Micro-SSZ-13 have a typical elliptic shape crystals with an average particle size of 1–2 μm (Figure 3.6-a). On the other hand, Meso-SSZ-13 sample has rhombohedral crystal morphology and particle sizes range from 250 nm to 4 μm which creates an intercrystalline mesopore volume (Figure 3.6-b). Mesopore addition procedure using CTABr have changed the morphology of SSZ-13.

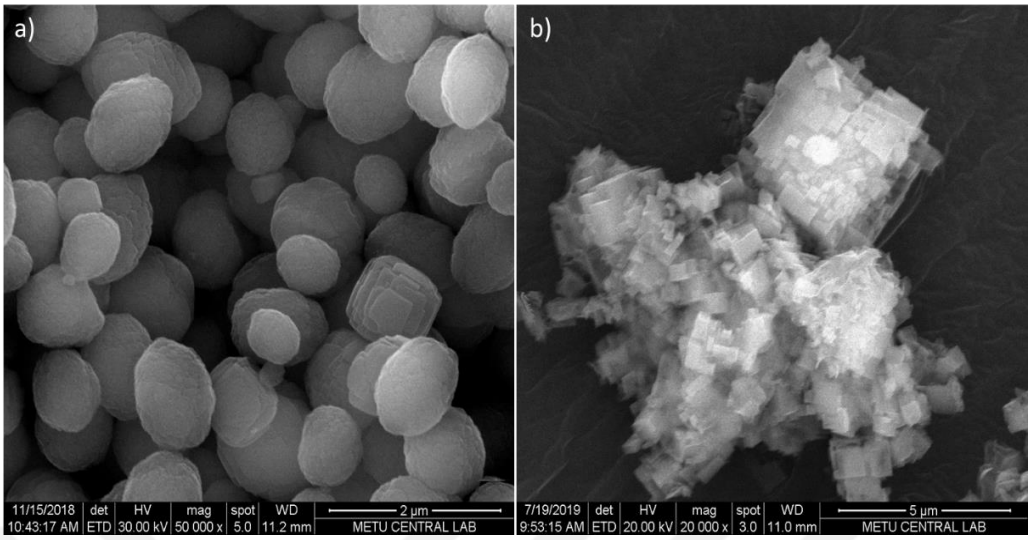

Figure 3.6. SEM images of a) Micro-Cu-SSZ-13, b) Meso-Cu-SSZ-13

Cu-SSZ-39 sample has 1.5–2 μm particle size with an orthorhombic crystal structure (Figure 3.7-a). Meso-SSZ-39 shows both typical orthorhombic morphology and layered crystal structure (Figure 3.7-b). Analcime zeolite morphology in 6–7 μm spherical particles were also observed (see Figure A.1).

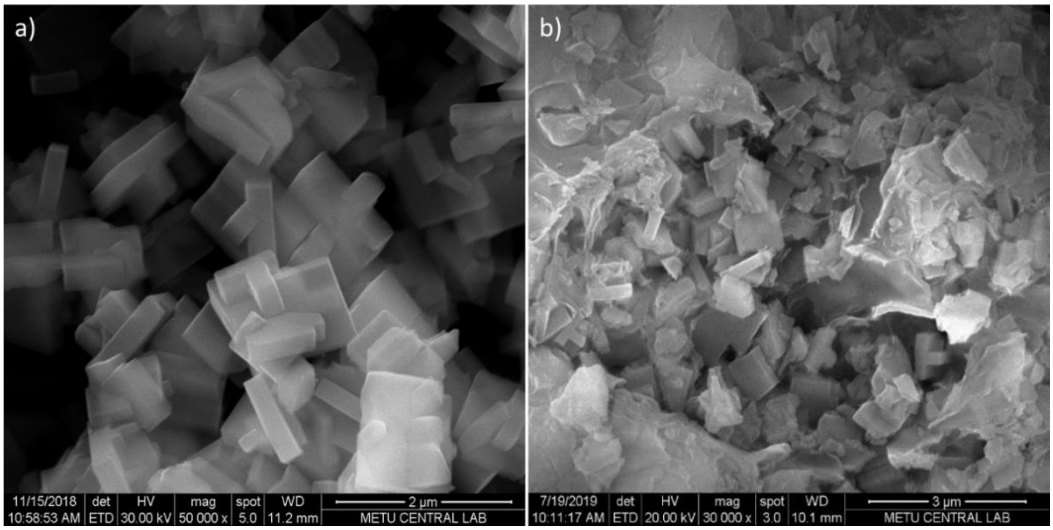

Figure 3.7. SEM images of a) Micro-Cu-SSZ-39, b) Meso-Cu-SSZ-39

Cu-Omega had globular shape and approximately 2 μm particle size crystals. The smaller particles that form bigger spherical structures are considered to cause mesoporosity (Figure 3.8).

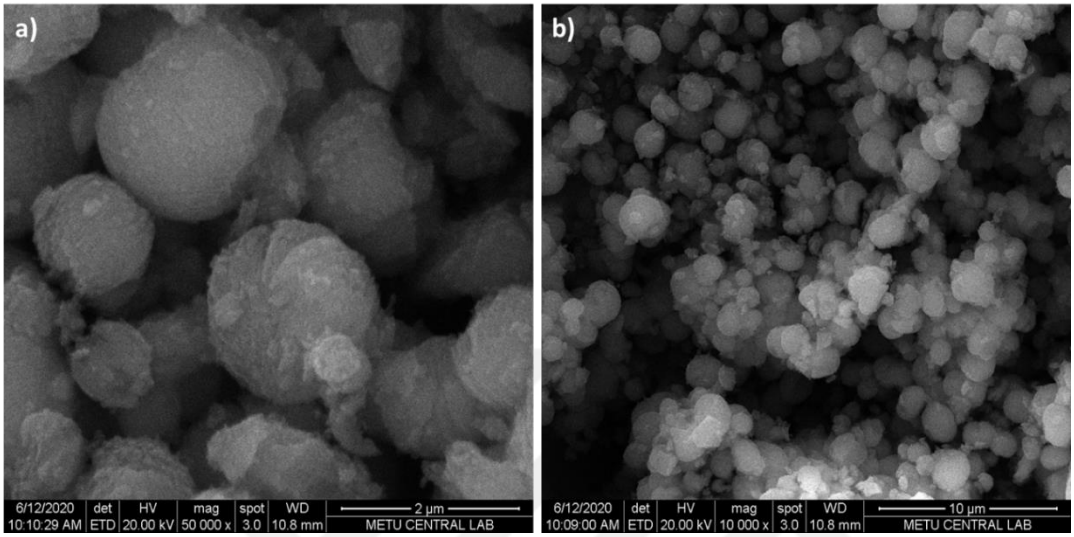

Figure 3.8. SEM images of Cu-Omega

3.1.4 N_2 Adsorption/Desorption Analysis

3.1.4.1 Pore Size Distributions

The mesopore size distributions were estimated by using the Barrett– Joyner–Halenda (BJH) method from the desorption branch of the isotherms given in Figure 3.9–Figure 3.12. The desired mesopore sizes were between 2–50 nm. According to BJH method, both mesopore and macropore (> 50 nm) formation was observed in Mordenite and SSZ-13 samples with a broad range as seen in Figure 3.9 and Figure 3.10. For Meso-Cu-SSZ-39 and Cu-Omega samples, mesopore size distributions have shown mesopores in the range of ~ 2–5 nm, and in the range of ~ 5–10 nm pore sizes, respectively. Results could be seen in Figure 3.11 and Figure 3.12.

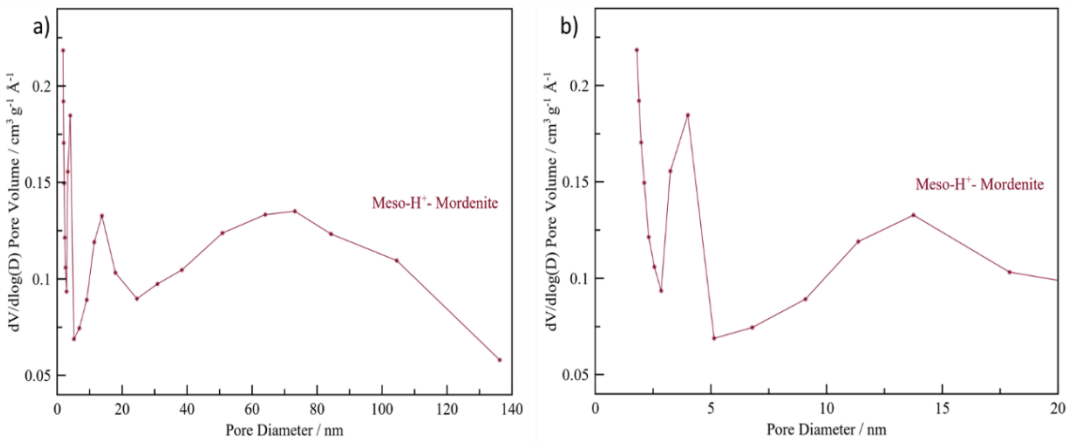

Figure 3.9. Pore size distribution of Meso- H^+-Mordenite sample calculated with BJH model

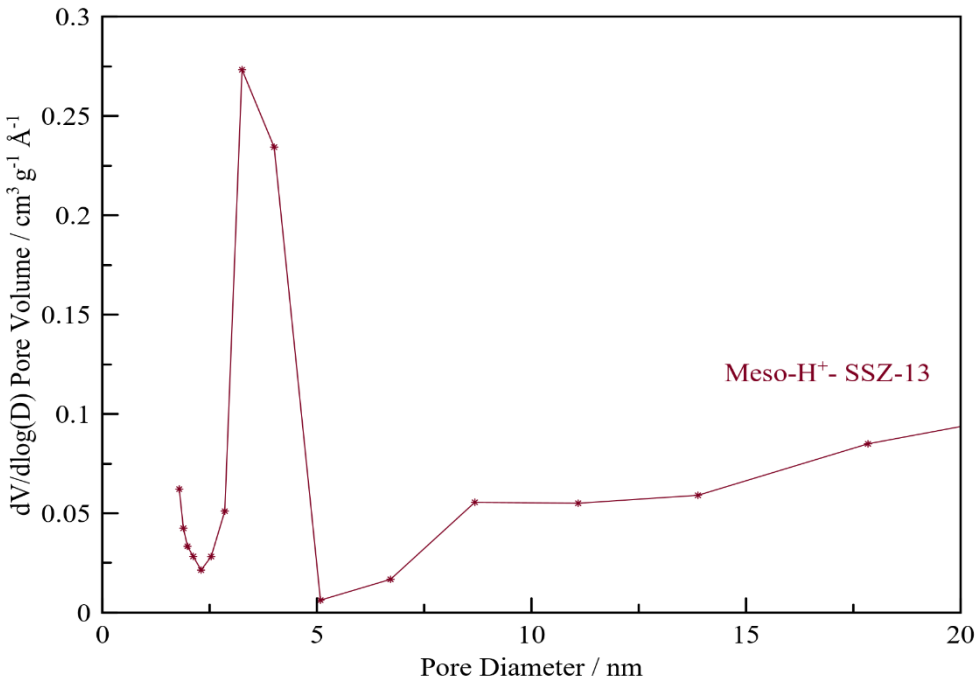

Figure 3.10. Pore size distribution of Meso- H^+-SSZ-13 sample calculated with BJH model

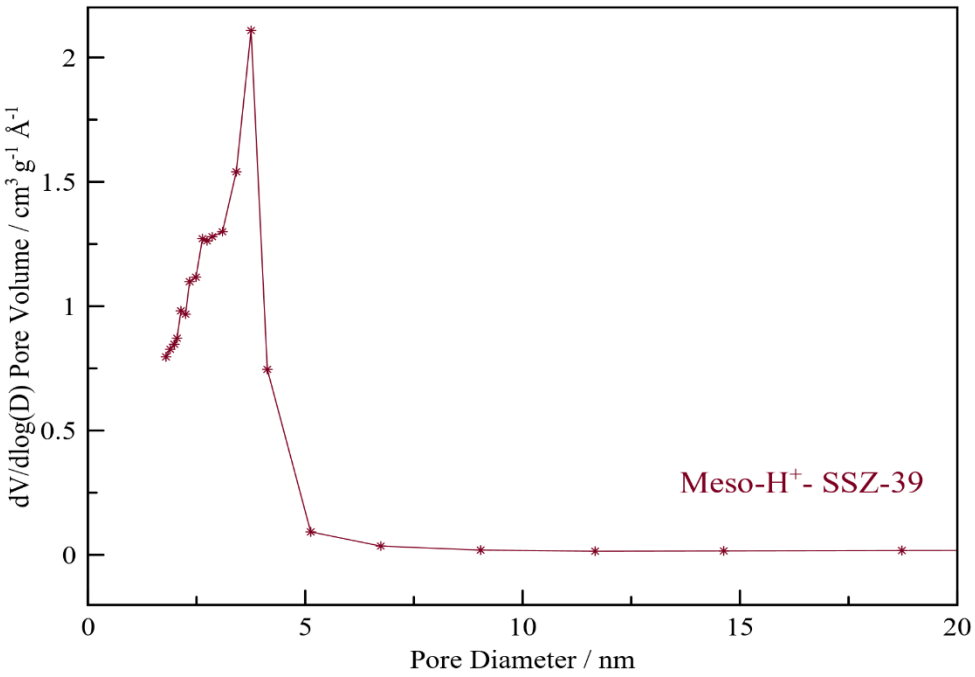

Figure 3.11. Pore size distribution of Meso- H^+-SSZ-39 sample calculated with BJH model

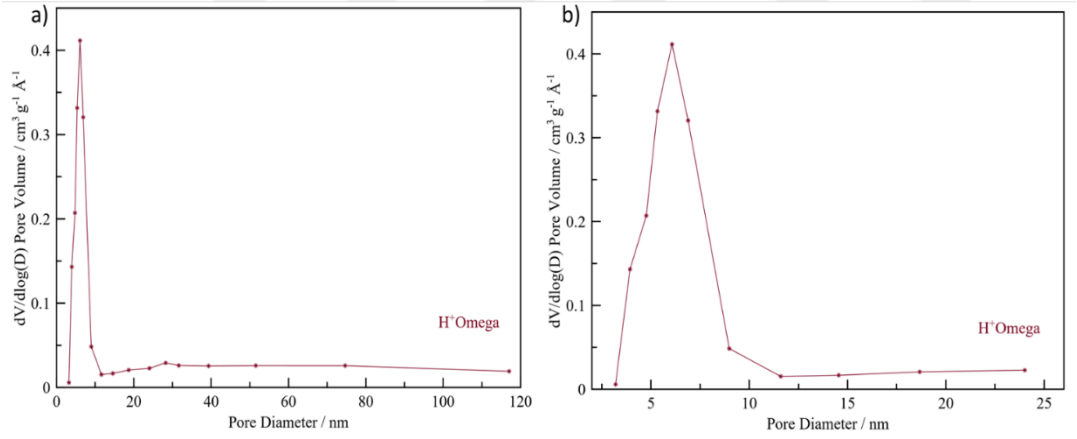

Figure 3.12. Pore size distribution of H^+- Omega sample calculated with BJH model

3.1.4.2 N_2 Adsoprtion Isotherm Analysis of H^+ Form Zeolites

N_2 isotherms of micro-and meso-H^+- form of Mordenite, SSZ-13, SSZ-39 and Omega were given in Figure 3.13Figure 3.16 (The tabulated data can be found in

Appendix A). The surface areas and pore volumes calculated from these isotherms are given in Table 3.3. For microporous samples, Type I adsorption isotherms without hysteresis loop were revealed, which were typical for microporous-zeolites. Volume filling was commenced with micropores at very low pressure for the Type I adsorption. For the mesoporous samples, adsorption and desorption curves followed different paths, showing hysteresis loops.

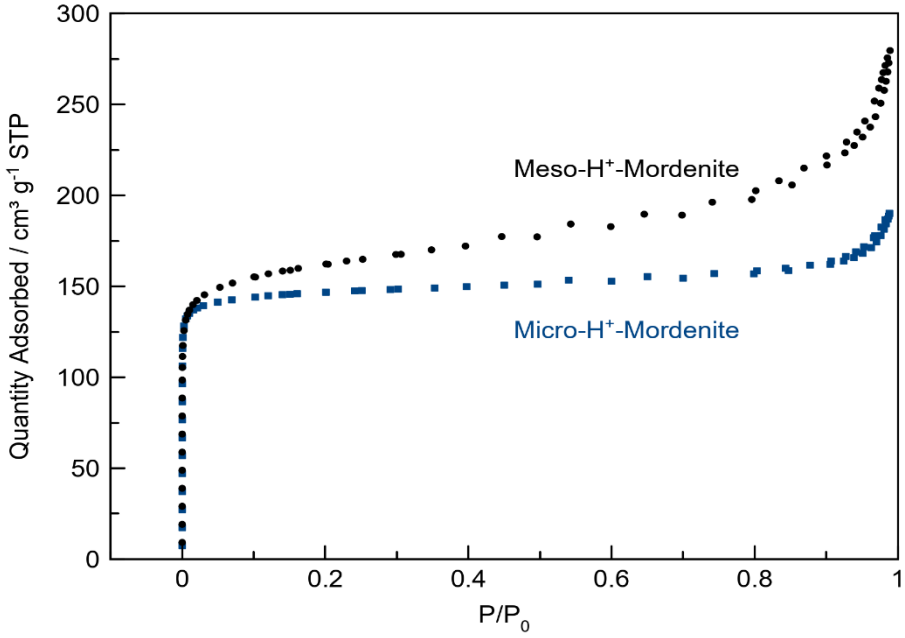

Figure 3.13. N_2 isotherms of micro- and mesoporous H^+ -Mordenite samples at 77 K

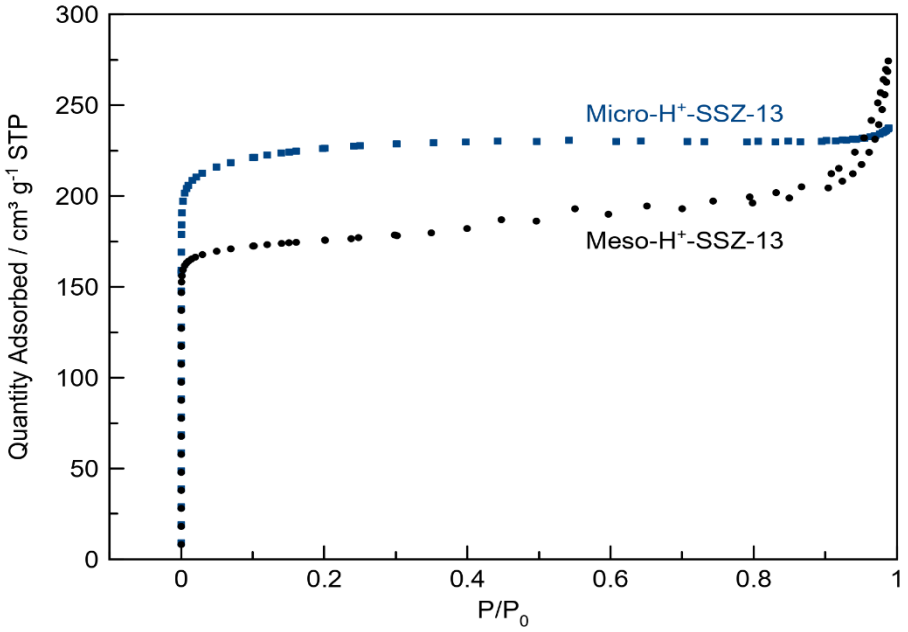

Figure 3.14. N_2 isotherms of micro- and mesoporous H^+-SSZ-13 samples at 77 K

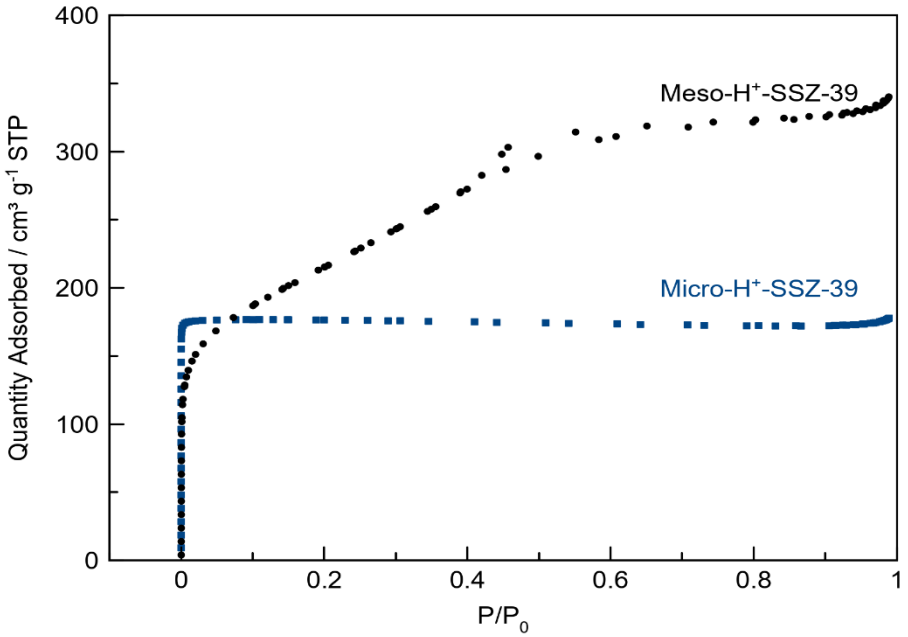

Figure 3.15. N_2 isotherms of micro- and mesoporous H^+ -SSZ-39 samples at 77 K

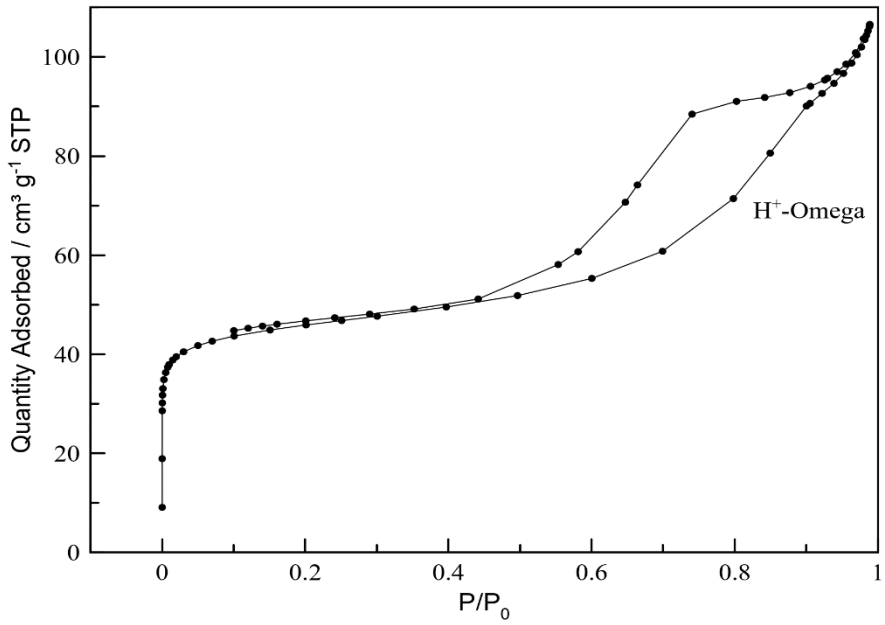

Figure 3.16. N_2 isotherm of and mesoporous H^+ -Omega sample at 77 K

3.1.4.3 N_2 Physisorption Characteristic Results of H^+ form Zeolites

The surface area, pore volume and pore size analyses of the synthesized micro- and mesoporous zeolites were performed using N_2 adsorption tests at 77 K. Table 3.3 shows the different characteristic of the samples. In Table 3.3, the total specific surface area (S_{BET}) was derived from the Brunauer–Emmett–Teller (BET) equation. Langmuir surface area ($S_{Langmuir}$) was calculated using Langmuir method, total volume (V_{total}) determined from the adsorbed amount at P/P_0=0.984. Micropore volume (V_{micro}) was calculated using t-plot (thickness method) and mesopore volume (V_{meso}) was figured out by subtracting micropore volume from the total pore volume [70].

Table 3.3. Surface area and pore volume values of micro and mesoporous H^+-zeolites

Zeolite	**$S_{Langmuir}$ / $m^2\ g^{-1}$**	**S_{BET}/ $m^2\ g^{-1}$**	**V_{total} / $cm^3\ g^{-1}$**	**V_{micro} / $cm^3\ g^{-1}$**	**V_{meso} / $cm^3\ g^{-1}$**
Micro- H^+-Mordenite	473	645	0.285	0.202	0.083
Meso- H^+-Mordenite	421	575	0.361	0.163	0.191
Micro- H^+-SSZ-13	730	995	0.364	0.306	0.058
Meso- H^+-SSZ-13	570	774	0.395	0.240	0.155
Micro- H^+-SSZ-39	559	766	0.276	0.278	-
Meso- H^+-SSZ-39	800	1099	0.557	0.056	0.501
H^+-Omega	206	151	0.16	0.05	0.11

Mesoporous samples were synthesized successfully reaching 0.501 $cm^3\ g^{-1}$ mesopore volumes compared to microporous samples. Mordenite sample, to which acid treatment was performed to obtain mesopore volume, showed increased mesopore volume from 0.083 $cm^3\ g^{-1}$ to 0.191 $cm^3\ g^{-1}$, which were expected values [62]. In SSZ-13 sample, decreased micropore volume from 0.306 $cm^3\ g^{-1}$ to 0.240 $cm^3\ g^{-1}$ was observed with increasing mesopore volume. Also development of mesoporosity accompanied by a decrease in BET and Langmuir surface areas (indicating decreasing microporosity) [71]. Although the microporous volumes

determined in Omega and Meso-SSZ-39 are slightly lower than the expected values [72,73], microporous SSZ-39 structures are clearly present in the X-ray diffraction patterns. In addition, drop in the micropore volume from 0.278 cm^3 g^{-1} to 0.056 cm^3 g^{-1} in the Meso-H^+-SSZ-39 could be explained by the presence of analcime having non-accessible pores. However, 0.501 cm^3 g^{-1} mesopore volume indicates significant mesoporosity.

3.1.4.4 N_2 Adsorption Isotherm Analysis of Cu(II) Exchanged Zeolites

The surface areas, pore volumes and pore size analysis of the synthesized micro- and mesoporous zeolites after the Cu(II)-exchange were also conducted using N_2 adsorption tests at 77 K.

Micropore and mesopore volumes of the zeolites are given in Figure 3.17–Figure 3.19 and Table 3.4. The slight decrease in the microporous volumes of zeolites after the Cu change shows that the Cu(II) cations were located in the micropores.

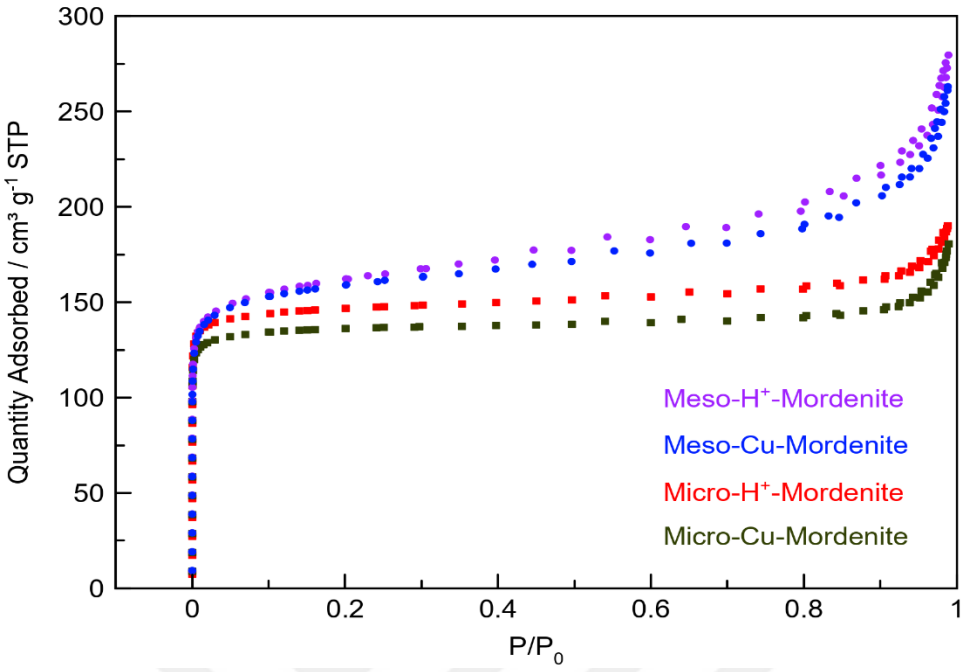

Figure 3.17. N_2 isotherms of micro- and mesoporous H^+ and Cu-Mordenite samples at 77 K

In Figure 3.17, Micro-Cu-Mordenite samples have shown a reversible Type-I adsorption/desorption isotherm which demonstrates an adsorption on microporous solid. Meso-H^+-Mordenite and Meso-Cu-Mordenite sample showed typical Type IV isotherms corresponding to zeolites with mesopores.

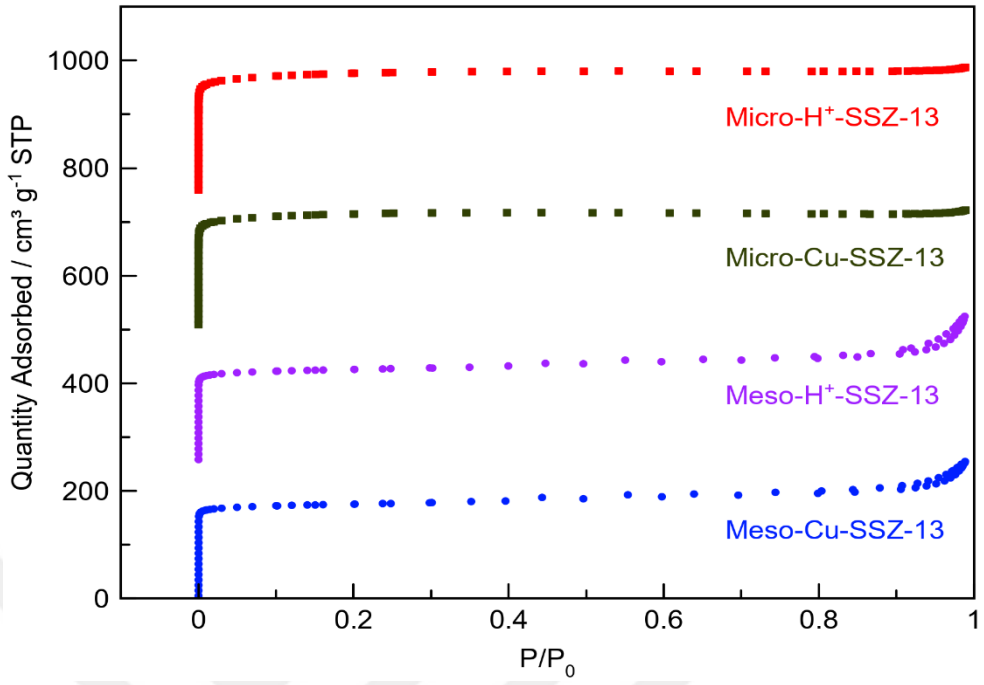

Figure 3.18. N_2 isotherms of micro- and mesoporous H^+ and Cu-SSZ-13 samples at 77 K

According to Figure 3.18, Micro-H^+-SSZ-13 and Micro-Cu-SSZ-13 have showed Type I adsorption isotherm, having only micropores. Meso-H^+SSZ-13 and Meso-Cu-SSZ-13 mesoporous samples showed a Type IV adsorption isotherm with H4 type hysteresis loop revealed mesopore structure and narrow slit-shaped pores [74].

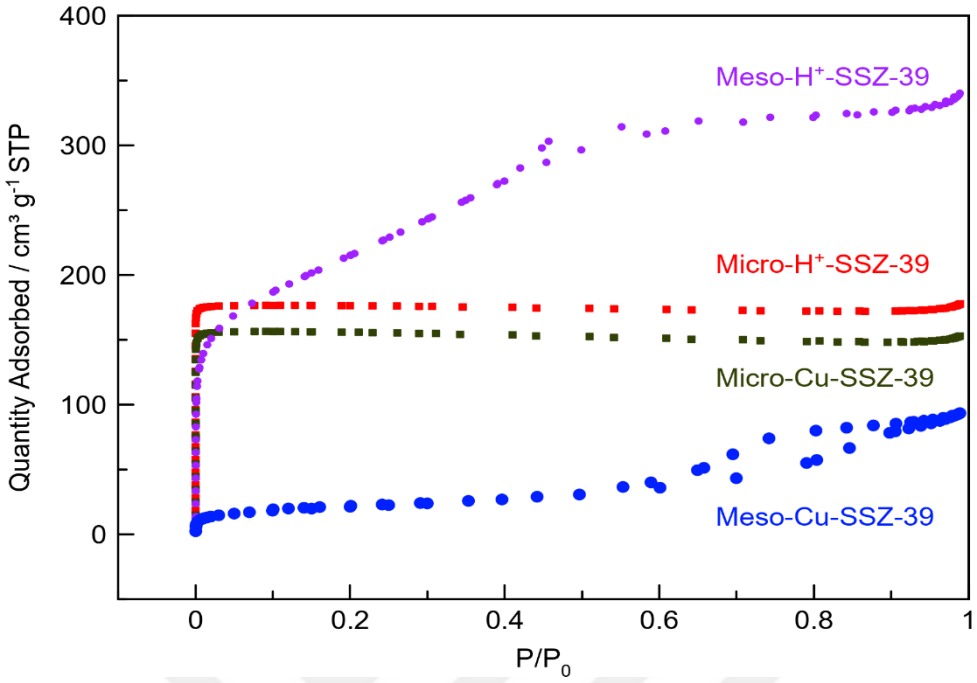

Figure 3.19. N_2 isotherms of micro- and mesoporous H^+ and Cu-SSZ-13 samples at 77 K

According to Figure 3.19, Micro-Cu-SSZ-39 sample showed typical Type I adsorption isotherm. In addition, Meso-H^+-SSZ-39 and Meso-Cu-SSZ-39 revealed Type IV adsorption isotherm with H2 hysteresis loop found with aggregated crystals of zeolites having clogged pores. On the other hand, Meso-Cu-SSZ-39 sample have shown lower micropore volume meaning that Cu(II)-exchange affected the N_2 adsorption capacity.

3.1.4.5 N_2 Physisorption Characteristic Results of Cu(II) Exchanged Zeolites

The surface area, pore volume and pore size analysis of the Cu(II)-exchanged microporous and mesoporous zeolites were performed using N_2 adsorption tests at 77 K shown in Table 3.4. After Cu(II) exchange, microporous zeolites have shown lower specific surface area and micropore volume. For the Meso-SSZ-39 sample, micropore volume was decreased after Cu(II) exchange.

Table 3.4. Surface area and pore volume values of micro and mesoporous H^+ and Cu(II)-exchanged -zeolites

Zeolite	**$S_{Langmuir}$ / $m^2\ g^{-1}$**	**S_{BET} / $m^2\ g^{-1}$**	**Vtotal / $cm^3\ g^{-1}$**	**Vmicro / $cm^3\ g^{-1}$**	**Vmeso / $cm^3\ g^{-1}$**
Micro- H^+ Mordenite	473	645	0.285	0.202	0.083
Micro-Cu-Mordenite	440	597	0.264	0.193	0.071
Meso- H^+-Mordenite	421	575	0.361	0.163	0.191
Meso-Cu-Mordenite	519	709	0.386	0.189	0.197
Micro- H^+-SSZ-13	730	995	0.364	0.306	0.058
Micro-Cu-SSZ-13	692	943	0.340	0.294	0.046
Meso- H^+-SSZ-13	570	774	0.395	0.240	0.155
Meso-Cu-SSZ-13	568	771	0.374	0.241	0.133
Micro- H^+-SSZ-39	559	766	0.276	0.278	-
Micro-Cu-SSZ-39	490	676	0.247	0.247	-
Meso- H^+-SSZ-39	800	1099	0.557	0.056	0.501
Meso-Cu-SSZ-39	74	102	0.142	0.004	0.138
Cu-Omega	194	265	0.202	0.057	0.145

3.1.5 Raman Spectra following N_2O Activation

For Cu-exchanged zeolites, different dicopper and tricopper species are assigned to be active sites for the step-wise methane activation [20,42]. To investigate the active sites for the Micro-Cu-SSZ-13, Micro-Cu-SSZ-39 and Micro-Cu-Mordenite, which showed promising methanol production activity, Raman experiments are performed. Resonance conditions toward these components can be achieved by proper excitation, which is determined as 532 nm. Results of the Raman spectroscopy are given in Figure 3.20 – Figure 3.24

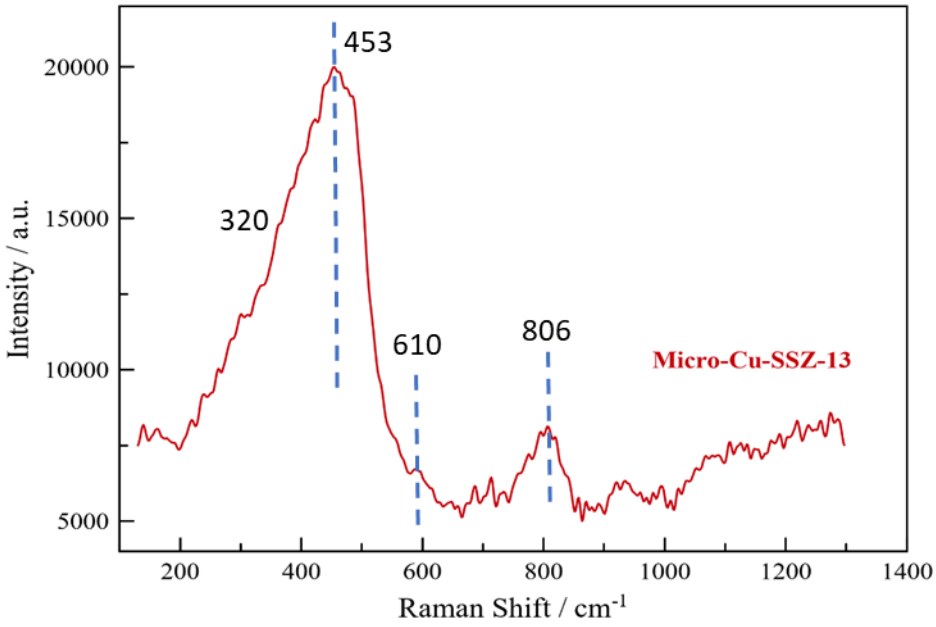

Figure 3.20. Raman spectra of Micro-Cu-SSZ-13 following treatment with 15.2 kPa N_2O at 573 K (λ_{ex} = 532 nm)

The bands at 453 cm^{-1} was assigned to T-O-T bending vibrations in the 4MR of the zeolite. 320 cm^{-1} was assigned to the bending vibration of the 6MR components [75]. The vibration at 806 cm^{-1} was assigned to the symmetrical stretching vibration of T-O bonds [76].

A band at 610 cm^{-1} was assigned as bis(μ-oxo) dicopper(III) complex by Guo et al., whose presence is widely debated on CHA due to the absence of evidence of any Cu(III) species using X-ray absorption spectroscopy [66]. Ipek et al. assigned a Raman vibration at 617 cm^{-1} to a mono-(μ-oxo) dicopper(II) complex with an expected Cu−O−Cu angle of 95° [20] Our results have shown that in SSZ-13 showed presence of vibrations indicative of mono-(μ-oxo) dicopper(II) complex following N_2O treatment (see Figure 3.20).

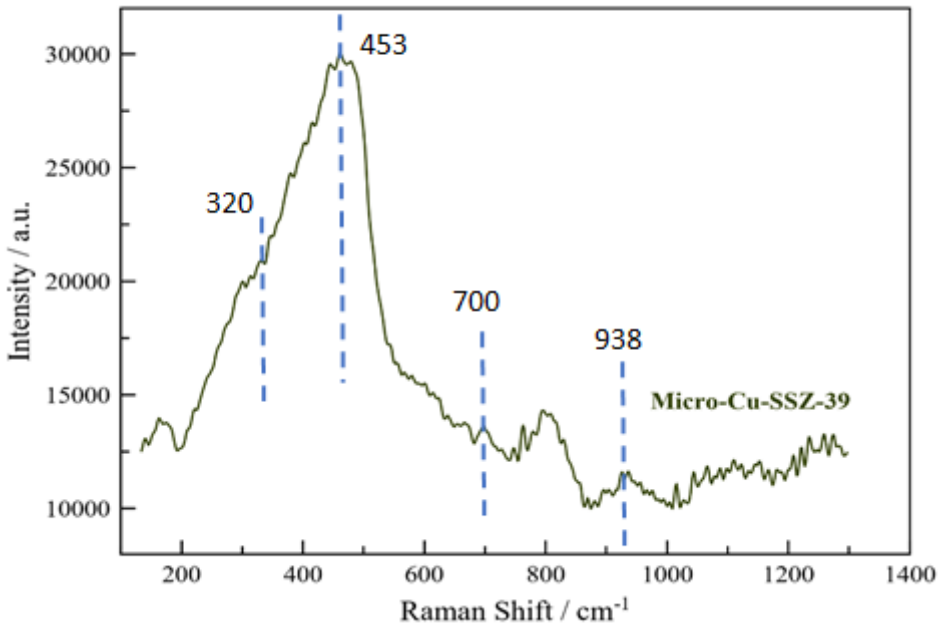

Figure 3.21. Raman spectra of Micro-Cu-SSZ-39 following treatment with 15.2 kPa N_2O at 573 K (λ_{ex} = 532 nm)

In Figure 3.21, Raman spectra of activated Micro-Cu-SSZ-39 strongly resembles the Micro-Cu-SSZ-13. Micro-Cu-SSZ-39 has specific Raman vibration at 453 cm^{-1} which designated to 4MR and also at ~320 cm^{-1} which assigned as 6MR vibrations. The band at ~700 cm^{-1} could indicate that SSZ-39 could have a different active species. Additionally, bands at 938 cm^{-1} and 1000–1200 cm^{-1} showed a new band related to several oxygen activated Cu(II) species which could be assigned to $[Cu^{II}O_2^{\bullet}]^+$ superoxo species.

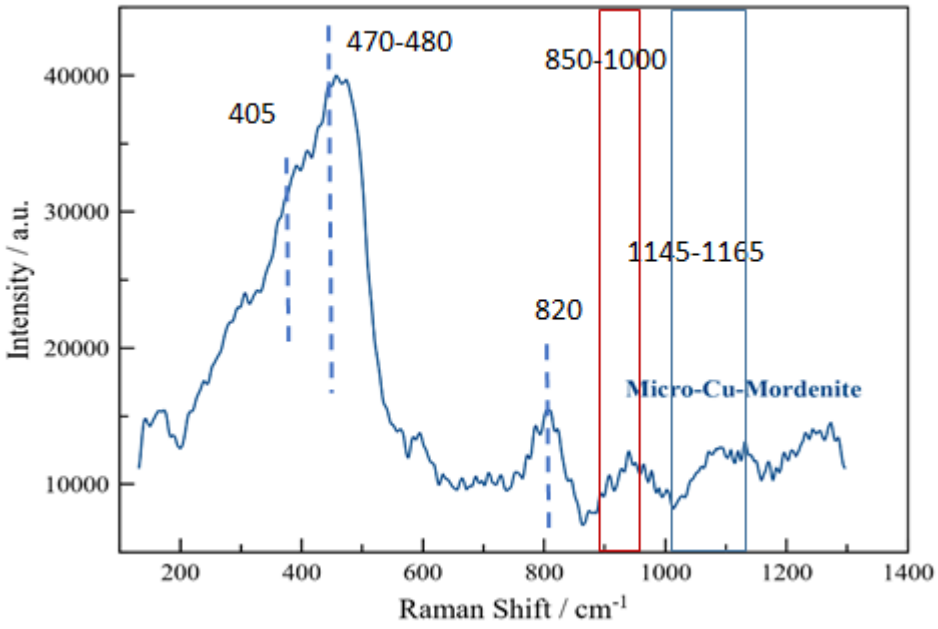

Figure 3.22. Raman spectra of Micro-Cu-Mordenite following treatment with 15.2 kPa N_2O at 573 K (λ_{ex} = 532 nm)

According to Figure 3.22, , the wide band at 400–500 cm^{-1} represents the bending vibrations of the 5MRs and 4MRs at 405 cm^{-1} and 470–480 cm^{-1} respectively. The vibrations at 820 cm^{-1} and 1145-1165 cm^{-1} are assigned to the symmetric and asymmetric stretching motions of T–O bonds respectively [76]. A plausible mono-(μ-oxo) dicopper(II) complex ($[Cu_2O]^{2+}$) forming following the N_2O activation of mordenite was expected to show a symmetric stretching mode of the bridging oxo ligand at 455 cm^{-1} and a weak antisymmetric stretch at ~870 cm^{-1} as characteristics vibrations [77]. On the other hand, Mordenite features were broad and asymmetric, suggesting more than one species is present especially with the vibrations at 850–1000 cm^{-1}.

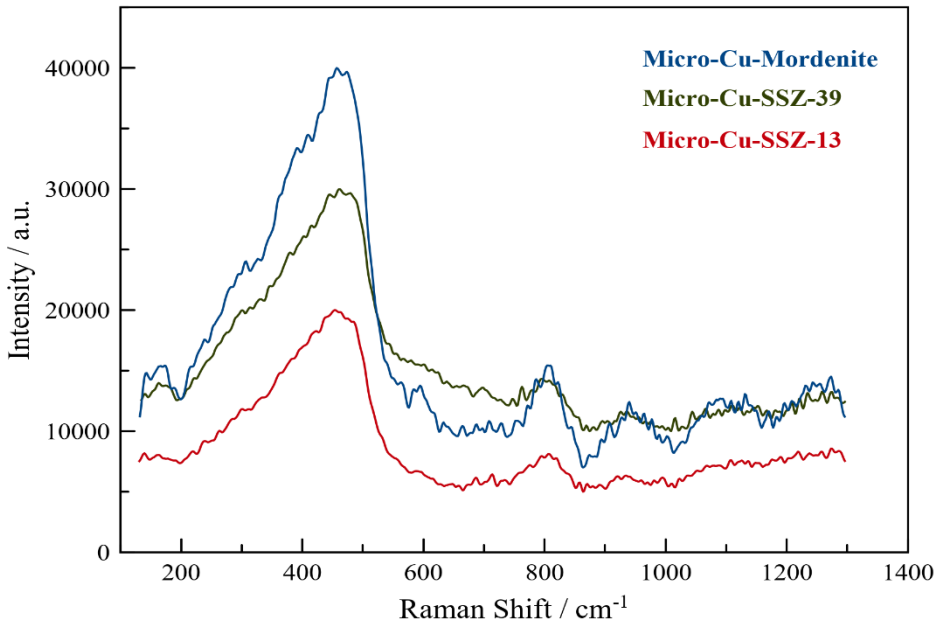

Figure 3.23. Raman spectra of Cu-zeolites following treatment with 15.2 kPa N_2O at 573 K

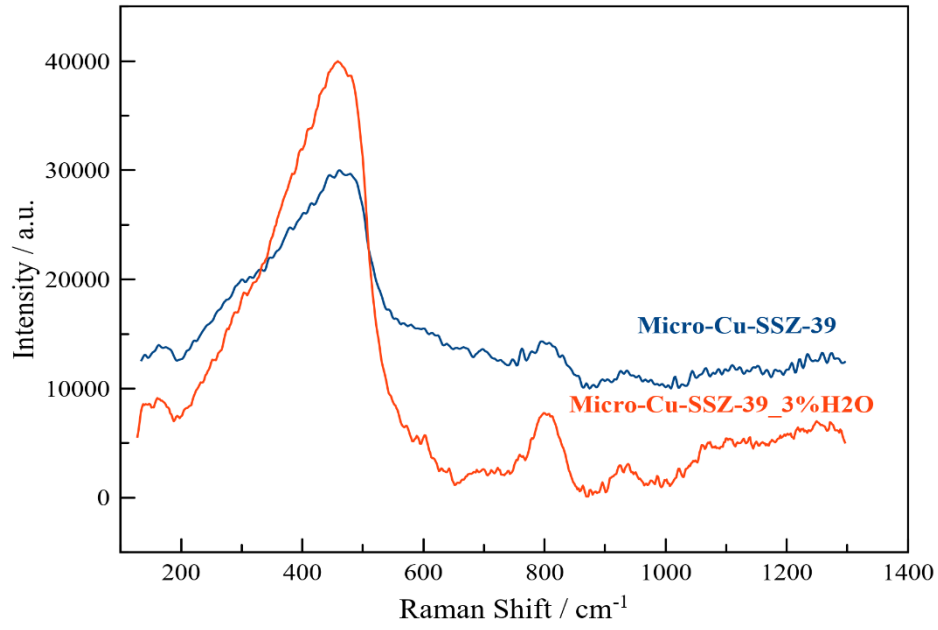

Figure 3.24. Raman spectra of Cu-SSZ-39 following treatment with 15.2 kPa N_2O and 3.2 kPa H_2O at 573 K

Figure 3.24 shows the different activation conditions for Micro-Cu-SSZ-39. The blue line has referred to N_2O treatment without water and orange line has indicated as activation conditions of 15 mole% N_2O and 3% H_2O. The band at ~700 cm^{-1} was observed to be more significant in the N_2O treated sample without the water vapour, indicating the vibration belonging to an active species that has to be further investigated.

3.2 Methane to Methanol Reaction Results

Catalytic experiments were carried out in the temperature range of 573 and 598 K in order to avoid the decomposition of methane into CO_2 and CO at higher temperatures. Reaction conditions were chosen to obtain reasonable rates and methanol selectivity values comparable to the results presented in the literature.

In the first part, micro- and meso-porous zeolites containing copper were tested at a temperature of 573 K with a composition of 40 mole% CH_4, 10% N_2O, 3% H_2O with the balance He. The total flow rate of the gas mixture was set to 100 sccm. In the second part, in order to optimize N_2O partial pressure and analyse the rate order, Micro-Cu-SSZ-39 and Micro-Cu-Mordenite were tested at a temperature of 573 K with a two different feed gas composition. (40 mole% CH_4, 5% N_2O, 3% H_2O, balance He and CH_4 40 mole% CH_4, 15% N_2O, 3% H_2O and balance He). The total flow rate was kept at 100 sccm. In the third part, for optimization of CH_4 partial pressure and investigating the rate order, Micro-Cu-SSZ-39 and Micro-Cu-Mordenite were tested at 573 K. Feed gas compositions consist of 20 mole% CH_4, 10% N_2O, 3% H_2O and 30 mole% CH_4, 10% N_2O, 3% H_2O respectively. In the fourth part, for understanding the water effect on reaction, reaction compositions of 40 mole% CH_4, 10% N_2O, 10% H_2O for Micro-Cu-Mordenite at 573 K and 598 K and 40 mole% CH_4, 15% N_2O, 10% H_2O were tested for Micro-Cu-SSZ-39 at 598 K. In the fifth part, comparison between the total flow rates of 50 sccm and 100 sccm was investigated. Finally, activation energy calculation was performed in the last part. In all experiments, zeolites containing Cu(II) showed a steady-state methanol

production for the testing time of least 2 hours and did not show signs of deactivation during this period.

3.2.1 Qualitative Analysis of Reaction Products at 573 K

The reaction products were automatically sampled and analyzed by the gas chromatograph equipped with a Pora Plot-Q and a Molsieve 5Å column; TCD and FID in each 21 minute intervals. Hydrocarbons having low concentrations in reaction such as CH_3OH and DME were analyzed by FID column which has high sensitivity while, N_2O, N_2, O_2, and H_2O were analyzed in TCD column. Different GC method was created in order to analyze CO and CO_2 concentrations in TCD column. Methanol selectivity was calculated as rate of production of methanol divided by rate of methane consumption, which is considered as the summation of all carbon weighted products' formation rates at the outlet given in Eq 3.1 (The sample calculations can be seen in Appendix B).

$$S_{CH3OH}=\frac{r_{CH3OH}}{r_{CH3OH}+2*r_{DME}+r_{CO}+r_{CO2}}*100 \quad \text{Eq 3.1}$$

$$r_{CH4}(\mu mol\ g^{-1}h^{-1}) = r_{CH3OH} + 2 * r_{DME} + r_{CO} + r_{CO2} \quad \text{Eq 3.2}$$

$$X_{CH4}(\%) = \frac{r_{CH4}}{F_{CH4}/g_{cat}} \quad \text{Eq 3.3}$$

$$X_{N2O}(\%) = \frac{r_{N2}}{F_{N2O}/g_{cat}} * 100 \quad \text{Eq 3.4}$$

$$TOF_{CH4}(\frac{mol\ CH_4}{mol\ Cu\ h}) = \frac{r_{CH4}}{Cu\ concentration} \quad \text{Eq 3.5}$$

Once steady-state CH_3OH production was achieved at 573 K, kinetic experiments were conducted. All reported values for selectivity, rates of product formation were averaged over at least four data points upon reaching steady-state.

For investigating the zeolite framework effect, reaction was carried out at 573 K with a composition of 40 mole% CH_4, 10% N_2O, 3% H_2O with the balance He. Methanol production rate with respect to time results are given in Figure 3.25. At the outlet stream, CH_3OH as the main product, DME, CO_2 and CO were observed as side-products. Side product production rate, methane conversion, N_2O conversion, selectivity and TOF values were given in Table 3.5.

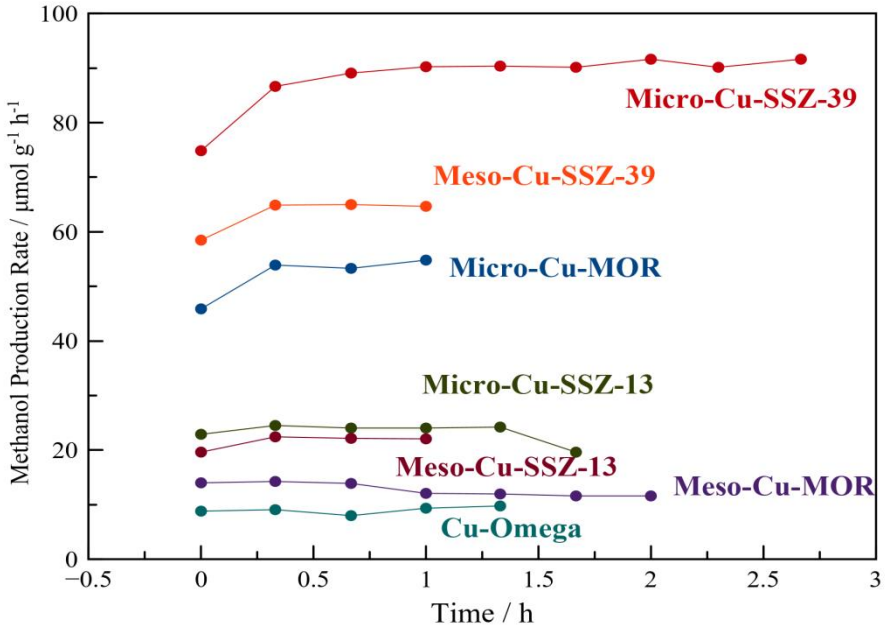

Figure 3.25. Methanol production rates at 573 K (gas composition of 40.5 kPa CH_4, 10.13 kPa N_2O, 3.2 kPa H_2O, total flow 100 sccm, ~0.3 g catalyst, time= 0 h is selected as the time the reactor reached the reaction temperature)

In Figure 3.25, the steady state was achieved at 573 K and kinetic experiments were conducted. Reaction time was approximately 2 hours. Methanol, DME, carbon dioxide and carbon monoxide were seen as products of the catalytic reaction with methanol selectivity values between 22% and 70%. The best methanol production rate achieved with the Micro-Cu-SSZ-39 sample, 90.6 µmol g^{-1} h^{-1}. Production rates of methanol and side products, also methanol selectivity values are given in Table 3.5.

Table 3.5. Methanol, DME, CO and CO_2 production rates and selectivity of methanol at 573 K with the feed composition of CH_4 40 mole %, 10%, N_2O, 3% H_2O and balance He (approximately 300 mg catalyst)

Zeolite	r_{CH3OH} / µmol g^{-1} h^{-1}	r_{DME} / µmol g^{-1} h^{-1}	r_{CO2} / µmol g^{-1} h^{-1}	r_{CO} / µmol g^{-1} h^{-1}	r_{CH4} / µmol g^{-1} h^{-1}	CH_4 Conversion / %	N_2O conversion / %	TOF CH_4 / h^{-1}	TOF CH_3OH / h^{-1}	S_{CH3OH} / %
Micro-Cu-Mordenite	54.7±0.7	2.24±0.03	10.9±0.7	31.9	101.9	0.027	0.173	0.40	0.22	54
Meso-Cu-Mordenite	13±1	0.18±0.02	22±3	2.2±1.5	37.3	0.008	0.082	0.17	0.06	34
Micro-Cu-SSZ-13	24.2±0.2	0.45±0.02	7.6±1	8±3	40.7	0.011	0.088	0.26	0.16	59
Micro-Cu-SSZ-13-2*	19.7±0.1	0.31±0.02	37±2	31±10	88.3	0.025	0.161	0.20	0.04	22
Meso-Cu-SSZ-13	22.2±0.2	0	32.6±2.4	7±5	61.5	0.017	0.156	0.17	0.06	36
Micro-Cu-SSZ-39	90.6±0.7	5.4±0.1	14.9±0.5	90.2±8.8	206.5	0.050	0.225	0.41	0.18	44
Meso-Cu-SSZ-39	65.2±0.4	2.3±0.1	3.6±0.7	20±4	93.4	0.025	0.159	0.23	0.16	70
Cu-Omega	9.0±0.7	0	5.9±0.8	0	14.9	0.003	0.055	0.08	0.05	60

*Micro-Cu-SSZ-13-2 was the same sample with Cu/Al=0.32, whereas Micro-Cu-SSZ-13 has Cu/Al=0.10

In Table 3.5, Micro-Cu-SSZ-39 showed 90.6 μmol g^{-1} h^{-1} and Micro-Cu-Mordenite showed 54.7 μmol g^{-1} h^{-1} methanol production rate with selectivities of 44% and 54%. These high methanol formation rates (when compared to literature) shows potential for Micro-SSZ-39 sample as a new catalyst for MTM reaction [20]. Micro-Cu-Mordenite and Meso-Cu-Mordenite have showed very high production rates when compared to literature. Narsimhan et al have found 0.84 μmol g^{-1} h^{-1} rate with a ~70% selectivity for microporous Mordenite at 483 K using the reaction conditions of 98 mole % CH_4, 3% H_2O and 0.002% O_2 [78]. This low methanol production rate with a high selectivity could be because of insufficient activation of active sites at 483 K. In addition, for Micro-Cu-SSZ-13, 24.2 μmol g^{-1} h^{-1} production rate have been achieved here, which is comparable with the Ipek et al. study, 28 μmol g^{-1} h^{-1} [20]. The reason of slight differences could be because of Cu/Al ratio, which effects the active site and the number of active site formed. In this study, Micro-Cu-SSZ-13 have Cu/Al=0.10 and Ipek et al. had Cu/Al=0.40. In addition, reaction conditions were also slightly different; i.e., N_2O partial pressure of 10.13 kPa used here and 30.4 kPa is used in Ipek et al., respectively.

Mesoporosity affected all zeolites differently. For mordenite and SSZ-13, selectivity and production rate were lower when mesoporosity was introduced. However for Meso-Cu-SSZ-39 a higher methanol selectivity (70%) was observed when compared to Micro-Cu-SSZ-39 (44%) with slightly slower methanol production rate; 65.2 μmol g^{-1} h^{-1}. Higher selectivity on Meso-Cu-SSZ-39 when compared to Micro-Cu-SSZ-39 could be due to the smaller crystal sizes observed for Meso-Cu-SSZ-39, which resulted in shortened diffusion pathways preventing secondary oxidation reaction to CO and CO_2. Mesoporous omega displayed methanol selectivity of 60% with 9 μmol g^{-1} h^{-1} methanol production rate, which is quite lower than other zeolite frameworks. In 3-step proses results, activation of Omega at 723 K and reaction at 473 K resulted in producing 197.2 μmol CH_3OH g^{-1} [79]. Comparison of the methanol production of Omega with the literature was not possible for catalytic application because the catalytic reaction on Cu-Omega was not performed before [79]. However, Cu/Al ratio of 0.05 observed here could result in Cu(II) sites away

from each other, which would decrease the chance of forming dicopper-oxo species as plausible active sites.

Lower TOF values of Meso-Cu-Mordenite (Cu/Al = 0.27), Meso-Cu-SSZ-13 (Cu/Al = 0.32) and Cu-Omega (Cu/Al = 0.05) indicated that Cu concentrations in these zeolites were not optimal for active species formation.

Micro-SSZ-13 samples with Cu/Al ratio of 0.10 and 0.32 (Micro-Cu-SSZ-13 and Micro-Cu-SSZ-13-2 respectively) have showed different methanol production rates 24.2 μmol g^{-1} h^{-1} and 19.7 μmol g^{-1} h^{-1}, respectively. When the turn over frequency values are concerned, a higher activity on Micro-Cu-SSZ-13 with Cu/Al 0.10 is observed (0.16 h^{-1} vs. 0.04 h^{-1}). For selectivity, lower Cu-content resulted in higher selectivity values. This result underscores the importance of Cu/Al ratio. Dinh et al. showed that, higher Cu-loadings direct the formation of Cu_xO_y active sites that are not selective towards methane partial oxidation to methanol indicating optimum Cu/Al ratios of <0.3 [52]. In addition, smaller concentration of Cu-sites (Cu/Al < 0.3) would favour methanol selectivity by inhibiting the interaction of freshly produced methanol with other active sites in the way out of the crystal, thus preventing secondary reactions.

3.2.2 Effect of N_2O, Methane and Water Partial Pressures

3.2.2.1 Effect of N_2O Partial Pressure

To investigate the effect of oxidant on methanol formation rate and oxidant partial pressure optimization, reactions were performed on Micro-Cu-SSZ-39 and Micro-Cu-Mordenite with different partial pressures of N_2O. Reactions were carried out with a composition of 40 mole % CH_4, 3% H_2O, 5% to 15 % N_2O, and balance He. First, reactions were carried out at a partial pressure of 5.1 kPa N_2O and then the N_2O partial pressure was increased to 15.2 kPa. Respective methanol production results can be seen in Figure 3.26. According to Figure 3.26, increasing N_2O partial

pressure resulted in increased amount of methanol production. For production rate, 15% oxidant was superior for both zeolites. Some reaction kinetic results were given in Table 3.6.

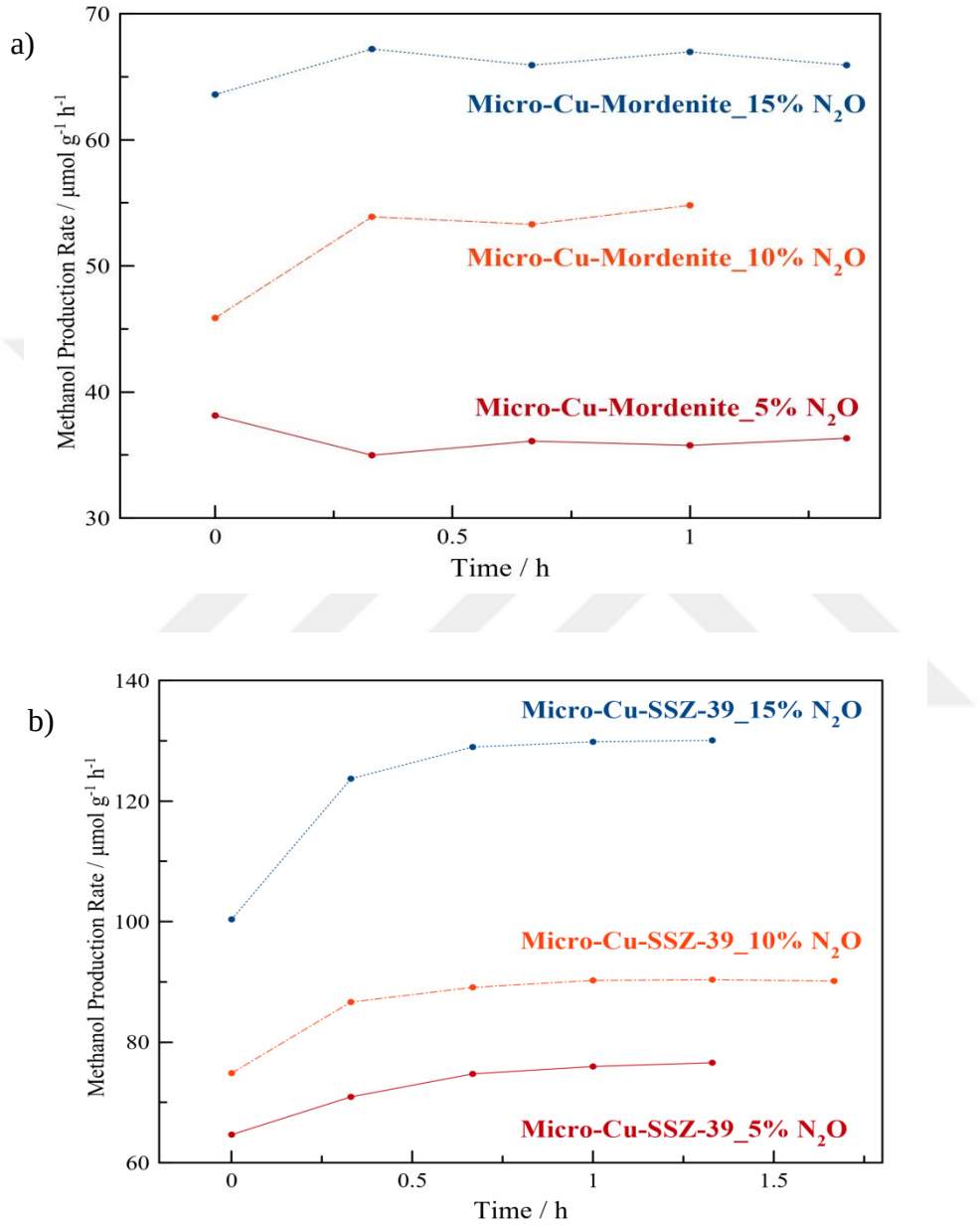

Figure 3.26. Methanol production rates at 573 K (gas composition of 40.5 kPa CH_4, 3.2 kPa H_2O and 5.06 kPa, 10.13 kPa or 15.2 kPa N_2O, total flow 100 sccm, ~0.3 g catalyst) a) SSZ-39 b) Mordenite

Methanol selectivity and methanol production rate could be seen in Table 3.6 with different N_2O partial pressures at 573 K. Methanol production rate of 130 μmol g^{-1} h^{-1} and 66 μmol g^{-1} h^{-1} were achieved for Micro-Cu-SSZ-39 and Micro-Cu-Mordenite with a feed gas composition of 40 mole% CH_4, 15% N_2O, 3% H_2O and balance He at 573 K. Selectivity of methanol was comparable on Micro-Cu-Mordenite and Micro-Cu-SSZ-39 (52%). Inverse relation between the selectivity and methanol production rate was observed for Micro-Cu-Mordenite, which is expected for alkane oxidation reactions with higher secondary oxidation rates [27]. However, for Micro-Cu-SSZ-39, increasing methanol selectivity with increasing methanol production rate was observed up to 15% N_2O composition (see Table 3.6).

For Micro-Cu-Mordenite, increased N_2O partial pressure from 5.1 kPa to 15.2 kPa had a tendency of increasing methanol production rate but decreasing selectivity values from 64% to 52%. Partial pressure of 10.1 kPa for N_2O resulted in a methanol production rate of 54.7 μmol g^{-1} h^{-1} and methanol selectivity of 54% on Micro-Cu-Mordenite. Because the selectivity values were more logical and optimal, this partial pressure was chosen as an optimum N_2O partial pressure for Micro-Cu-Mordenite. But superior methanol production rate and selectivity with the 15% N_2O was achieved for Micro-Cu-SSZ-39 with values of 130 μmol g^{-1} h^{-1} and 52%, respectively, which are unprecedented in literature for catalytic methanol production [20,52,78]

Methane conversion was high on Micro-Cu-SSZ-39 and increased amount of oxidant resulted not only in increased methane conversion but also increased TOF (h^{-1}) values of methane and methanol.

Increased N_2O partial pressure also resulted in fast increase in CO and CO_2 formation rates than methanol production rate. This result brings higher TOF CH_4 (h^{-1}) values but lower selectivity values for Micro-Cu-Mordenite.

Table 3.6. Methanol, DME, CO and CO_2 production rates and selectivities at 573 K with the feed composition of 40 mole %, CH_4 5,10 or 15%, N_2O, 3% H_2O and balance He

Zeolite	P_{N2O} / kPa	r_{CH3OH} / µmol g^{-1} h^{-1}	r_{DME} / µmol g^{-1} h^{-1}	r_{CO2} / µmol g^{-1} h^{-1}	r_{CO} / µmol g^{-1} h^{-1}	r_{CH4} / µmol g^{-1} h^{-1}	CH_4 Conversion / %	N_2O conversion / %	TOF CH_4 / h^{-1}	TOF CH_3OH / h^{-1}	S_{CH3OH} / %
Micro-Cu-Mordenite	5.1	36.1±0.3	1.01±0.03	10.1±0.8	8	56	0.015	0.49	0.22	0.14	64
Micro-Cu-Mordenite	10.1	54.7±0.7	2.24±0.03	10.9±0.7	31.9	102	0.027	0.17	0.40	0.22	54
Micro-Cu-Mordenite	15.2	66.5±0.7	2.5±0.1	18.7±1	40	130	0.034	0.14	0.52	0.27	51
Micro-Cu-SSZ-39	5.1	75.8±0.9	3±0.1	63±1.6	70±8	215	0.052	0.39	0.43	0.15	35
Micro-Cu-SSZ-39	10.1	90.6±0.7	5.4±0.1	14.9±0.5	90.2±8	201	0.048	0.22	0.40	0.18	45
Micro-Cu-SSZ-39	15.2	130.0±0.6	8.5±0.1	15±1	86±18	248	0.060	0.42	0.49	0.26	52

Rate order with respect to partial pressure of N_2O

Rates of methane oxidation and methanol production were investigated for different partial pressures of N_2O using expression given in Eq 3.6. Equation 3.6 was linearized and natural logarithm was taken for N_2O partial pressures. Table 3.7 showed the methanol and methane rates and their natural logarithms for rate order investigation.

$$r_{CH4} = -k * P_{CH4}^{\alpha} * P_{N2O}^{\beta} \quad \text{Eq 3.6}$$

Table 3.7. Methanol production rate, methane oxidation rate and natural logarithm of rates of CH_3OH and CH_4 at 573 K

Zeolite	P_{N2O} / kPa	r_{CH3OH} / µmol g^{-1} h^{-1}	r_{CH4} / µmol g^{-1} h^{-1}	ln_{RCH3OH}	ln_{RCH4}	S_{CH3OH} / %
Micro-Cu-Mordenite	5.1	36.1±0.3	56	3.58	4.02	64
Micro-Cu-Mordenite	10.1	54.7±0.7	102	4.00	4.62	54
Micro-Cu-Mordenite	15.2	66.5±0.7	130	4.20	4.87	51
Micro-Cu-SSZ-39	5.1	75.8±0.9	215	4.32	5.37	35
Micro-Cu-SSZ-39	10.1	90.6±0.7	201	4.50	5.30	45
Micro-Cu-SSZ-39	15.2	130.0±0.6	248	4.86	5.51	52

CH_4 oxidation rate and CH_3OH production rate were plotted with respect to lnP_{N2O} in order to understand the rate order on Micro-Cu-SSZ-39 (see Figure 3.27). N_2O rate order of ß = 0.11 was discovered for methane oxidation reaction and R^2 value of 0.40 which is quite out of linear behaviour. N_2O partial pressure significantly affect the methanol production rates from 75 µmol g^{-1} h^{-1} to 130 µmol g^{-1} h^{-1} for Micro-

Cu-SSZ-39, Figure 3.27-a. Methanol production rate order was calculated as 0.46 which could be simply 0.5 order.

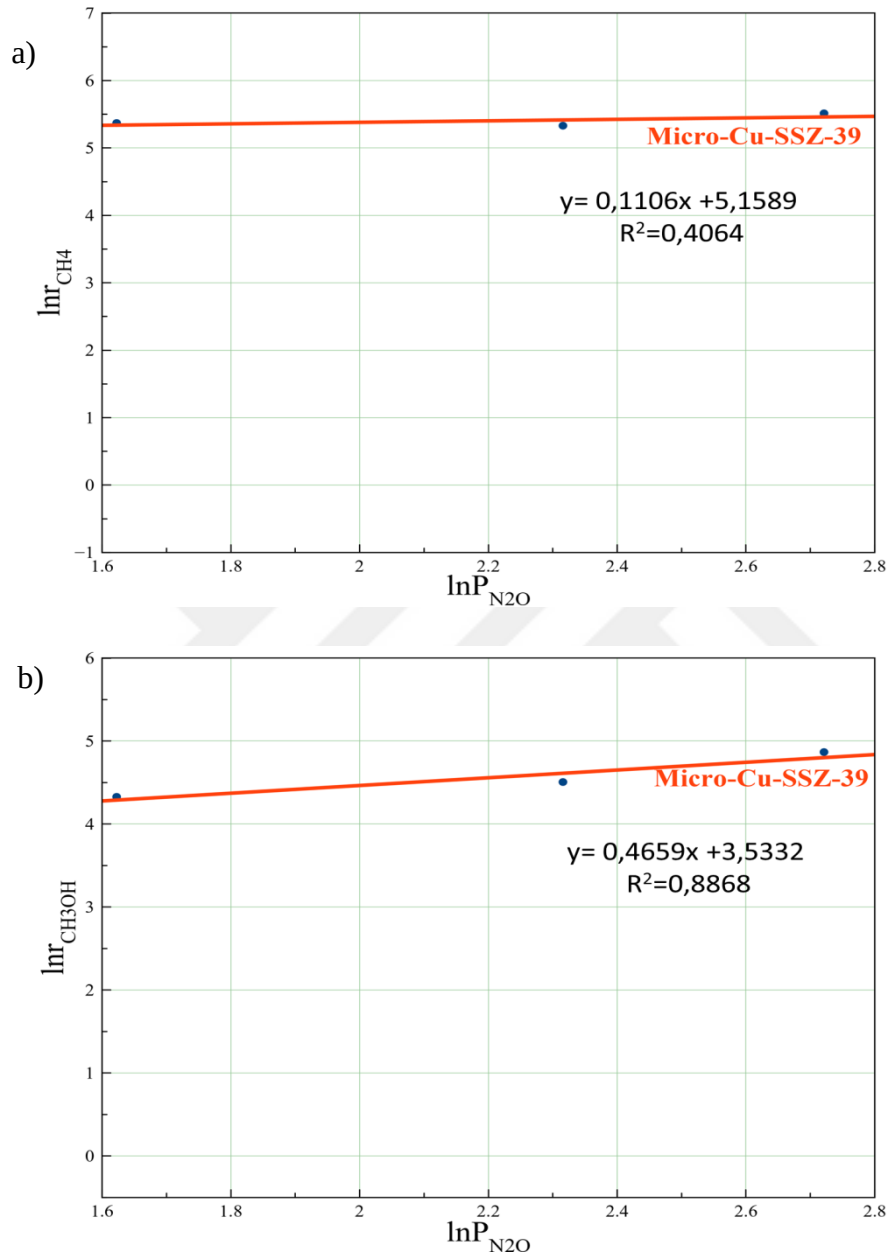

Figure 3.27. Rates with respect to different partial pressure of N_2O on Micro-Cu SSZ-39 a) Rate of CH_4 with respect to lnP_{N2O} b) Rate of CH_3OH with respect to lnP_{N2O}

For Micro-Cu-Mordenite, methane oxidation rate was demonstrated as ß=0.77 and R^2 value of 0.99 in Figure 3.28a. However, increasing N_2O partial pressure caused

increased amount of methanol from 36.1 µmol g^{-1} h^{-1} to 66.5 µmol g^{-1} h^{-1} could be seen from Table 3.7.

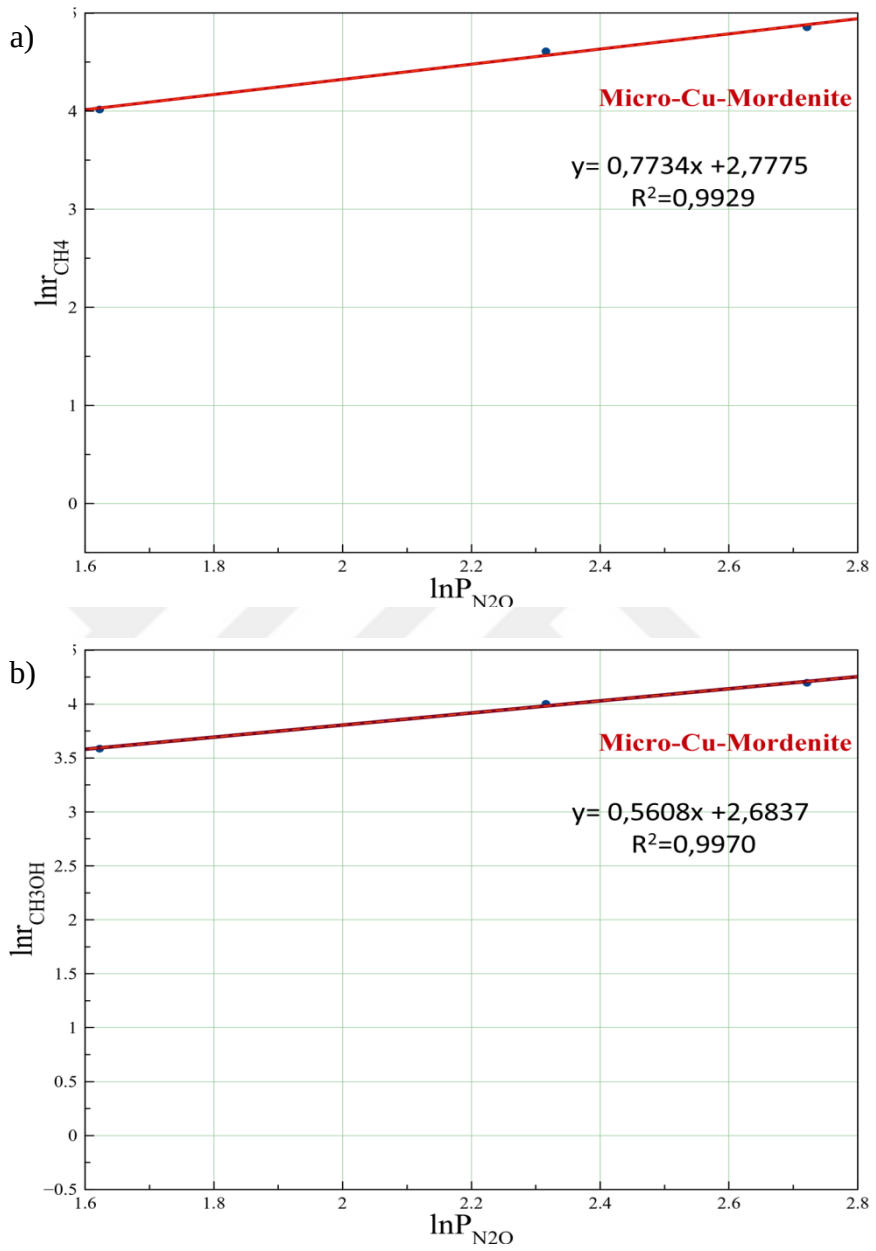

Figure 3.28. Rates with respect to different partial pressure of N_2O on Micro-Cu-Mordenite a) Rate of CH_4 with respect to lnP_{N2O} b) Rate of CH_3OH with respect to lnP_{N2O}

3.2.3 Effect of Methane Partial Pressure

For understanding the effect of partial pressure of CH_4 in reaction, proportional alterations in the partial pressure of methane was made.

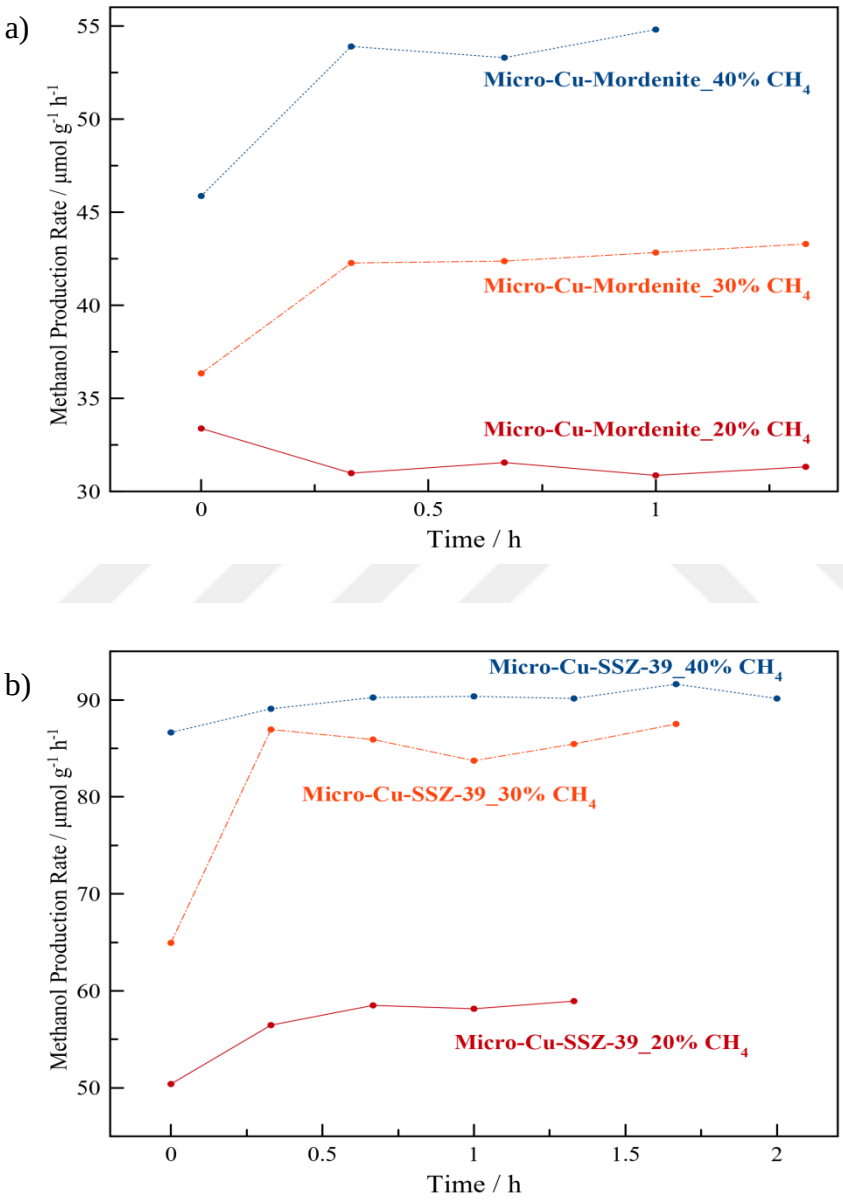

Figure 3.29. Methanol production rates at 573 K (gas composition of 20.2 kPa, 30.4 kPa or 40.5 kPa CH_4, 3.2 kPa H_2O 10.1 kPa N_2O, total flow 100 sccm, ~0.3 g catalyst) a) Micro-Cu Mordenite b) Micro-Cu-SSZ-39

Reactions were performed on Micro-Cu-Mordenite and Micro-Cu-SSZ-39 with feed gas compositions of 20, 30 or 40 mol% CH_4, 10%, N_2O, 3% H_2O and balance He. Methanol production rate values with respect to time can be seen in Figure 3.29.

As seen in Figure 3.29, methanol production rates were observed without any deactivation of both zeolites during the reaction. According to Figure 3.29, increasing CH_4 partial pressure resulted increased amount of methanol production. For production rate, 40% methane partial pressure was superior for both zeolites with production rates of approximately 55 μmol g^{-1} h^{-1} and 90 μmol g^{-1} h^{-1} for Micro-Cu-Mordenite and Micro-Cu-SSZ-39 respectively. The reaction kinetic results were given in Table 3.8.

According to Table 3.8, increasing CH_4 pressure resulted in increased methanol production rates and similar methanol selectivity values for Micro-Cu-Mordenite. But the methanol selectivity slightly decreased with the increasing methanol production rates up to 40.5 kPa of methane pressure on Micro-Cu-SSZ-39. Achieved high methanol production rates, 54.7 μmol g^{-1} h^{-1} and 90.6 μmol g^{-1} h^{-1} motivates selection of 40.5 kPa of methane pressure as the optimum pressure.

Micro-Cu-SSZ-39 was superior catalyst for production of methanol with the composition of 40.5 kPa CH_4, 10.1 kPa N_2O, 3.2 kPa H_2O when compared to Micro-Cu-Mordenite.

Table 3.8. Methanol, DME, CO and CO_2 production rates and selectivities at 573 K with the feed composition of 20, 30 40 mole% CH_4, 10%, N_2O, 3% H_2O and balance He

Zeolite	P_{CH4} / kPa	r_{CH3OH} / µmol g^{-1} h^{-1}	r_{DME} / µmol g^{-1} h^{-1}	r_{CO2} / µmol g^{-1} h^{-1}	r_{CO} / µmol g^{-1} h^{-1}	r_{CH4} / µmol g^{-1} h^{-1}	CH_4 Conversion / %	N_2O conversion / %	TOF CH_4 / h^{-1}	TOF CH_3OH / h^{-1}	S_{CH3OH} / %
Micro-Cu-Mordenite	20.2	31.2±0.3	0.72	14±1	12±6	58.64	0.03	0.14	0.23	0.12	53
Micro-Cu-Mordenite	30.4	42.7±0.5	1.14±0.03	11.4±0.5	6±4	61.88	0.022	0.16	0.25	0.17	69
Micro-Cu-Mordenite	40.5	54.7±0.7	2.24±0.03	10.9±0.7	31.9±0	101.98	0.027	0.18	0.40	0.22	54
Micro-Cu-SSZ-39	20.2	58.5±0.4	2±0.1	10±1	18±5	90.5	0.044	0.17	0.18	0.12	64
Micro-Cu-SSZ-39	30.4	85.7±1.5	3.8±0.3	7.3±1	45±5	145.5	0.047	0.28	0.29	0.17	59
Micro-Cu-SSZ-39	40.5	90.6±0.7	5.4±0.1	14.9±0.5	90±9	206.5	0.050	0.23	0.41	0.18	44

Rate order with respect to partial pressure of CH_4

Effect of altering the methane partial pressure was investigated in this part. Methane oxidation and methanol production rates were found out using Equation 3.4. Table 3.9 shows the methanol and methane rates and their natural logarithms for rate order investigation.

Table 3.9. Methanol production rate, methane oxidation rate and natural logarithm of rates of CH_3OH and CH_4 at 573 K

Zeolite	P_{CH4} / kPa	r_{CH3OH} / µmol g^{-1} h^{-1}	r_{CH4} / µmol g^{-1} h^{-1}	ln_{RCH3OH}	ln_{RCH4}	S_{CH3OH} / %
Micro-Cu-Mordenite	20.2	31.2±0.3	58.64	3.44	4.07	53
Micro-Cu-Mordenite	30.4	42.7±0.5	61.88	3.75	4.13	69
Micro-Cu-Mordenite	40.5	54.7±0.7	101.98	4.00	4.62	54
Micro-Cu-SSZ-39	20.2	58.5±0.4	90.5	4.06	4.50	64
Micro-Cu-SSZ-39	30.4	85.7±1.5	145.5	4.45	4.98	59
Micro-Cu-SSZ-39	40.5	90.6±0.7	206.5	4.50	5.33	44

CH_4 oxidation rate and CH_3OH production rate were plotted with respect to lnP_{CH4} and given in Figure 3.30 (Micro-Cu-SSZ-39) and 3.31 (Micro-Cu-Mordenite).

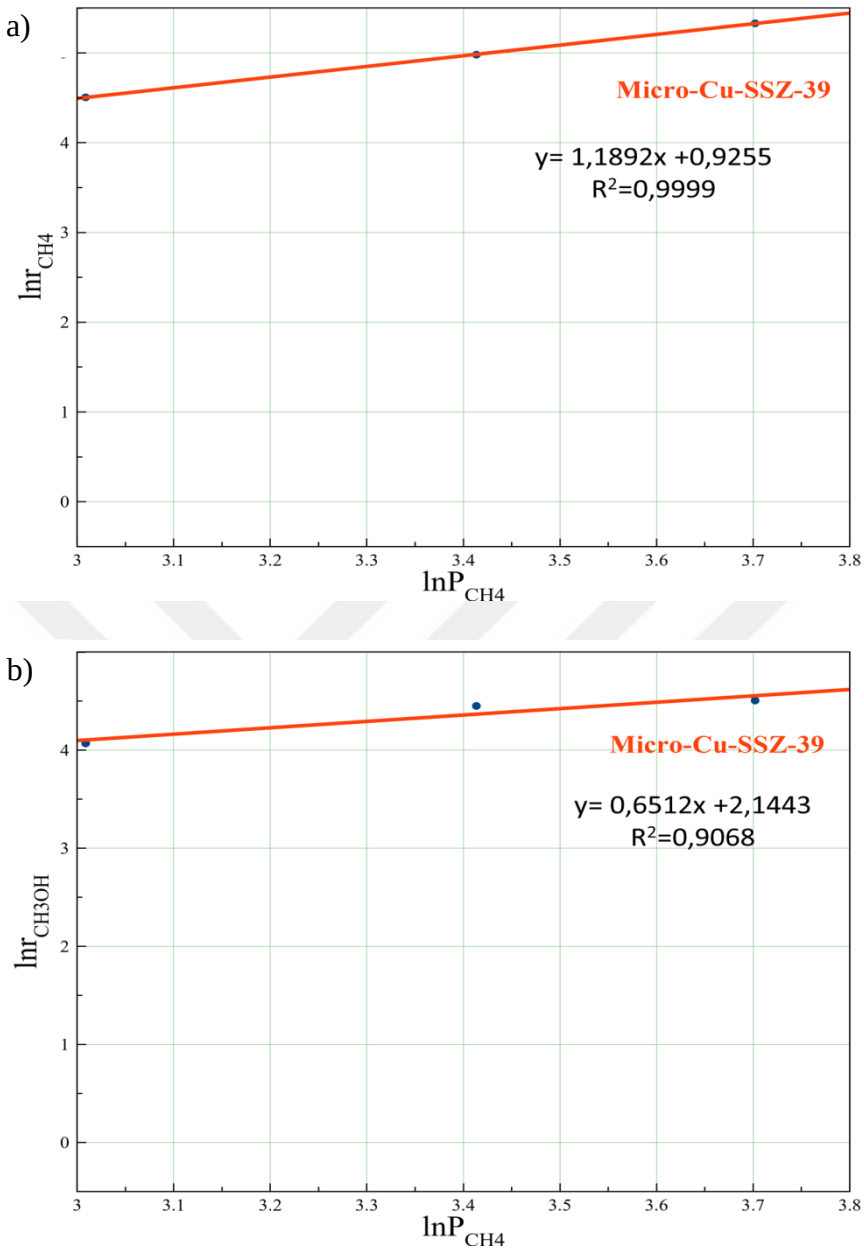

Figure 3.30. Rates with respect to different partial pressure of CH_4 on Micro-Cu-SSZ-39 a) Rate of CH_4 with respect to lnP_{CH4} b) Rate of CH_3OH with respect to lnP_{CH4}

CH_4 rate order of α = 1.19 was discovered for methane oxidation reaction on Micro-Cu-SSZ-39, which means near first order dependence on total rate and methane oxidation rate was increased from 90.5 µmol g^{-1} h^{-1} to 206 µmol g^{-1} h^{-1} in Figure 3.30-a and Table 3.9. For methanol production rate, equation gave the slope of 0.65,

which means sub-first order dependence on methane partial pressure but it significantly affects the methanol production rates from 58.5 μmol g^{-1} h^{-1} to 90.5 μmol g^{-1} h^{-1} for Micro-Cu-SSZ-39, Figure 3.30-b and Table 3.9.

For Micro-Cu-Mordenite, methane oxidation rate was demonstrated as α=0.75 and R^2 value of 0.74 which is quite out of linear behaviour Figure 3.31a. This value is similar to CH_4 order observed for methanol production rate on Cu-ZSM-5 with O_2 as the oxidant [78]. However, increasing CH_4 partial pressure caused increased amount of methane consumption from 59 μmol g^{-1} h^{-1} to 102 μmol g^{-1} h^{-1} could be seen from Table 3.9. From methanol production view, increased partial pressure of CH_4 resulted increased amount of methanol.

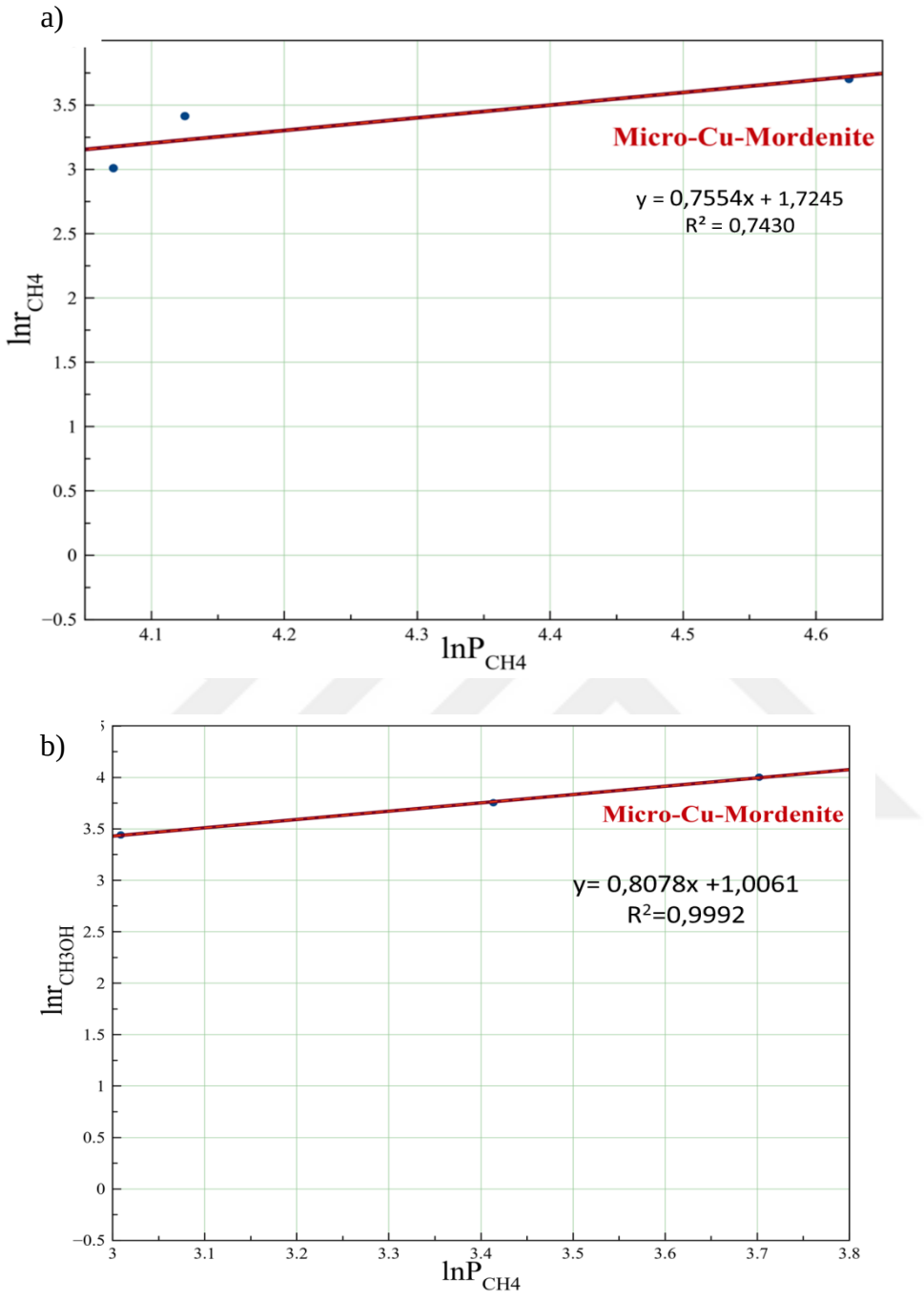

Figure 3.31. Rates with respect to different partial pressure of CH_4 on Micro-Cu-Mordenite a) Rate of CH_4 with respect to lnP_{CH4} b) Rate of CH_3OH with respect to lnP_{CH4}

3.2.4 Effect of Water Partial Pressure

For understanding the water effect on reaction, feed composition of CH_4 40 mole%, 10% N_2O, 3% and 10% H_2O and balance He conditions were tested at 573 K and 598 K on Micro-Cu-Mordenite sample. Micro-Cu-SSZ39 sample was tested in a composition of CH_4 40 mole%, 15% N_2O, 2.8%, 3.8% and 10% H_2O and balance He at 598 K. Total flow rate was fixed 100 sccm. Methanol production rate graphs are given in Figure 3.32 and Figure 3.33.

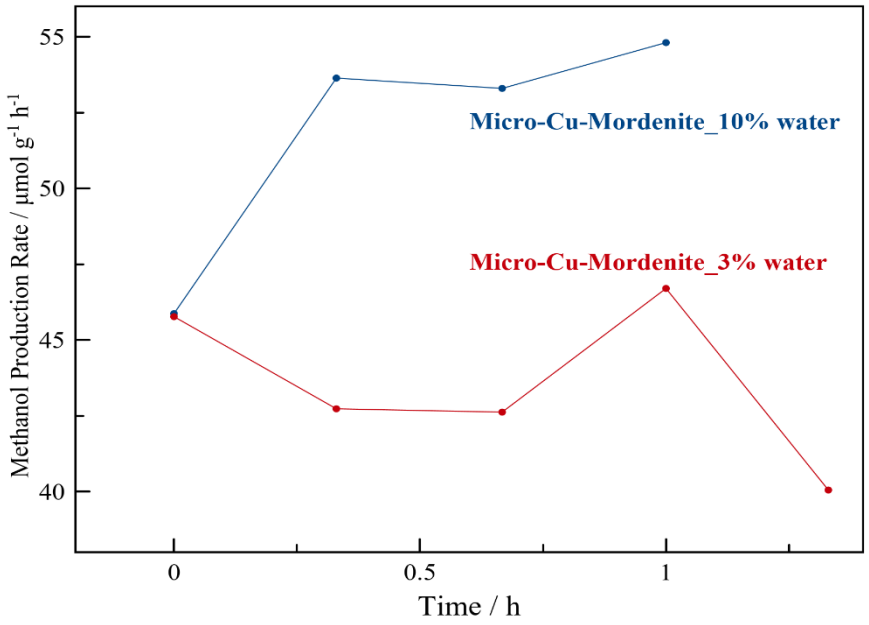

Figure 3.32. Methanol production rates on Micro-Cu-Mordenite at 573 K (gas composition of 40.5 kPa CH_4, 10.13 kPa N_2O, 3.2 kPa H_2O and 10 kPa H_2O, total flow 100 sccm, ~0.3 g catalyst)

Table 3.10 shows the comparison of the Micro-Cu-Mordenite with a feed gas composition consists of 3% H_2O and 10% H_2O. As a result, selectivity values were increased with increasing water partial pressure which takes a role in desorption of surface-bound methoxy species in both total flow rates.

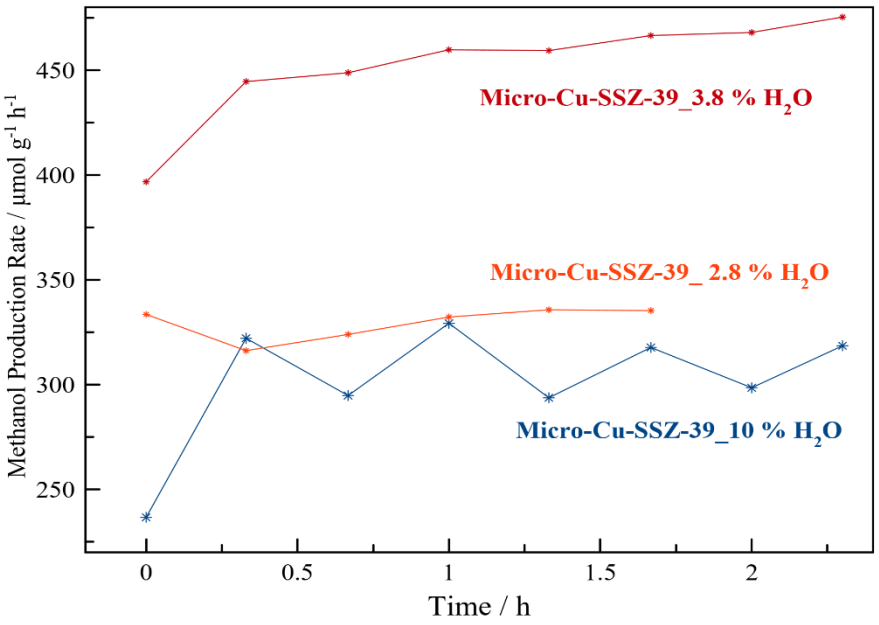

Figure 3.33. Methanol production rates on Micro-Cu-SSZ-39 at 598 K (gas composition of 40.5 kPa CH_4, 15.2 kPa N_2O, 2.8 kPa H_2O, 3.8 kPa H_2O and 10 kPa H_2O, total flow 100 sccm, ~0.3 g catalyst)

From Figure 3.32 and Figure 3.33, sufficient amounts of methanol production rates were observed without any deactivation of both zeolites during the reaction. For Micro-Cu-Mordenite, production rate was decreased from 54.7 µmol g^{-1} h^{-1} to 43.6 µmol g^{-1} h^{-1} yet, selectivity values of 53.6% and 76.3% explains the positive effect of water on methanol selectivity. Prior reports have cogitated that the existence of water decrease desorption energy of the chemisorbed methoxy species in the surface after to form methanol [36,80,81]. Hence, at high partial H_2O pressures, methanol desorption event commence more easily because of decreasing activation energy [82]. Methanol selectivity was significantly increased with increasing water partial pressure which is consistent with the literature [52]. However, at the same time, increased water partial pressure result in a decreased number of active sites, decreasing the total methane conversion as observed for Micro-Cu-mordenite (see Table 3.10).

Methanol production rate firstly showed an increase as the water partial pressure was increased from 2.8 kPa to 3.8 kPa with slightly increased methanol selectivity. This effect was also reported on Cu-SSZ-13 with low values of water vapour pressures (1–2.5 kPa) [83]. However, when the water vapour pressure was increased to 10.1 kPa, both the methanol formation rate and the N_2O conversion decreased, indicating formation of smaller concentration of the active sites.

Small amounts of coke formation were observed on the catalysts. At 598 K, the total amount of coke formation on Micro-Cu-SSZ-39 at 3.8 kPa water vapour pressure was calculated to be 12.2 μmol (9.9 μmol g^{-1} h^{-1} coke formation rate compared to 463 μmol g^{-1} h^{-1} methanol formation rate). The calculated selectivity values and methane conversion values when coke formation was also taken into account is given in Appendix B.10.

Table 3.10. Methanol, DME and CO_2 production rates and selectivities with the feed composition of 40.5 kPa CH_4, 15.2 kPa N_2O, 2.8 kPa, 3.8 kPa and 10 kPa H_2O at 598 K on Micro-Cu-SSZ-39 and feed composition of 40.5 kPa CH_4, 10.1 kPa N_2O, 3.2 kPa and 10 kPa H_2O at 573K and 598 K on Micro-Cu-Mordenite

Zeolite	**Temperature / K**	**P_{H2O} / kPa**	**r_{CH3OH} / µmol g^{-1} h^{-1}**	**r_{DME} / µmol g^{-1} h^{-1}**	**r_{CO2} / µmol g^{-1} h^{-1}**	**r_{CO} / µmol g^{-1} h^{-1}**	**CH_4 Conversion / %**	**N_2O conversion / %**	**TOF CH_4 / h^{-1}**	**TOF CH_3OH / h^{-1}**	**S_{CH3OH} / %**
Micro-Cu-Mordenite	573	3.2	54.7±0.7	2.24±0.03	10.9±0.7	31.9	0.027	0.17	0.40	0.22	53.6
Micro-Cu-Mordenite	573	10.1	44±3	0.49±0.08	10.8±2	1.7	0.015	0.13	0.23	0.17	76.3
Micro-Cu-Mordenite	598	3.2	125±1	9.5±0.1	38±4	201±10	0.102	0.47	1.52	0.50	32.6
Micro-Cu-Mordenite	598	10.1	116±6	2.8±0.6	31±2	121±32	0.073	0.36	1.09	0.46	42.4
Micro-Cu-SSZ-39	598	2.8	330±8	40±2	34±1	445±29	0.215	0.58	1.77	0.65	37.1
Micro-Cu-SSZ-39	598	3.8	463±8	49.6±0.7	44±5	610±17	0.231	0.57	2.42	0.92	38.1
Micro-Cu-SSZ-39	598	10.1	311±15	19±3	89±4	336±23	0.150	0.40	1.54	0.62	40.2

3.2.5 Effect of Total Flow Rate

For studying mass transfer limitation, total flow rates of 50 sccm and 100 sccm were tested. As seen in Table 3.11, total flow rate of 100 sccm gave higher methanol production rates and selectivity values for Meso-Cu-Mordenite, Meso-Cu-SSZ-13 and Meso-Cu-SSZ-39 samples. For microporous samples, higher total flow rate resulted in higher methanol production rates.

Table 3.11. Methanol production and selectivity comparison at 573 K (gas composition of 40.5 kPa CH_4, 10.1 kPa N_2O, 3.2 kPa H_2O, ~ 0.3 g catalyst)

Zeolite	50 sccm		100 sccm	
	R_{CH3OH}	Selectivity	R_{CH3OH}	Selectivity
Micro-Cu-Mordenite	70	59	54.7	54
Meso-Cu-Mordenite	20	18	12.7	34
Micro-Cu-SSZ-39	80.6	55	90.6	43.9
Meso-Cu-SSZ-39	53.4	53.9	65.2	69.7
Micro-Cu-SSZ-13	8	73	24.2	59.4
Meso-Cu-SSZ-13	11	20	22.2	36
Cu-Omega	-	-	9	60

3.2.6 Rate Calculation of Activation Energy

Total rate of C−H activation was analysed as the carbon-weighted sum of all products formed ($r_{total} = r_{CH3OH} + 2r_{DME} + r_{CO2} + r_{CO}$). For procuring the Arrhenius plot, the data in

Table 3.12 was utilized and plots were given in Figure 3.34 and Figure 3.35. C–H bond activation energies are affected by the transition metal cation, the zeolite topology and the active site motif.

Table 3.12. Methanol, DME and CO_2 production rates and selectivities with the feed composition of 40.5 kPa CH_4, 15.2 kPa N_2O, 3.2 kPa H_2O on Micro-Cu-SSZ-39 and feed composition of 40.5 kPa CH_4, 10.1 kPa N_2O, 3.2 kPa H_2O on Micro-Cu-Mordenite at different reaction temperatures (543, 573 and 598 K)

Zeolite	Temperature / K	r_{CH3OH} / µmol g^{-1} h^{-1}	r_{DME} / µmol g^{-1} h^{-1}	r_{CO2} / µmol g^{-1} h^{-1}	r_{CO} / µmol g^{-1} h^{-1}	r_{CH4} / µmol g^{-1} h^{-1}	ln_{RCH3OH}	ln_{RCH4}	S_{CH3OH} / %
Micro-Cu-Mordenite	543	11.7±0.5	0	5±1	1.3±0	18	2.45	2.89	65
Micro-Cu-Mordenite	573	54.7±0.7	2.24±0.03	10.9±0.7	31.9±0	101.98	4.00	4.62	54
Micro-Cu-Mordenite	598	125.2±0.8	9.5±0.1	38±4	201±10	383.3	4.83	5.94	33
Micro-Cu-SSZ-39	543	22.2±0.08	3.2±0.08	5±1	29.9±5	54.6	3.099	4	41
Micro-Cu-SSZ-39	573	129±0.6	8.5 ±0.05	14.7±1.3	86.8±17.8	248.4	4.86	5.51	29
Micro-Cu-SSZ-39	598	325.8±12	37±3	24.8±4	1037±10	1481	5.81	7.30	22

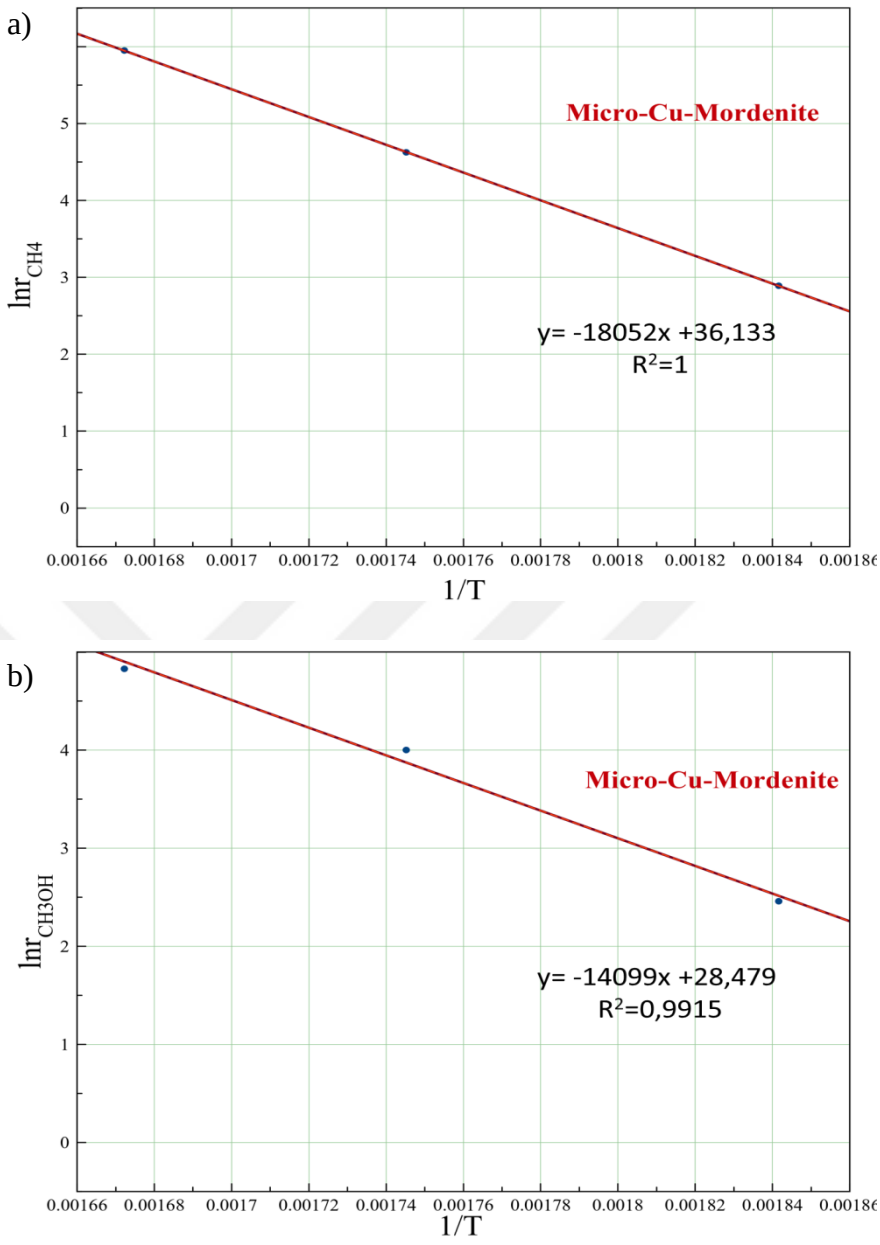

Figure 3.34. Methane oxidation and methanol production on Micro-Cu-Mordenite at 543 K, 573 K and 598 K (gas composition of 40.5 kPa CH_4, 10.1 kPa N_2O, 3.2 kPa H_2O, total flow 100 sccm, ~0.3 g catalyst)

In Figure 3.34, in order to calculate the activation energy of methane oxidation and methanol production natural logarithm of rates with respect to 1/T-temperature data were plotted. For Micro-Cu-Mordenite, activation barrier for methane oxidation was

calculated as 150 kJ mol^{-1}, on the other hand, activation energy for methanol production was determined as 117 kJ mol^{-1}.

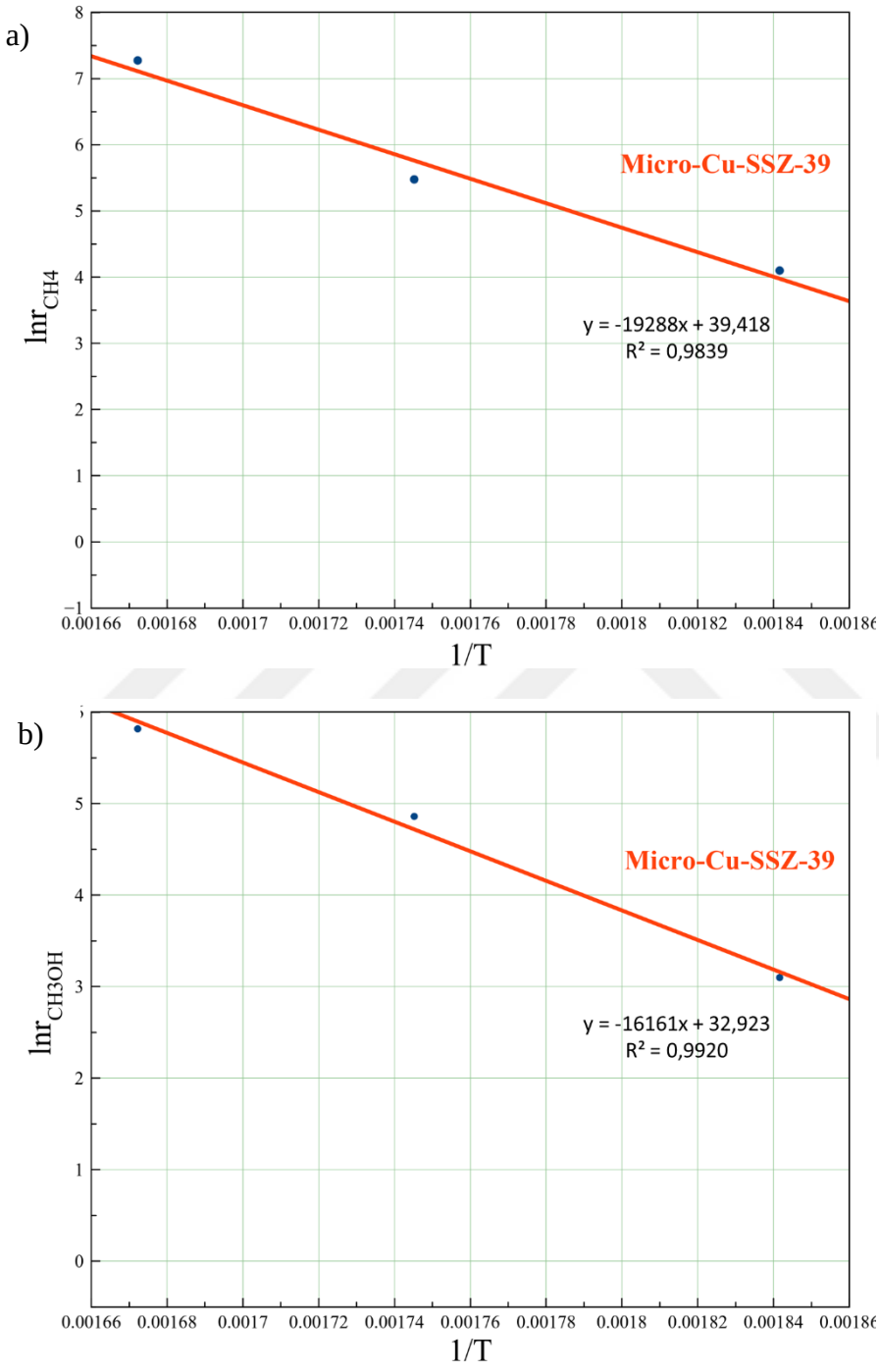

Figure 3.35. Methane oxidation and methanol production on Micro-Cu-SSZ-39 at 543 K, 573 K and 598 K (gas composition of 40.5 kPa CH_4, 15.2 kPa N_2O, 3.2 kPa H_2O, total flow 100 sccm, ~0.3 g catalyst)

In Figure 3.35, natural logarithm of methane and methanol rates with respect to 1/T-temperature data were plotted on Micro-Cu-SSZ-39. Activation energy of C–H bond of methane calculated as 160 kJ mol^{-1}, and methanol production activation energy was calculated using Arrhenius plot as 134 kJ mol^{-1}.

The activation energy for C−H bond dissociation was calculated to be 45.2 kJ mol^{-1} for $[Cu_2(\mu\text{-}O)]^{2+}$ on SSZ-39 by Mahyuddin et al. [13] and 99 kJ mol^{-1} for $[Cu_2(\mu\text{-}O)]^{2+}$ on Mordenite by Zhao et al. [84] by DFT. C–H bond activation in these DFT studies predict an already formed active Cu-oxo species on the zeolite. And then, the active oxygen abstracts a hydrogen from methane (via homolytic cleavage) leading to a methyl radical located and weakly bound to the hydrogen. But in our continuous studies, formation of the active sites together with the C−H bond activation could result in a higher experimental activation energy.

Recently, Dinh et al. calculated the activation energy of Al-free Cu-CHA sample as 140 kJ mol^{-1} for CuO_x nanoparticles. For a presumed $[Cu_2(\mu\text{-}O)]^{2+}$ species, they reported an apparent activation energy of C−H scission was 97 kJ mol^{-1} on Cu-CHA with Cu/Al ratio of 0.22. Our values reaching 160 kJ mol^{-1} indicates presence of a different active species on Cu-SSZ-39.

CHAPTER 4

CONCLUSION

In this study, we have investigated continuous methanol production using Cu(II)-exchanged zeolites. Mesopore addition, effect of temperature, zeolite framework, oxidant partial pressure and methane partial pressure optimization and finally water effect on reaction have been analysed.

Increasing temperature resulted in not only increased amount of methanol formation rate but also decreasing selectivity values because the methane oxidation reaction has a tendency of over-oxidation at higher temperatures. We have seen that at high temperatures, CO and CO_2 production rates are more favoured when compared to methanol.

When we investigated the framework effect on reaction, medium pore zeolite Mordenite and small pore zeolite SSZ-39 have showed the superior amount of methanol production (54.7 μmol g^{-1} h^{-1} and 90.6 μmol g^{-1} h^{-1}, respectively) and selectivity values (54% and 44%); so, further investigations must be done on these zeolites.

Omega, which showed high production of methanol in a 3-step process, did not show significant methanol formation activity in the continuous process. This could be because of the inefficient copper loading, which does not allow to form sufficient number of active sites responsible for methanol formation.

Mesopore addition favoured the methanol selectivity only for SSZ-39, for which the crystal sizes are smaller than the microporous sample. The main effect is considered to be the shortened diffusion pathways that favours the methanol selectivity by decreasing the encounter of methanol with the other active sites.

We understand that lower Cu loading favours the high selectivity on Cu-SSZ-13. Having different Cu/Al ratios has changed the selectivity values, Cu/Al ratio of 0.1 gave the selectivity value of 59%, whereas the Cu/Al ratio of 0.32 gave the 22% selectivity value. This result showed that Cu/Al ratio <0.3 showed better selectivity towards methanol.

N_2O and CH_4 partial pressures have affected the methanol formation rates and selectivity values differently on Micro-Cu-Mordenite and Micro-SSZ-39. On Micro-mordenite, increasing N_2O partial pressure have caused excessive amount of oxidation products, which resulted in decreased methanol selectivity values (64% to 52%). On the other hand, CH_4 partial pressure has not altered the methanol selectivity significantly but again methanol production (from 36.1 μmol g^{-1} h^{-1} to 66.5 μmol g^{-1} h^{-1}) and secondary product formation rates have risen.

On Micro-Cu-SSZ-39 sample, increasing N_2O partial pressure increased the methanol formation rate more dominantly (reaching 130 μmol g^{-1} h^{-1}) than the over-oxidation products, resulting in an increased methanol selectivity (from 35% to 52%). Increase in CH_4 partial pressure resulted in enhanced CO and CO_2 formation rates, decreasing the methanol selectivity from % 64 to %44 even though rate order on methanol production was 0.65. These results implicated that, SSZ-39 have different active sites, which favor methanol formation at higher N_2O partial pressures.

Increasing the water partial pressure was observed to enhance the methanol selectivity for Micro-Cu-Mordenite and Micro-Cu-SSZ-39 while causing a slight decrease in the methanol formation rate due to the decreased number of active sites in presence of water vapour.

The best methanol production rate with 311 μmol g^{-1} h^{-1} and selectivity of 40 % was obtained using Micro-Cu-SSZ-39 catalyst with a feed gas composition of 40.5 kPa CH_4, 15.2 kPa N_2O, 10.1 kPa H_2O at 598 K. For optimizing selectivity and methanol production rate, further investigations should be performed.

CHAPTER 5

RECOMMENDATIONS

The present study demonstrated that catalytic methanol production for Cu-Mordenite, Cu-SSZ-13, Cu-SSZ-39 and Cu-Omega could be achieved with reasonable methanol formation rates and selectivity values. The investigation of different reaction conditions such as temperature, changing the partial pressures of reactants or using different kind of oxidant is necessary to suppress the secondary reactions and for feasibility in commercial scale. Methanol production stability should be investigated with different resulting Cu capacities for promising zeolites, which are SSZ-39 and mordenite. Also, characterization of active sites in these zeolites should be performed in detail to understand the active site and the conditions that favour the active site formation.

REFERENCES

[1] W. Hölderich, M. Hesse, F. Näumann, Angew. Chemie Int. Ed. English 27 (1988) 226–246.

[2] E.M. Flanigen, R.W. Broach, S.T. Wilson, Zeolites in Industrial Separation and Catalysis, 2010.

[3] International Zeolite Association. Database of Zeolite Structures http://www.iza-structure.org/databases/, (n.d.).

[4] H. E Mgbemere, I. C. Ekpa, G. I. Lawal, Int. Res. J. Environ. Sci. 6 (2017) 45–59.

[5] J. Yu, Introduction to Zeolite Science and Practice, 2007.

[6] K. Byrappa, Y. Masahiro, Handbook of Hydrothermal Technology, 2001.

[7] Shuai Ban, Computer Simulation of Zeolites: Adsorption, Diffusion and Dealumination, Utrecht, 2009.

[8] J. Pérez-pariente, T. Álvaro-muñoz, Mesoporous Zeolites: Preparation, Characterization and Applications, 2015.

[9] A. Idris, U. Khalil, I. AbdulAziz, I.G.B.N. Makertihartha, Subagjo, M. Laniwati, A.R. Al-Betar, R.R. Mukti, O. Muraza, Powder Technol. 342 (2019) 992–997.

[10] J. Yue, X. Wang, T. Zeng, L. Chen, Z. Luo, D. Huang, 148 (2018) 3492–3501.

[11] S. Samanta, N.K. Mal, P. Kumar, A. Bhaumik, J. Mol. Catal. A Chem. 215 (2004) 169–175.

[12] K. Nakamoto, M. Ohshiro, T. Kobayashi, J. Environ. Chem. Eng. 5 (2017) 513–525.

[13] M.H. Mahyuddin, Y. Shiota, K. Yoshizawa, Catal. Sci. Technol. 9 (2019) 1744–1768.

[14] M. Dusselier, J.E. Schmidt, R. Moulton, B. Haymore, M. Hellums, M.E. Davis, (2015).

[15] B.N. Bhadra, P.W. Seo, J.W. Jun, J.H. Jeong, T.W. Kim, C.U. Kim, S.H. Jhung, Microporous Mesoporous Mater. 235 (2016) 135–142.

[16] G.S.L. S.I.Zones, Y.Nakagawa, S.T. Evans, , U.S. Pat. 5,958,370 (1997).

[17] M. Dusselier, M.A. Deimund, J.E. Schmidt, M.E. Davis, ACS Catal. 5 (2015) 6078–6085.

[18] Y. Kunitake, M. Yoshioka, J.N. Kondo, T. Yokoi, Appl. Catal. A Gen. 568 (2018) 123–129.

[19] M. Moliner, C. Franch, E. Palomares, M. Grill, A. Corma, Chem. Commun. 48 (2012) 8264–8266.

[20] B. Ipek, M.J. Wulfers, H. Kim, F. Go, I. Hermans, J.P. Smith, K.S. Booksh, C.M. Brown, R.F. Lobo, (2017).

[21] R. Wendelbo, D. Akporiaye, A. Andersen, I.M. Dahl, H.B. Mostad, Appl. Catal. A Gen. 142 (1996) 197–207.

[22] A.M. Goossens, E.J.P. Feijen, G. Verhoeven, B.H. Wouters, P.J. Grobet, P.A. Jacobs, J.A. Martens, 36 (2000) 555–572.

[23] A.J. Knorpp, A.B. Pinar, M.A. Newton, V.L. Sushkevich, J.A. van Bokhoven, ChemCatChem 10 (2018) 5593–5596.

[24] J.F. Allain, P. Magnoux, P. Schulz, M. Guisnet, Appl. Catal. A Gen. 152 (1997) 221–235.

[25] T. Yamazaki, H. Nishimura, S. Ozawa, Microporous Mesoporous Mater. 38 (2000) 187–196.

[26] (n.d.).

[27] (n.d.).

[28] P.J. Smeets, M.H. Groothaert, R.A. Schoonheydt, 110 (2005) 303–309.

[29] N. V. Beznis, B.M. Weckhuysen, J.H. Bitter, Catal. Letters 138 (2010) 14–22.

[30] E.M.C. Alayon, M. Nachtegaal, M. Ranocchiari, J.A. Van Bokhoven, 66 (2012) 668–674.

[31] M.H. Groothaert, P.J. Smeets, B.F. Sels, P.A. Jacobs, R.A. Schoonheydt, J. Am. Chem. Soc. 127 (2005) 1394–1395.

[32] M.J. Wulfers, S. Teketel, B. Ipek, R.F. Lobo, Chem. Commun. 51 (2015) 4447–4450.

[33] M.H. Mahyuddin, A. Staykov, Y. Shiota, M. Miyanishi, K. Yoshizawa, ACS Catal. 7 (2017) 3741–3751.

[34] P. Tomkins, A. Mansouri, S.E. Bozbag, F. Krumeich, M.B. Park, E.M.C. Alayon, M. Ranocchiari, J.A. Vanbokhoven, Angew. Chemie - Int. Ed. 55 (2016) 5467–5471.

[35] D.K. Pappas, A. Martini, M. Dyballa, K. Kvande, S. Teketel, K.A. Lomachenko, R. Baran, P. Glatzel, B. Arstad, G. Berlier, C. Lamberti, S. Bordiga, U. Olsbye, S. Svelle, P. Beato, E. Borfecchia, J. Am. Chem. Soc. 140 (2018) 15270–15278.

[36] D.K. Pappas, E. Borfecchia, M. Dyballa, I.A. Pankin, K.A. Lomachenko, A. Martini, M. Signorile, S. Teketel, B. Arstad, G. Berlier, C. Lamberti, S. Bordiga, U. Olsbye, K.P. Lillerud, S. Svelle, P. Beato, J. Am. Chem. Soc. 139 (2017) 14961–14975.

[37] M.B. Park, H. Ahn, A. Mansouri, M. Ranocchiari, (2017) 3705–3713.

[38] V.L. Sushkevich, D. Palagin, M. Ranocchiari, J.A. Van Bokhoven, 527 (2017) 523–527.

[39] J.S. Woertink, P.J. Smeets, M.H. Groothaert, M.A. Vance, B.F. Sels, R.A. Schoonheydt, E.I. Solomon, (2009) 2–7.

[40] E.M. Alayon, M. Nachtegaal, J.A. Van Bokhoven, (2012) 404–406.

[41] T. Sheppard, C.D. Hamill, A. Goguet, D.W. Rooney, J.M. Thompson, Chem. Commun. 50 (2014) 11053–11055.

[42] S. Grundner, M.A.C. Markovits, G. Li, M. Tromp, E.A. Pidko, E.J.M. Hensen, A. Jentys, M. Sanchez-Sanchez, J.A. Lercher, Nat. Commun. 6 (2015) 1–9.

[43] S.E. Bozbag, E.M.C. Alayon, J. Pecháček, M. Nachtegaal, M. Ranocchiari, J.A. Van Bokhoven, Catal. Sci. Technol. 6 (2016) 5011–5022.

[44] M.A.C. Markovits, A. Jentys, M. Tromp, M. Sanchez-Sanchez, J.A. Lercher, Top. Catal. 59 (2016) 1554–1563.

[45] H. V. Le, S. Parishan, A. Sagaltchik, C. Göbel, C. Schlesiger, W. Malzer, A. Trunschke, R. Schomäcker, A. Thomas, ACS Catal. 7 (2017) 1403–1412.

[46] Y. Kim, T.Y. Kim, H. Lee, J. Yi, Chem. Commun. 53 (2017) 4116–4119.

[47] R. Oord, J.E. Schmidt, B.M. Weckhuysen, Catal. Sci. Technol. 8 (2018) 1028–1038.

[48] M.A. Newton, A.J. Knorpp, A.B. Pinar, V.L. Sushkevich, D. Palagin, J.A. Van Bokhoven, J. Am. Chem. Soc. 140 (2018) 10090–10093.

[49] B. Ipek, R.F. Lobo, Chem. Commun. 52 (2016) 13401–13404.

[50] J. Xu, R.D. Armstrong, G. Shaw, N.F. Dummer, S.J. Freakley, S.H. Taylor, G.J. Hutchings, Catal. Today 270 (2016) 93–100.

[51] K. Narsimhan, K. Iyoki, K. Dinh, (2016) 2–7.

[52] K.T. Dinh, M.M. Sullivan, K. Narsimhan, P. Serna, R.J. Meyer, M. Dincă, Y. Román-Leshkov, J. Am. Chem. Soc. 141 (2019) 11641–11650.

[53] A.R. Kulkarni, Z. Zhao, S. Siahrostami, J.K. Nørskov, F. Studt, (2016).

[54] D. Palagin, A.J. Knorpp, A.B. Pinar, M. Ranocchiari, J.A. Van Bokhoven, Nanoscale 9 (2017) 1144–1153.

[55] G. Brezicki, J.D. Kammert, T.B. Gunnoe, C. Paolucci, R.J. Davis, ACS Catal. 9 (2019) 5308–5319.

[56] M.-L. Tsai, R.G. Hadt, P. Vanelderen, B.F. Sels, R.A. Schoonheydt, E.I. Solomon, J. Am. Chem. Soc. 136 (2014) 3522–3529.

[57] S. Grundner, W. Luo, M. Sanchez-Sanchez, J.A. Lercher, Chem. Commun. 52 (2016) 2553–2556.

[58] G. Li, P. Vassilev, M. Sanchez-Sanchez, J.A. Lercher, E.J.M. Hensen, E.A. Pidko, J. Catal. 338 (2016) 305–312.

[59] P. Tomkins, M. Ranocchiari, J.A. Van Bokhoven, Acc. Chem. Res. 50 (2017) 418–425.

[60] T.D. Pham, Q. Liu, R.F. Lobo, (2013).

[61] E.J.. Feijen, J.A. Martens, A.M. Goossens, P.A. Jacobs, B.H. Wouters, P.J. Grobet, G. Verhoeven, Microporous Mesoporous Mater. 35–36 (2002) 555–572.

[62] 2016 K. Leng, Y. Sun, X. Zhang, M. Yu, and W. Xu, “Ti-modified hierarchical mordenite as highly active catalyst for oxidative desulfurization

of dibenzothiophene," Fuel, vol. 174, pp. 9–16, (n.d.).

[63] A. Galarneau, J. Rodriguez, B. Coasne, (2014).

[64] (n.d.).

[65] P. Iam-khong, P. Muchan, N. Sriprang, M. Nithitanakul, Solid State Sci. 96 (2019) 105956.

[66] Y. Guo, T. Sun, X. Liu, Q. Ke, X. Wei, Y. Gu, S. Wang, 358 (2019) 331–339.

[67] V.L. Sushkevich, D. Palagin, J.A. van Bokhoven, Angew. Chemie - Int. Ed. 57 (2018) 8906–8910.

[68] K. Honda, A. Yashiki, M. Sadakane, T. Sano, Microporous Mesoporous Mater. 196 (2014) 254–260.

[69] H. Chen, Y. Wang, F. Meng, H. Li, S. Wang, C. Sun, S. Wang, X. Wang, RSC Adv. 6 (2016) 76642–76651.

[70] Stud. Surf. Sci. Catal. (2002) 1587–1594.

[71] L. Sommer, D. Mores, S. Svelle, M. Stöcker, B.M. Weckhuysen, U. Olsbye, Microporous Mesoporous Mater. 132 (2010) 384–394.

[72] N. Martín, P.N.R. Vennestrøm, J.R. Thøgersen, M. Moliner, A. Corma, ChemCatChem 9 (2017) 1754–1757.

[73] S. Yang, N.P. Evmiridis, Stud. Surf. Sci. Catal. 84 (1994) 155–162.

[74] J.B. Condon, Surf. Area Porosity Determ. by Physisorption (2006) 1–27.

[75] C.L. Knight, M. a. Williamson, R.J. Bodnar, Microbeam Anal. (1989) 572–574.

[76] Y. Yu, G. Xiong, C. Li, F.S. Xiao, Microporous Mesoporous Mater. 46 (2001) 23–34.

[77] P. Vanelderen, B.E.R. Snyder, M.L. Tsai, R.G. Hadt, J. Vancauwenbergh, O. Coussens, R.A. Schoonheydt, B.F. Sels, E.I. Solomon, J. Am. Chem. Soc. 137 (2015) 6383–6392.

[78] K. Narsimhan, K. Iyoki, K. Dinh, Y. Román-Leshkov, ACS Cent. Sci. 2 (2016) 424–429.

[79] A.J. Knorpp, M.A. Newton, V.L. Sushkevich, P.P. Zimmermann, A.B.

Pinar, J.A. Van Bokhoven, Catal. Sci. Technol. 9 (2019) 2806–2811.

[80] Z.J. Zhao, A. Kulkarni, L. Vilella, J.K. Nørskov, F. Studt, ACS Catal. 6 (2016) 3760–3766.

[81] E.M.C. Alayon, M. Nachtegaal, A. Bodi, J.A. Van Bokhoven, ACS Catal. 4 (2014) 16–22.

[82] M.H. Mahyuddin, T. Tanaka, Y. Shiota, A. Staykov, K. Yoshizawa, ACS Catal. 8 (2018) 1500–1509.

[83] A. Koishybay, D.F. Shantz, J. Am. Chem. Soc. 142 (2020) 11962–11966.

[84] D. Zhao, Y. Zhang, Z. Li, Y. Wang, J. Yu, Chem. Eng. J. 323 (2017) 295–303.

APPENDICES

A. N_2 Adsorption/Desorption Data obtained at 77 K

Table A. 1. N_2 adsorption data for Micro-Cu-Mordenite

Relative Pressure / P/P_0	**Quantity Adsorbed / cm^3 g STP $^{-1}$**	**Relative Pressure / P/P_0**	**Quantity Adsorbed / cm^3 g STP $^{-1}$**
1.032E-4	8.88607601	0.98714284	176.813809
1.1617E-4	18.7895933	0.98949741	180.551213
1.2112E-4	28.7042673	0.98949741	180.551213
1.2668E-4	38.6149433	0.9862937	175.211022
1.4526E-4	48.5106909	0.9805398	170.688122
1.4663E-4	58.3947455	0.97315968	165.158558
1.5593E-4	68.3037318	0.97171635	164.295726
1.6256E-4	78.156488	0.96559134	160.462907
1.8108E-4	88.0478581	0.95382881	155.885402
2.285E-4	97.8545035	0.94291973	152.635484
4.1621E-4	106.866476	0.92588233	149.688837
5.0464E-4	108.623063	0.90770063	147.625338
9.9874E-4	114.194817	0.87775307	145.482814
0.00247902	119.920607	0.84264403	144.039541
0.00506361	123.479477	0.803189	142.986398
0.00757307	125.200501	0.7437383	142.036756
0.01052451	126.525696	0.63981524	141.035999
0.01461902	127.770651	0.53992358	140.023339
0.01971487	128.86177	0.44992194	138.064813
0.02977176	130.285697	0.35265857	137.303781
0.04954133	131.994928	0.29062946	136.957349
0.06940085	133.091397	0.24116353	136.623896
0.10201106	134.298858	0.2006974	136.225066
0.15052003	135.461306	0.16057636	135.676588
0.20063306	136.232774	0.14017919	135.325842
0.25060594	136.807927	0.12022862	134.913202
0.2971569	137.194489	0.10025262	134.384094
0.39751193	137.799592		
0.49674873	138.431777		
0.59982935	139.259683		
0.69973661	140.191309		
0.79921837	141.890748		
0.84763424	143.200131		
0.90481235	146.073313		
0.92401491	147.767658		
0.93864794	149.766194		
0.95201971	152.299386		
0.96225495	155.385057		
0.96995613	158.901301		
0.97585151	163.036921		
0.98124519	167.841332		
0.98391805	170.93837		
0.98579262	173.520538		

Table A. 2. N_2 adsorption data for Meso-Cu-Mordenite

Relative Pressure / P/P_0	**Quantity Adsorbed / $cm^3\ g^{-1}$**	**Relative Pressure / P/P_0**	**Quantity Adsorbed / $cm^3\ g^{-1}$**
3.4313E-5	9.36066879	0.98846386	263.067535
5.822E-5	19.1749471	0.98358297	257.804151
5.1771E-5	29.0658373	0.97920622	251.233671
5.5292E-5	38.9063927	0.97430355	244.675833
5.6725E-5	48.7690036	0.97148241	241.167201
5.7344E-5	58.6397251	0.96663078	235.980997
7.2095E-5	68.4939133	0.95595285	227.584281
6.892E-5	78.3648165	0.94088918	220.16056
9.9648E-5	88.1468164	0.92823914	215.658339
1.7657E-4	97.8696285	0.90729922	210.262317
2.6014E-4	101.656092	0.86851865	202.175547
5.0931E-4	108.674618	0.83239201	195.284173
0.00101148	114.911604	0.80083674	190.904081
0.0024971	123.297695	0.7434493	185.96616
0.00496124	129.155734	0.65266816	180.944119
0.00731017	132.37732	0.55199299	176.94813
0.00983767	134.757985	0.44465203	169.897707
0.01552624	138.319246	0.34874693	164.950432
0.02090252	140.602874	0.3018154	163.194072
0.02921293	143.182982	0.24245962	160.843274
0.04934307	147.208375	0.20100504	159.039465
0.06881502	149.829202	0.16087737	157.005411
0.10164043	153.005548	0.14018723	155.813107
0.15061849	156.429166	0.12029612	154.523765
0.20155637	159.195222	0.10034536	153.036629
0.25180098	161.514669		
0.30197351	163.586301		
0.39681323	167.431216		
0.4961972	171.370641		
0.59889731	175.839007		
0.6991434	181.011562		
0.79790563	188.519294		
0.84619022	194.532341		
0.90229554	205.874704		
0.92533232	211.722113		
0.93890942	215.704649		
0.95114629	220.110473		
0.96194561	225.530893		
0.96956286	230.970638		
0.97562397	237.032071		
0.98042639	244.324761		
0.9836163	249.952192		
0.98541833	254.354062		
0.98799986	261.117578		
0.98846386	263.067535		

Table A. 3. N_2 adsorption data for Micro-Cu-SSZ-13

Relative Pressure / P/P_0	**Quantity Adsorbed / cm^3 g^{-1}**	**Relative Pressure / P/P_0**	**Quantity Adsorbed / cm^3 g^{-1}**
8.836E-5	9.09033601	0.98928969	221.947228
1.1103E-4	18.9499157	0.98074262	219.168007
1.1863E-4	28.8309028	0.96897485	217.154234
1.2924E-4	38.7127832	0.95520928	215.903455
1.2165E-4	48.6149236	0.94329324	215.37639
1.3374E-4	58.4829516	0.93024329	214.95057
1.3488E-4	68.3784942	0.91477001	214.672599
1.3216E-4	78.2697284	0.89541366	214.432264
1.3715E-4	88.1447399	0.865566	214.453421
1.5544E-4	98.0317908	0.83060903	214.681954
1.3873E-4	107.889869	0.79061899	214.899064
1.57E-4	117.760265	0.73140469	215.396514
1.6055E-4	127.647836	0.64211456	216.260592
1.6577E-4	137.542946	0.54166547	217.252254
1.8565E-4	147.413492	0.4422069	217.389432
1.9913E-4	157.248851	0.34546018	217.016528
2.1957E-4	160.857683	0.30083038	216.660743
3.205E-4	170.209377	0.24151785	215.773207
6.9728E-4	179.694711	0.20074798	214.811115
0.00102938	182.639021	0.16057938	213.505778
0.00245677	188.352973	0.14016728	212.617655
0.00492124	192.40206	0.12017025	211.620828
0.00775587	194.938458	0.10035345	210.414886
0.01036582	196.539544		
0.01580813	198.897869		
0.01956406	200.090746		
0.02956219	202.491523		
0.04980689	205.70518		
0.06913414	207.828729		
0.10207945	210.431157		
0.15100123	213.071425		
0.19994536	214.80777		
0.25132384	216.010618		
0.30142784	216.765484		
0.39789424	217.25659		
0.50810336	216.93125		
0.60776312	216.433346		
0.70725195	215.816813		
0.80657617	215.286436		
0.85853912	215.084452		
0.91270581	215.307507		
0.9237609	215.366394		
0.9385647	215.676871		
0.95213821	216.172932		
0.96310003	216.840357		
0.97053721	217.520963		
0.97637446	218.352499		
0.98157594	219.264226		
0.98384458	219.766534		
0.98564992	220.311584		
0.98738296	221.170865		
0.98928969	221.947228		

Table A. 4. N_2 adsorption data for Meso-Cu-SSZ-13

Relative Pressure / P/P_0	**Quantity Adsorbed / cm^3 g^{-1}**	**Relative Pressure / P/P_0**	**Quantity Adsorbed / cm^3 g^{-1}**
1.2874E-4	4.75373567	0.98862501	254.508568
1.3867E-4	14.6555326	0.98371299	249.343643
1.571E-4	24.538529	0.97857448	243.375579
1.8916E-4	34.3581988	0.97334681	237.798802
2.0308E-4	44.1961467	0.97148585	236.098216
2.1476E-4	54.0905314	0.96425135	230.457142
2.2171E-4	63.987383	0.95453375	224.384718
2.4146E-4	73.8646155	0.9411585	218.384773
2.2853E-4	83.7255808	0.92723928	213.922894
2.5946E-4	93.6107925	0.90740468	209.585507
2.6511E-4	103.503591	0.87868088	205.428592
2.6934E-4	113.323962	0.84397801	202.203389
2.639E-4	123.202348	0.80347124	199.675151
2.7269E-4	133.063109	0.74400793	197.123759
3.1713E-4	142.862742	0.63903084	194.021673
5.2633E-4	152.48117	0.55374202	192.543121
0.00104153	156.55757	0.44314254	187.653062
0.00254703	159.91893	0.35165381	180.036485
0.00500697	162.10267	0.30092333	178.059991
0.0077276	163.436381	0.23757215	176.348558
0.01039787	164.355938	0.20152449	175.398792
0.01476015	165.42825	0.16060749	174.304084
0.01983744	166.347762	0.14033226	173.711718
0.02981073	167.641205	0.12027827	173.053522
0.04972476	169.351655	0.10022162	172.332558
0.06941774	170.545428		
0.10158001	171.998317		
0.15050009	173.663697		
0.20092842	175.070757		
0.24800885	176.348533		
0.29807449	177.750927		
0.39595699	181.017884		
0.49634781	185.160418		
0.59759051	188.941609		
0.69608982	191.927789		
0.79880316	195.236214		
0.84630867	197.601189		
0.90580831	202.834932		
0.92464265	205.745377		
0.93886733	208.993342		
0.95130356	213.098113		
0.96212872	218.428419		
0.96976345	223.977946		
0.97596415	230.11918		
0.98080264	237.020439		
0.98392205	242.390865		
0.98549631	245.912962		
0.9879566	251.518271		
0.98862501	254.508568		

Table A. 5. N_2 adsorption data for Micro-Cu-SSZ-39

Relative Pressure / P/P_0	**Quantity Adsorbed / $cm^3\ g^{-1}$**	**Relative Pressure / P/P_0**	**Quantity Adsorbed / $cm^3\ g^{-1}$**
1.1706E-4	4.83544212	0.98873898	152.902813
1.3411E-4	14.7160302	0.98016988	151.256754
1.4448E-4	24.6250602	0.96852169	149.868909
1.577E-4	34.5291954	0.95449417	149.036584
1.6003E-4	44.4454054	0.94280996	148.638441
1.8214E-4	54.336173	0.92985266	148.379274
1.8499E-4	64.2282377	0.91524281	148.224136
1.9544E-4	74.1260003	0.89522352	148.147198
2.0297E-4	75.4964716	0.86559134	148.191095
2.2365E-4	85.3793288	0.83071877	148.390442
2.2054E-4	95.2998726	0.79074788	148.706268
2.3765E-4	105.194862	0.7309652	149.383679
2.4444E-4	115.078961	0.64152415	150.4829
2.5026E-4	124.958486	0.54132473	151.805769
3.0397E-4	134.751899	0.44060587	153.00499
5.0361E-4	142.770298	0.34222104	154.257414
0.00100668	147.409599	0.28911324	154.903579
0.00259658	151.28458	0.22907251	155.57875
0.0052129	153.17098	0.18889727	155.961572
0.00806361	154.093458	0.1488261	156.284963
0.01030957	154.542523	0.12888234	156.40877
0.0147111	155.092019	0.10928546	156.496031
0.01986062	155.483832	0.09110808	156.550186
0.02974787	155.929038		
0.04987852	156.32792		
0.0763361	156.495498		
0.10100305	156.493498		
0.15042221	156.313845		
0.21103547	155.882985		
0.26107227	155.438354		
0.31102783	154.949285		
0.41017397	153.818172		
0.50981411	152.595787		
0.60896761	151.353832		
0.70827157	150.165376		
0.80728005	149.163476		
0.85844472	148.738745		
0.9130472	148.693183		
0.93432974	148.871827		
0.94009512	148.952229		
0.95243931	149.277724		
0.96296751	149.754074		
0.97072787	150.218032		
0.97667236	150.786837		
0.98168009	151.43598		
0.98355732	151.824958		
0.98583452	152.248506		
0.98743133	152.627825		
0.98873898	152.902813		

Table A. 6. N_2 adsorption data for Meso-Cu-SSZ-39

Relative Pressure / P/P_0	**Quantity Adsorbed / $cm^3 g^{-1}$**	**Relative Pressure / P/P_0**	**Quantity Adsorbed / $cm^3 g^{-1}$**
1.4221E-4	2.3940524	0.98892212	93.4582267
4.3795E-4	6.15131679	0.9787804	91.495455
5.1878E-4	6.44699574	0.96735663	89.9160736
0.00111173	7.92953012	0.9539529	88.5651886
0.00270967	9.61568243	0.94228369	87.6641846
0.00500913	10.8218989	0.92918651	86.7895262
0.0079231	11.7455712	0.92523217	86.5237466
0.01061131	12.3659225	0.90611599	85.413585
0.014865	13.0756721	0.87698276	83.9739653
0.01978466	13.7186625	0.8423229	82.2408141
0.02997651	14.693871	0.80259886	80.0010428
0.04988398	16.0210714	0.74190364	74.0353765
0.06961559	17.0275125	0.69512626	61.7369977
0.09952129	18.2341601	0.65761969	51.2656527
0.15011752	19.8706551	0.64935849	49.5025727
0.19999796	21.2535815	0.58920639	40.0912793
0.24979089	22.5499119	0.553	36.5311543
0.29975569	23.8686968	0.44188516	28.9930389
0.39637214	26.8784066	0.35299193	25.7835359
0.49662522	30.7019419	0.29081902	24.126321
0.60089578	35.9587186	0.24142968	22.9828557
0.69962346	43.2885667	0.2008511	22.0262965
0.79053601	55.0329395	0.16056453	21.0416246
0.80363738	57.3538565	0.14026603	20.4805024
0.84605248	66.5790832	0.12013317	19.92038
0.89806106	78.2652511	0.10030668	19.2860518
0.90527453	79.422364		
0.92278502	81.6944135		
0.93836189	83.6679349		
0.95163062	85.5910845		
0.96307417	87.4889349		
0.9703096	88.9432302		
0.97659027	90.2911357		
0.98156196	91.4597424		
0.98383323	92.0448908		
0.98591166	92.5430079		
0.98797093	93.1586607		
0.98892212	93.4582267		

Table A. 7. N_2 adsorption data for Cu-Omega

Relative Pressure / P/P_0	**Quantity Adsorbed / $cm^3 g^{-1}$**	**Relative Pressure / P/P_0**	**Quantity Adsorbed / $cm^3 g^{-1}$**
1.178E-4	4.75161609	0.98914048	150.242716
2.1742E-4	14.6581874	0.9805604	147.102021
2.9661E-4	23.790051	0.97006755	144.074729
4.0108E-4	34.0694803	0.95633066	141.461889
5.3561E-4	41.2559476	0.94393938	139.788325
0.00122729	49.3519591	0.93058593	138.45069
0.00272007	56.6589408	0.92576639	138.008529
0.00530867	60.7153609	0.90600196	136.661787
0.01082359	64.6019425	0.87688293	135.22381
0.01806992	66.9662166	0.84219422	134.117347
0.02261736	68.2496757	0.80289936	133.107587
0.03031442	69.6176945	0.74201225	128.852846
0.04888436	71.7308856	0.69635037	118.048152
0.06933268	73.208432	0.65486166	107.344145
0.10137067	74.7498414	0.64966225	106.251453
0.1506436	76.4239404	0.58849311	96.6875062
0.20099697	77.7586595	0.5512253	93.3025823
0.25082785	78.8974543	0.44217921	87.0082896
0.30007191	80.0067501	0.35307131	84.9537809
0.39670767	82.3430021	0.29061416	83.9463322
0.4964884	85.4203218	0.24133374	83.2090516
0.60028114	89.8438005	0.20062379	82.5845826
0.69925267	96.3887686	0.16059223	81.8851975
0.79591533	108.176744	0.14024989	81.4602411
0.84672202	118.60133	0.12025583	80.9738204
0.89795963	130.174623	0.10026377	80.4103248
0.9059531	131.608764		
0.92257998	134.031841		
0.9382003	136.295021		
0.95186448	138.619658		
0.96267901	140.857701		
0.97055232	142.72676		
0.97672942	144.541921		
0.98208141	146.437711		
0.98413233	147.45497		
0.98616418	148.436042		
0.98783719	149.410266		
0.98914048	150.242716		

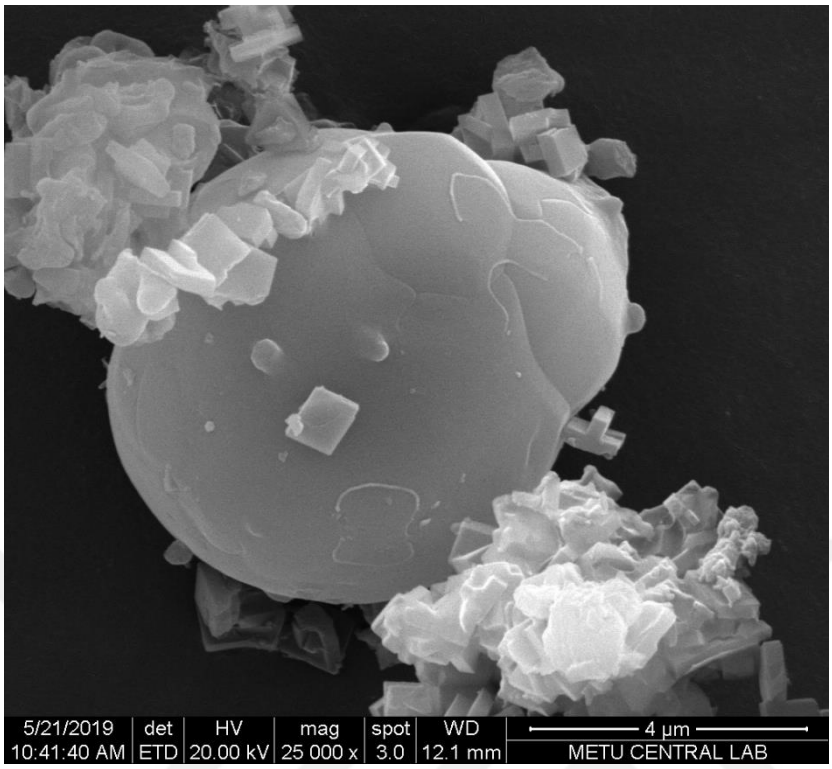

Figure A.1. SEM image of Mesoporous-Cu-SSZ-39

Analcime (ANA) phase formed during the synthesis of mesoporous SSZ-39. Zeolite morphology in 6–7 µm spherical particles were also observed.

B. Sample Calculation of Micro-Cu-SSZ-39 Reaction Results

B.1. CH_3OH Production Rate

Reaction conditions: 0.243 ± 0.005 g zeolite; feed mixture: 40 mole% CH_4 + 15% N_2O + 3% H_2O with balance He; total flow rate 100 sccm; reaction temperature 598 K

FID Peak Area = 291.1

Response factor (RF) of CH_3OH = 1.0313 ppm area^{-1}

Methanol Concentration / ppm = FID Peak Area × RF

$$Molar\ Flow\ Rate\ of\ CH_3OH\ \left(\frac{\mu mol}{min}\right)$$

$$= 291.1 * 1.0313 * 100\ sccm * 10^{-6}\frac{m^3}{min}$$

$$* \frac{101325\ Pa}{\frac{8.314J}{mol.K} * (T_{room} + 273)K} = 1.36\ \frac{\mu mol}{min}$$

$$Methanol\ Production\ Rate\ \left(\frac{\mu mol\ CH_3OH}{gcat * h}\right)$$

$$= \frac{1.36\ \mu mol}{min} * \frac{60\ min}{h} * \frac{1}{0.243 gcat} = 335\ \frac{\mu mol\ CH_3OH}{gcat * h}$$

B.2. DME Production Rate

Reaction conditions: 0.243 ± 0.005 g zeolite; feed mixture: 40 mole% CH_4, 15% N_2O, 3% H_2O with balance He; total flow rate 100 sccm; reaction temperature 598 K

FID Peak Area = 61.5

Response factor (RF) of DME = 0.59 ppm area^{-1}

DME Concentration (ppm) = FID Peak Area × RF

$$Molar\ Flow\ Rate\ of\ DME\ \left(\frac{\mu mol}{min}\right)$$

$$= 61.5 * 0.59 * 100\ scmm * 10^{-6}\frac{m^3}{min} * \frac{101325\ Pa}{\frac{8.314J}{mol.K} * (T_{room} + 273)K}$$

$$= \ 0.16\ \frac{\mu mol}{min}$$

$$DME\ Production\ Rate\ \left(\frac{\mu mol\ DME}{gcat * h}\right) = \frac{0.16\ \mu mol}{min} * \frac{60\ min}{h} * \frac{1}{0.243 gcat}$$

$$= 40.57\ \frac{\mu mol\ DME}{gcat * h}$$

B.3. CO Production Rate

Reaction conditions: 0.243 ± 0.005 g zeolite; feed mixture: 40 mole% CH_4, 15% N_2O, 3% H_2O with balance He; total flow rate 100 sccm; reaction temperature 598 K

FID Peak Area = 11.76

Response factor (RF) of CO = 74.4 ppm area^{-1}

CO Concentration (ppm) = FID Peak Area × RF

$$Molar\ Flow\ Rate\ of\ CO\ \left(\frac{\mu mol}{min}\right)$$

$$= (FID\ Peak\ area) * RF * 100\ sccm * 10^{-6}\frac{m^3}{min}$$

$$* \frac{101325\ Pa}{\frac{8.314J}{mol.K} * (T_{room} + 273)K} = \ 4.19\frac{\mu mol}{min}$$

$$CO\ Production\ Rate\ \left(\frac{\mu mol\ CO}{gcat * h}\right) = \frac{4.19\ \mu mol}{min} * \frac{60\ min}{h} * \frac{1}{0.243 gcat}$$

$$= 1037\ \frac{\mu mol\ CO}{gcat * h}$$

B.4. CO_2 Production Rate

Reaction conditions: 0.243 ± 0.005 g zeolite; feed mixture: 40 mole% CH_4, 15% N_2O + 3% H_2O with balance He; total flow rate 100 sccm; reaction temperature 598 K

FID Peak Area = 0.27

Response factor (RF) of CO_2 = 77.5 ppm area^{-1}

CO_2 Concentration (ppm) = FID Peak Area × RF

$$Molar\ Flow\ Rate\ of\ CO_2\ \left(\frac{\mu mol}{min}\right)$$

$$= 0.27 * 77.5 * 100 * 10^{-6}\frac{m^3}{min} * \frac{101325\ Pa}{\frac{8.314J}{mol.K} * (T_{room} + 273)K}$$

$$= 0.09\frac{\mu mol}{min}$$

$$CO_2\ Production\ Rate\ \left(\frac{\mu mol\ CO2}{gcat * h}\right) = \frac{0.09\ \mu mol}{min} * \frac{60\ min}{h} * \frac{1}{0.243 gcat}$$

$$= 24.80\ \frac{\mu mol\ CO_2}{gcat * h}$$

B.5. CH_4 Conversion

$$r_{CH4}\left(\frac{mol\ CH_4}{gcat * h}\right) = (r_{CH3OH} + 2 * r_{DME} + r_{CO} + r_{CO2}) * 10^{-6}$$

$$= 0.000883\ \frac{mol\ CH_4}{gcat * h}$$

$$Molar\ Flow\ Rate\ of\ CH_4\ \left(\frac{mol\ CH_4}{gcat * h}\right)$$

$$= 40 * 10^{-12}\frac{m^3}{min} * \frac{101325\ Pa}{\frac{8.314J}{mol.K} * (273)K} * \frac{60\ min}{h} * \frac{1}{0.243\ gcat}$$

$$= 0.440\frac{mol\ CH_4}{gcat * h}$$

$$CH_4\ conversion = \frac{r_{CH_4}\left(\frac{mol\ CH_4}{gcat * h}\right)}{Molar\ Flow\ Rate\ of\ CH_4\left(\frac{mol\ CH_4}{gcat * h}\right)} * 100 = 0.20\ \%$$

B.6. N_2O Conversion

Reaction conditions: 0.243 ± 0.005 g zeolite;feed mixture: 40 mole% CH_4, 15% N_2O, 3% H_2O with balance He; total flow rate 100 sccm; reaction temperature 598 K

FID Peak Area = 110.3

Response factor (RF) of CH_3OH = 7.58 ppm area^{-1}

Methanol Concentration / ppm = FID Peak Area × RF

$$r_{N2}\left(\frac{mol\ N_2}{gcat * h}\right)$$

$$= 110.3 * 7.58 * 100\ sccm * 10^{-12}\frac{m^3}{min} * \frac{101325\ Pa}{\frac{8.314J}{mol.K} * (273)K}$$

$$* \frac{60\ min}{h} * \frac{1}{0.243\ gcat} = 0.000934.96\ \frac{mol\ N_2O}{gcat * h}$$

$$Molar\ Flow\ Rate\ of\ N_2O\ \left(\frac{mol\ N_2O}{gcat * h}\right)$$

$$= 15 * 10^{-6}\frac{m^3}{min} * \frac{101325\ Pa}{\frac{8.314J}{mol.K} * (273)K}\frac{60\ min}{h} * \frac{1}{0.243\ gcat}$$

$$= 0.165\frac{mol\ N_2O}{gcat * h}$$

$$N_2O\ conversion = \frac{r_{N_2}\ \left(\frac{mol\ N_2O}{gcat * h}\right)}{Molar\ Flow\ rate\ of\ N_2O\ \left(\frac{mol\ N_2O}{gcat * h}\right)} * 100 = 0.56\ \%$$

B.7. TOF CH_4

Reaction conditions: 0.243 ± 0.005 g zeolite; feed mixture: 40 mole% CH_4 + 15% N_2O + 3% H_2O with balance He; total flow rate 100 sccm; reaction temperature 598 K.

$$TOF\ CH_4 = \frac{r_{CH4}\left(\frac{mol\ CH_4}{gcat * h}\right)}{\frac{mol\ Cu}{gcat}} = \frac{0.000883}{0.502 * 10^{-3}} = 1.76\ h^{-1}$$

B.8. TOF CH_3OH

Reaction conditions: 0.243 ± 0.005 g zeolite; feed mixture: 40 mole% CH_4 + 15% N_2O + 3% H_2O with balance He; total flow rate 100 sccm; reaction temperature 598 K.

$$TOF\ CH_3OH = \frac{r_{CH3OH}\left(\frac{mol\ CH_3OH}{gcat * h}\right)}{\frac{mol\ Cu}{gcat}} = \frac{0.000329}{0.502 * 10^{-3}} = 0.66\ h^{-1}$$

B.9. Reaction Rate Data

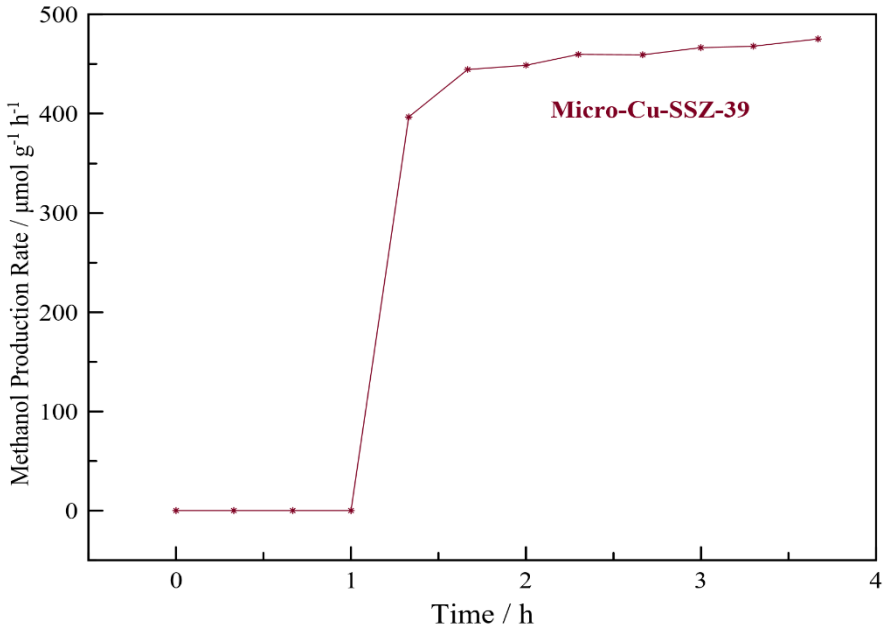

Figure B.1. Methanol production rates at 598 K (gas composition of 40.5 kPa CH_4, 15.2 kPa N_2O, 3.8 kPa H_2O, total flow 100 sccm, ~0.205 g catalyst)

B.10. Carbon Balance

Table B.1. Methanol, coke formation rate and carbon balance based on product formation rate and CH_4 areas on Micro-Cu-SSZ-39

P_{H2O}/ kPa	r_{CH3OH} / (μmol g^{-1} h^{-1})	r_{CH4} / (μmol g^{-1} h^{-1})	Conversion from rCH_4 (Eq. 3.3, %)	Conversion from products including coke, %	Conversion from CH_4 area, %	Coke formation (μmol g^{-1} h^{-1})
3.8	463±8	1216.4	0.231	0.233	0.261	9.9
10.1	311±15	773.3	0.150	0.151	0.110	2.8